Top Quark Pair Production at the LHC

Von der Fakultät für
Mathematik, Informatik und Naturwissenschaften
der RWTH Aachen University
zur Erlangung des akademischen Grades
eines Doktors der Naturwissenschaften
genehmigte Dissertation

vorgelegt von

Diplom–Physiker

Peter Bärnreuther

aus Aachen

Berichter: Universitätsprofessor Dr. Michael Czakon
Universitätsprofessor Dr. Michael Krämer

Tag der mündlichen Prüfung: 28.06.2012

Abstract

One of the most interesting and manifold processes in the Standard Model of elementary particle physics is the top quark pair production. It enabled the discovery of the top quark at the Tevatron in 1995 and the determination of many of its properties. By means of a precise measurement and calculation of the cross section of top quark pair production it is possible to extract the top quark mass. Improvements in the gluon parton distribution functions (important for the Higgs boson production) or improvements in the prediction of the Higgs mass are also closely linked with the top quark pair production. Furthermore, the production process plays an important role in the discovery of new physics. On the one hand the top quark pair decays form the largest part of the background in many BSM[1] models, on the other hand BSM physics can be detected directly in the decay process by investigating the charge symmetry or the invariant mass spectrum.

At the LHC it will be possible for the first time to produce a large amount of top quarks; thereby the statistical errors of the observables will be strongly reduced. The enormous increase in the production rate has two reasons. On the one hand, the acceleration energy of the LHC (14 TeV and 7 TeV) is significantly greater than that of the Tevatron (1.96 Tev). This leads to an increase of the cross section by a factor of 100 ($\sim$7.3 pb at the Tevatron to $\sim$800 pb at 14 TeV LHC). On the other hand, the luminosity of the LHC outperforms the Tevatron by a factor of 10-100. The reduced experimental errors for the observables demand an improvement of the theoretical error.

The experimental accuracy of the LHC and the great relevance of the process led to an intensive activity of different research groups in order to improve the calculation of the cross section of top quark pair production. This work presents for the first time a complete numerical result for the full NNLO correction for the top quark pair production in quark anti-quark annihilation channel, and the result of the double virtual corrections in the gluon fusion channel. The latter was calculated by the author in his doctoral thesis autonomously. Our results agree with already published partial results. Furthermore, the author was involved in the improvement of the double virtual corrections in the quark annihilation channel through implementation of newly developed methods. The complete NNLO results enable a reduction of the scale dependence of the production process from 15% to 4%. This allows an excellent comparison with the experimental results. Another essential component of this work, was the development and implementation of new methods for the computer-aided calculation of the production process. Two papers will be published, containing material from this thesis.

[1] Beyond standard model

Zusammenfassung

Einer der vielfältigsten und interessantesten Prozesse im Standardmodell der Elementarteilchenphysik ist die Top Quark Paar Produktion. Sie ermöglichte 1995 die Entdeckung des Top Quarks am Tevatron und die Bestimmung vieler seiner Eigenschaften. Durch die präzise Messung und Berechnung des Wirkungsquerschnitts der Top Quark Paar Produktion ist es möglich auf die Top Quark Masse zurück zuschließen. Auch die Verbesserung der Gluon PDFs (Partonverteilungsfunktionen) für die Higgs Boson Produktion oder die Verbesserung der Vorhersage der Higgsmasse sind eng mit der Top Quark Paar Produktion verknüpft. Des Weiteren spielt der Produktionsprozess eine wichtige Rolle bei der Entdeckung neuer Physik. So kann sie zum Einen direkt im Zerfallsprozess nachgewiesen werden z.B. mit Hilfe der Ladungssymmetrie oder im invarianten Massenspektrum des Top Quarks, zum Anderen bilden Top Quark Paar Zerfälle in vielen BSM[2] Modellen den größten Anteil am Hintergrund.

Am LHC wird es zum ersten Mal möglich sein eine große Menge von Top Quarks zu produzieren und dadurch den statistischen Fehler der Observablen stark zu reduzieren. Der enorme Anstieg in der Produktionsrate hat zwei Gründe. Zum Einen ist die Beschleunigungsenergie des LHC (14 TeV bzw. 7 TeV) signifikant größer als die des Tevatrons (1.96 TeV). Dies führt zu einer Erhöhung des Wirkungsquerschnitts um den Faktor 100 ($\sim$7.3 pb am Tevatron gegen $\sim$800 pb am 14 TeV LHC). Zum Anderen ist die Luminosität des LHC um den Faktor 10-100 größer verglichen mit der des Tevatrons. Der reduzierte experimentelle Fehler für die Observablen erfordert eine Verbesserung des theoretischen Fehlers.

Die experimentelle Genauigkeit des LHC und die große Relevanz des Prozesses führte zu einer intensiven Auseinandersetzung verschiedener Arbeitsgruppen mit der Berechnung des Wirkungsquerschnitts der Top Quark Paar Produktion. Mit dieser Arbeit liegt zum ersten Mal ein komplettes, numerisches Ergebnis für die gesamte NNLO Korrektur für die Top Quark Paar Produktion im Quark Anti-Quark Vernichtungskanal vor, sowie das Ergebnis der doppelten virtuellen Korrekturen des Gluon Fusions Kanals. Der Autor hat in seiner Doktorarbeit letztere selbstständig berechnet. Unsere Ergebnisse bestÃ¤tigen bereits analytisch vorliegenden Teilergebnisse. Des Weiteren war der Autor durch Implementierung neu entwickelter Methoden maßgeblich an der Verbesserung der doppelt virtuellen Korrekturen im Quark Vernichtungskanal beteiligt. Die kompletten NNLO Ergebnisse ermöglichen es die Skalenabhängigkeit des Produktionsprozesses von 15% auf 4% zu reduzieren, was einen exzellenten Vergleich mit den experimentellen Ergebnissen ermöglicht. Ein weiterer wesentlicher Bestandteil dieser Arbeit war die Entwicklung und Implementierung von neuen Methoden zur computergestützten Berechnung

[2]Beyond standard model

von Produktionsprozessen. Wir werden 2 Publikationen über die Top Quark Paar Produktion veröffentlichen, welche im Rahmen dieser Doktorarbeit entstanden sind.

Contents

1. Introduction to Top Quark Pair Physics

After the discovery of the Bottom quark in 1977, there was no doubt about the existence of its Isospin Doublet partner, the top quark. Nevertheless, it needed 18 years of intensive search at different particle accelerators to finally discover it at the proton anti-proton accelerator Tevatron. Not until then, the collider energy was high enough to produce the ~ 173 GeV heavy top quark.

Today the proton-proton collider LHC provides first high precision measurements of observables related to the top quark. The quality of the recorded data at the LHC ($\geq 5\text{fb}^{-1}$) already outmatches today the whole data set collected at the Tevatron over the last 15 years and thus promises an exciting future. With the LHC's help it will be possible to explore nature up to energies that never have been reached before.

The LHC was built for three main reasons. First, the discovery of the Higgs Boson. Second, the search for physics beyond the standard model and third, the determination of standard model parameters, especially the properties of the top quark.

In the next sections it will be shown, that all three main motivations for building the LHC are strongly connected with top quark pair production and that a calculation of the cross section to NNLO precision is essential.

1.1. Measurement of Top Quark Parameters

The standard model comprises a set of free parameters that are a priori unknown. However, once these 25 parameters [1] and the PDFs are measured, all other observables can be predicted. Therefore, it is crucial to measure the input parameter with the highest possible accuracy.

At the LHC it will be possible for the first time to produce a huge amount of top quarks, and hence to reduce the statistical error in the observables drastically. The enormous increase in the production rate has two reasons. First, the accelerator energy of the LHC (14 TeV or 7 TeV) is significantly higher than the one of its competitor (1.96 TeV). This implies that more parton pairs have enough energy to produce a top quark pair which leads to a cross section which is 100 times larger (~ 7.3 pb at the Tevatron against ~ 800 pb at the LHC). The dependence of the cross section on the accelerator energy is shown in Figure 1.1 . The second reason for the higher production rate is that the LHC luminosity outperforms the one of Tevatron by a factor of $10 - 100$.

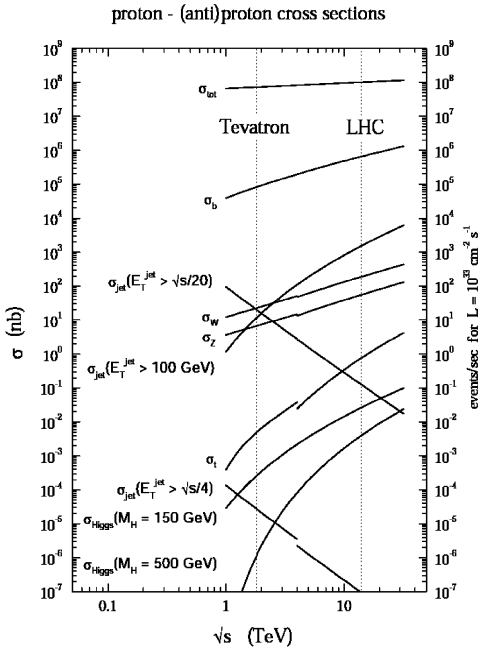

Figure 1.1.: Dependence of different cross sections on the accelerator energy $\sqrt{s}$ (logarithmic scale). Figure taken from [2].

Due to the huge amount of available data at the LHC, the statistical error is neglectable for many measurements involving the top quark, and the overall error is dominated by the systematic error. At 10 fb^{-1}, the total statistical uncertainty for the $t\bar{t}$ production will be only $\sim 0.4\%$. Experimentalists claim, that it will be possible to reduce the error for the cross section below 5%, even 3% seems possible [3].

Top Quark Mass Measurement

The top quarks have an extremely small lifetime of $\sim 10^{-23}$s and decay into W bosons and Bottom quarks [1]. The Bottom quarks are seen as b-jets and the W bosons decay further. Each of them can decay leptonically into a neutrino and a lepton, or hadronically into two quarks (see Figure 1.2). Top quark pair decays are distinguished by the decay channels of the W bosons. The different channels and their branching ratio are presented in Figure 1.3.
The top quark mass can be measured in two different ways. The first one consists of a direct reconstruction of the event kinematics by measuring the decay products. The second method is indirect, uses the cross section and is explained in the next subsection. Although most top quark properties have a large uncertainty, its mass has been determined very accurately to less

[1] Due to the small size of the non-diagonal elements of the CKM matrix it is sufficient to restrict oneself to the case of a decay into Bottom quarks.

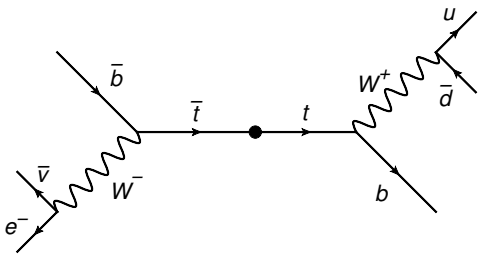

Figure 1.2.: Decay of a top quark Pair. One W-Boson decays hadronically, the other one leptonically.

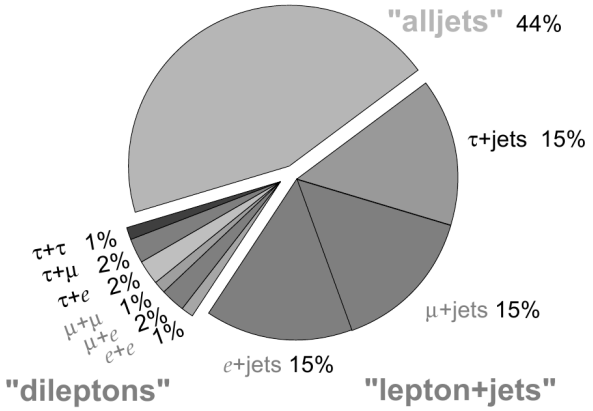

Figure 1.3.: Channels and branching ratios of a top quark pair decay. Plot taken from [4]

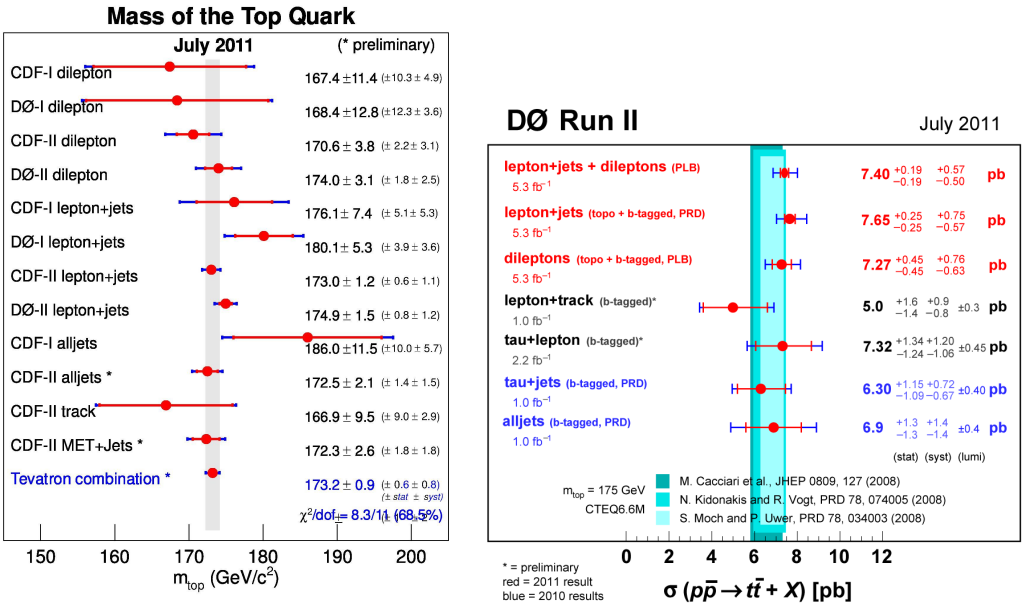

Figure 1.4.: Left: top quark mass measurement from the different decay channels at the Tevatron. Right: Determination of the top quark Pair cross section at the DØ experiment in the different channels. Plot taken from [4]

than 1% relative error (see Figure 1.4). The LHC will improve this measurement further and the ILC could measure the mass with the help of a threshold scan with an error of ~ 200 MeV.

The direct method of the top quark mass measurement identifies possible top quark decays in the data, reconstructs the masses of the W bosons and finally, together with the two b-jets, the top quark mass. This mass determination is performed independently in each channel and the results are combined. The reconstruction is optimized for the different channels by choosing proper cuts. The 4 to 6 observed jets have to be assigned to the decay products of the top quarks in each event. Problems arise from the combinatoric in the reconstruction of the top quarks decay products and from the non-detected Neutrino in case of a leptonic decay. The ambiguity can be reduced with the help of b-tagging. In practice the jets are so assigned that the following function is minimized:

$$\chi^2 = \left(\frac{M_t - M_{\bar{t}}}{\sigma_{M_t}}\right)^2 + \left(\frac{M_{W_1} - M_{W_0}}{\sigma_{M_W}}\right)^2 + \left(\frac{M_{W_2} - M_{W_0}}{\sigma_{M_W}}\right)^2, \tag{1.1}$$

where M_{W_0} is the known W boson mass, M_{W_1}, M_{W_2} and M_t, $M_{\bar{t}}$ are the reconstructed W bosons and top quark masses. Therefore, the chosen combination minimizes the difference between the measured top and anti-top quark mass M_t and $M_{\bar{t}}$ and the difference between the known W boson mass and the reconstructed ones.

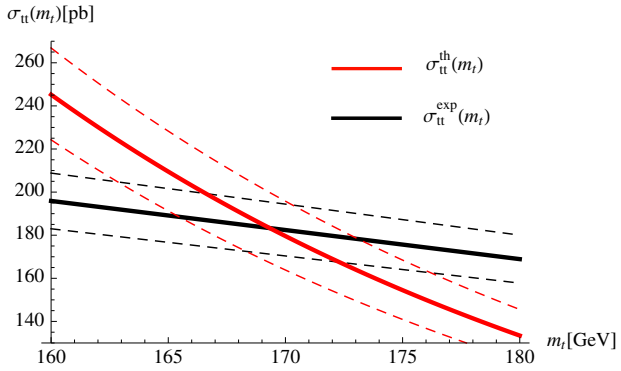

Figure 1.5.: Mass dependence of the theoretical NNLL cross section (gray) and of the experimental cross section (black), as obtained from Monte Carlo studies the by ATLAS collaboration. The solid lines represent the central values, while the total uncertainties of the theoretical and experimental results are given by the external dashed lines. Plot taken from [5].

Top Quark Cross Section

The measurement of the top quark cross section is performed independently in all decay channels and its results are combined (see Figure 1.4). Top quark pair production is identified by two b-tagged jets and, according to the channels,two reconstructed W-Bosons decay. The cross section is given by

$$\sigma = \frac{N_{obs} - N_{back}}{\varepsilon \, L \, b} \, , \tag{1.2}$$

where N_{obs} is the observed number of events, N_{back} the number of expected background events, L is the integrated luminosity and the factor ε describes the detector's efficiency for the process at hand. If there are different decay channels, the branching fraction b has to be included.
This procedure has the advantage, that no mass reconstruction is needed and therefore the systematic error is much smaller. The cross section can be used to determine the top quark mass, as can be seen in Figure 1.5. There, both the theoretical and the experimental expectation for the cross section are plotted in dependence of the top quark mass. The intersection of the two curves gives it value of the top quark mass. It is important to notice, that the error of the mass is only one fifth of the error of the cross section ($\frac{\Delta\sigma}{\sigma} \approx 5\frac{\Delta m_t}{m_t}$). That means, a precise measurement of the top quark pair cross section of 3% to 5% at the LHC leads to the determination of the top quark mass with an error of 0.6% to 1%.

1.2. Physics Beyond the Standard Model and the Top Quark

Discovering BSM Particles in the $t\bar{t}$-channel

In the last section it was discussed, that the top quark mass can be measured in two independent ways. First, directly by kinematic mass reconstruction, second using a cross section

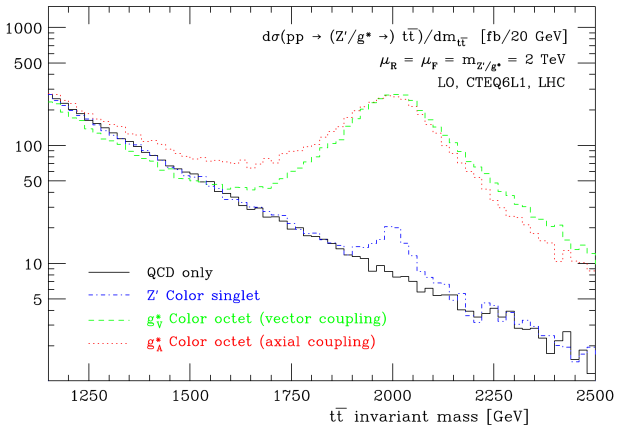

Figure 1.6.: $t\bar{t}$ invariant mass spectrum, including different non-SM extensions. Solid: QCD $t\bar{t}$ production. Dot-dashed: with a color singlet (Z'). Dotted with a color octet axial vector (axigluon g_A). Dashed with a color octet vector boson (KK gluon/coloron g_V). Plot taken from [6].

measurement. If both values differ significantly, this would strongly hint at new physics. Yet undiscovered particles could decay to top quark pairs, leading to an increase of the measured cross section. In Figure 1.6 the $t\bar{t}$ invariant mass spectrum for $p\overline{p} \to t\bar{t}$ is plotted for the SM and for various extensions. One model includes an additional s-channel Z' color singlet vector boson, the others a color octet vector bosons with masses $m_X = 2000$ GeV that couples with standard model strength to quarks. For example a non SM (pseudo-)scalar particle increases $\sigma_{t\bar{t}}$, being produced via a top quark loop (see Figure 1.10) and decaying into a top quark Pair. A measurement of this spectrum can give crucial hints to the existence and properties of the new particles. The contributions of the color octet vector bosons would be so large, that they could even be seen in the total cross section. On the other hand top quarks could decay to unknown particles, resulting in a smaller cross section. In both cases a discrepancy will emerge between the directly and indirectly measured top quark mass.

Charge asymmetry

The strong production of top quark pairs at LO predicts no preferred direction for each of the two quarks, because it is symmetric under charge conjugation. Taking into account, that the initial $p\overline{p}$-state at the Tevatron is not symmetric, this symmetry is a coincidence. The charge asymmetry arises at NLO through interference of terms in the amplitude which are symmetric and terms which are antisymmetric under the exchange of a top and an anti-top quark. There is a negative contribution from gluon radiation $q\overline{q} \to t\bar{t}g$ and a larger positive one from the interference between the virtual box diagrams and the Born. Therefore the top quarks tend to go in the direction of the incoming quark, and the anti-top quarks in the directions of the incoming anti-quark.
Due to its symmetric initial state, the gluon fusion channel has no effect on the asymmetry [7].

Therefore, charge asymmetry plays a larger role at the Tevatron, where 85% of the top quark pairs are produced in the $q\bar{q}$ annihilation channel, whereas at the LHC the gluon fusion channel dominates with 90%. Moreover at the LHC, as a pp collider, the top quarks have on average much more momentum than the anti-top quarks. This makes it more difficult to detect the asymmetry. Nevertheless the LHC will try to measure it.
The charge asymmetry for the Tevatron in the $t\bar{t}$ rest frame is given (including the LO electroweak corrections and resummation of threshold logarithms) by [8, 9]:

$$A_{RF}(t\bar{t}) = 0.073^{+0.009}_{-0.007}\,. \tag{1.3}$$

The error is estimated by renormalization and factorization scale dependence. Both, the CDF and the DØ collaboration find a non-zero top quark charge asymmetry. DØ measured [10]:

$$A_{RF}^{\mathrm{D\O}}(t\bar{t}) = 0.08 \pm 0.04\ (\mathrm{stat.}) \pm 0.01\ (\mathrm{syst.}) \tag{1.4}$$

The CDF collaboration corrected in their analysis their results for hadronization, underlying event, background effects, etc. which leads to an enhancement of the charge asymmetry [10]

$$A_{RF}^{\mathrm{CDF}}(t\bar{t}) = 0.057 \pm 0.028 \tag{1.5}$$

These measurements are almost two standard deviations larger than the theory predictions given in Equation (1.3). There are three possibilities to solve this discrepancy:

- First, the error of the measurements is statistically dominated and hence the two sigma derivation could be a pure statistical effect. In this case it would disappear with increasing statistics.
- Second, the effect can be explained by some BSM models such as [11].
- Third, higher order effects in perturbation theory might increase the predicted cross section. The need to go from NLO to the full NNLO is discussed in [7].

Background to new physics

High energy jets, leptons and missing transverse energy are typical signals for SUSY as well as for $t\bar{t}$ decays. The missing energy in (semi-)leptonic top quark pair decays, originates from the non-detectable Neutrinos. Hence, they often form the dominant part of the background to signals predicted by BSM models and therefore knowing the cross section σ_{tt} with a high precision increases the probability to uncover the BSM physics.
In Figure 1.7 the discovery potential of SUSY at the (already excluded) benchmark parameter point SU4 for the channel with one lepton, 4 jets and missing transverse energy is shown, for the LHC at 10 TeV and an integrated luminosity of 200 pb^{-1}. Usually, searches of BSM physics look for events with a large missing transverse momentum M_T. The semi-leptonic top quark pair decays give by far the largest SM contribution to the background and therefore the top quark pair cross section must be known to a high accuracy to discriminate between signal and background and permit the discovery of Supersymmetry.

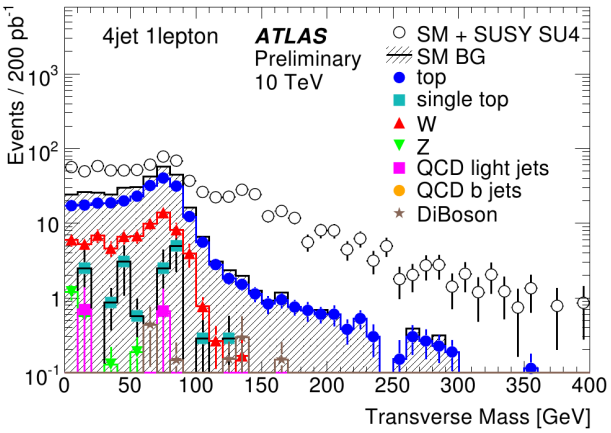

Figure 1.7.: M_T distributions for the 4 jet channel with 1 lepton. Plot taken from [12].

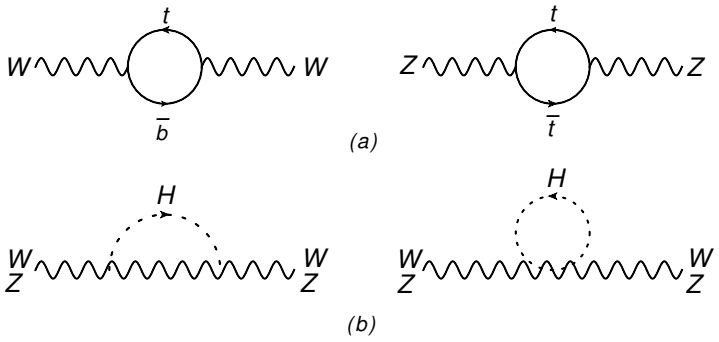

Figure 1.8.: (a) Radiative corrections to the W and Z propagators from the top quark. (b) Radiative contributions to the W and Z propagators coming from the Higgs Boson.

1.3. Higgs Hunting with Top Quarks

In the search for the Higgs Boson the top quark shows up on two fronts.

A Consistency Check for the SM Higgs Boson Mass

First, the Higgs Boson mass can be determined from the masses of the top quark and the mass of the W boson. The relation of these 3 parameters arises from higher order radiative corrections, as can be seen in Figure 1.8.
The W-Boson mass can be expressed as:

$$m_W^2 = \frac{\pi\alpha}{\sqrt{2}G_F} \cdot \frac{1}{\sin^2\theta_W(1-\Delta r)}, \tag{1.6}$$

where $\sin\theta_W$ is the weak mixing angle and Δr can be calculated within the electroweak theory. The contributions from first-order perturbation theory can be seen in Figure 1.8 and give as

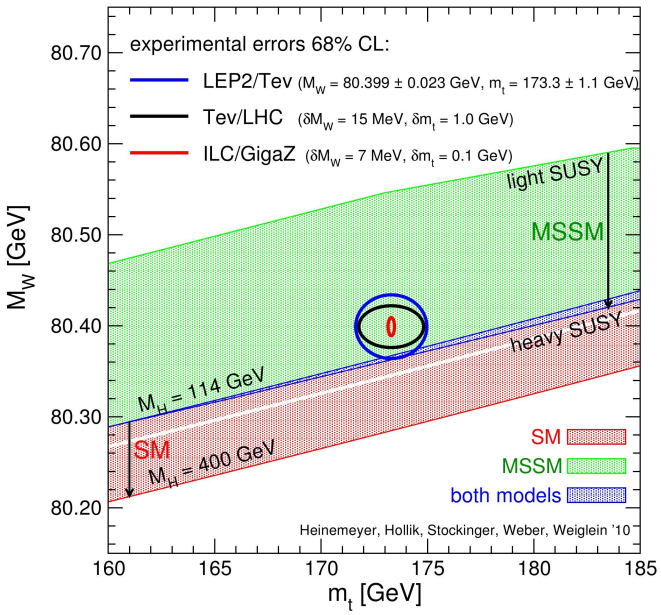

Figure 1.9.: The mass of the Higgs Boson in dependence of the top quark and the W boson mass. The ellipses illustrate the errors of m_t and m_W, as well as their decrease in future accelerators. Plot taken from [4]

result [13]:

$$\Delta r^{\text{top}} = -\frac{3\sqrt{2}G_F \cot^2\theta_W}{16\pi^2} \cdot m_t^2 \qquad (\text{for } m_t \gg m_b) \tag{1.7}$$

$$\Delta r^{\text{Higgs}} = \frac{3\sqrt{2}G_F m_W^2}{16\pi^2} \cdot \left(\ln\frac{m_H^2}{m_W^2} - \frac{5}{6}\right) \qquad (\text{for } m_H \gg m_W). \tag{1.8}$$

Therefore, precise measurement of the masses m_W, m_Z, m_t (see more for top quark mass measurement on 1.1) leads to a constraint of the Higgs mass. The dependence on the top quark mass is much higher as it enters quadratic, whereas the Higgs mass only logarithmically. The illustration 1.9 shows the currently preferred Higgs mass from the measurements of m_t and m_W at 95% confidence level, and the decreasing of the uncertainty for the new generations of particle accelerators, the LHC and the ILC (International Linear Collider). BSM particles would lead to additional radiative corrections in Equation 1.6 and lead to a different dependence of the three masses.

Improvement of Gluon PDFs

The second important role of the top quark, concerning the Higgs Boson, originates from their similar production processes. The Higgs Boson is mainly produced via two incoming gluons and

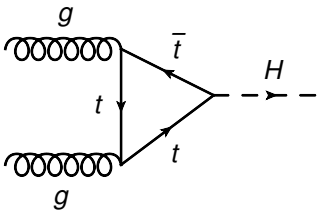

Figure 1.10.: Two gluons produce a Higgs Boson via a top quark Loop. This is the main production channel for the Higgs Boson.

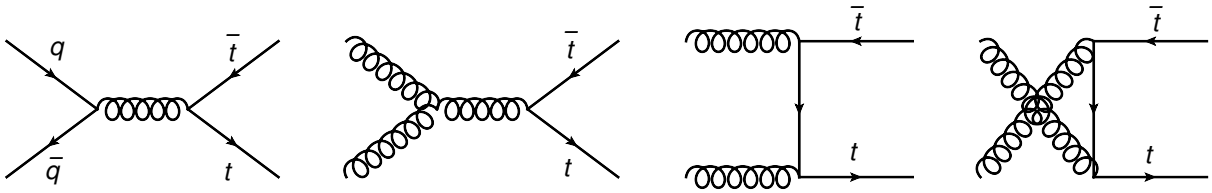

Figure 1.11.: Leading order (LO) Feynman diagrams for top quark pair production. The first diagram is the quark anti-quark annihilation channel, the following three diagrams represent the gluon fusion channel.

a top quark loop (see Figure 1.10) and therefore needs precise gluon luminosity (see Equation 2.3) to predict its cross sections. The top quark, on the other hand, is produced in two different channels, but at the LHC, the gluon fusion channel dominates with 90% (see Figure 1.11 and for more detailed information on top quark production see Section 2.2).
Figure 1.12 shows the ratio between gluon-luminosities of different working groups and their uncertainty as a function of x for $\sqrt{s} = 7$ TeV. The error bands for each set are of similar size, but at small values for x the different PDFs sets do not even overlap. For example, as shown in the Figure 1.12, top quark pair production starts at $x \sim 0.05$ at the LHC and there is a huge discrepancy of about 10% between the different luminosities.

According to [14] details of heavy flavor treatment account for some deviation, as well as the different values of α_s used in the various groups. ABKM and MSTW fit their value for α_s from their data. In addition, the MSTW collaboration provides its PDF sets for different external values forα_s as well. At high x values, jet data from the Tevatron constrain the gluon PDFs. These data are not included into ABKM09, but they claim that their effect is small. Although arguments for the differences of the PDF sets are given in [14] [15] [16], there is an ongoing discussion among experts regarding a complete solution of the discrepancies. At a Higgs mass of $m_H = 165$ GeV the MSTW parton distribution functions give a prediction of the cross which is 35% larger than ABKM (~ 4 standard derivations). Using ABKM PDFs would halve the Higgs mass exclusion area determined by the Tevatron.

Thus, two challenges arise for the top quark pair production. A precise calculation and mea-

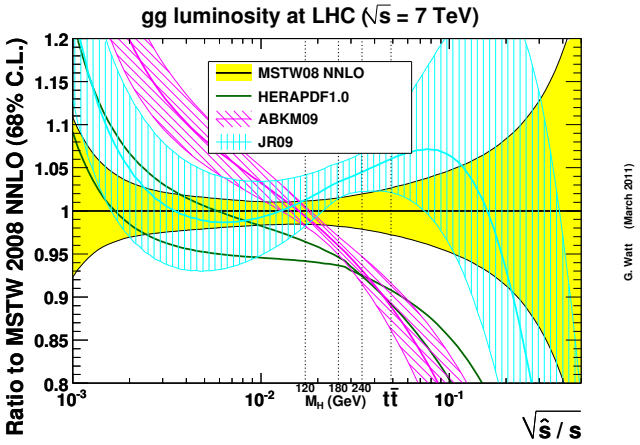

Figure 1.12.: The NNLO of gluonluminosity predicted by several PDF fitting collaborations. Each gluon luminosity is normalized to the central value of the MSTW08 luminosity. Plot taken from [17]

surement would dicriminate between the different PDFs sets. A second task is the reduction of the error bands of the PDFs. The goal is a measurement of the PDFs to a precision of $\sim 3\%$ for $x \geq 0.05$.
Hence, a precise calculation and measurement of the top quark cross section improves the gluon PDFs for large x and permits a better prediction of the Higgs cross section and its mass.

1.4. Resumé

In the preceding sections, different motivations for a high precision calculation of the top quark pair cross section at the LHC have been illustrated. In the domain of the SM, it can be used to improve the determination of the top quark mass and the gluon PDFs. In the area of BSM physics, top quark pair decays are the main background to many new physics searches. Moreover new physics can be observed in the top quark channel directly. An NNLO calculation could solve the charge asymmetry puzzle as well.

The experimentalists claim that they will measure the top quark pair cross section at the LHC to a precision of 5%, even 3% seems possible [3]. On the theoretical side, the cross section is known at NLO. The uncertainty, estimated by scale variation is 15%. Different groups have improved these predictions by using soft gluon and threshold resummation and could reduce the error by about 10%. Nonetheless, a complete NNLO cross section would reduce the uncertainty to 3%-4% and is highly desirable.

2. State of the Art of Top Quark Pair Production

2.1. Factorization

2.1.1. The Factorization Theorem

The factorization theorem is crucial for reliable precision calculations in QCD. It states that the total cross section can be factorized into a short distance (or hard) part $\hat{\sigma}_{t\bar{t}}$ and a long distance (or soft) part, called parton distribution function (PDF) $\phi_{i,A}$ [18]. The PDFs describe the probability $\phi_{i,A}(x_1, \mu_F)$, that a parton i can be found inside the hadron A with a percentage x_1 of the longitudinal momentum of the hadron at a scale μ_F.

$$\sigma(s, m_t) = \sum_{i,j} \int_0^1 \int_0^1 dx_1 dx_2 \phi_{i,A}(x_1, \mu_F) \phi_{j,B}(x_2, \mu_F) \hat{\sigma}_{ij \to t\bar{t}}(\frac{m_t^2}{\hat{s}}, \mu_R, \mu_F, \alpha_s(\mu_R)) \tag{2.1}$$

Equation 2.1 is valid up to terms which are suppressed by the relevant scale of the process. A and B are the colliding hadrons, whereas i and j are the scattering partons within these hadrons. s represents the accelerator energy, $\hat{s} = x_1 x_2 s$ is center of mass energy of the involved partons, α_s stands for the coupling constant, μ_F the factorization scale and μ_R the renormalization scale.

The theorem separates the short and long distance parts. Interactions, which occur long before the hard scattering process, are factored out and absorbed in the description of the incoming hadrons. The remaining hard part contains only high momentum transfer and does only depend on the partons involved in the hard scattering processes yet not on the type of the incoming hadrons. The short distance cross section can be calculated perturbatively, on the contrary the PDFs are universal and obtained experimentally.

The separation of the total cross section in the short and long distance part is not unique. It is possible to shift finite terms between these two. The scale μ_F divides these two parts. Partons emitted with a smaller transverse momentum than μ_F can be thought of being part of the hadron structure which are absorbed in the PDFs. Partons with larger transverse momentum than μ_F belong to the short distance cross section. The hard scattering process additionally depends on the renormalization scale, which is introduced in dimensional regularization to conserve the mass dimension of the coupling constant α_s. Both scales can be given arbitrary values, but the result for the total cross section at a given order is not allowed to depend on these values. This means

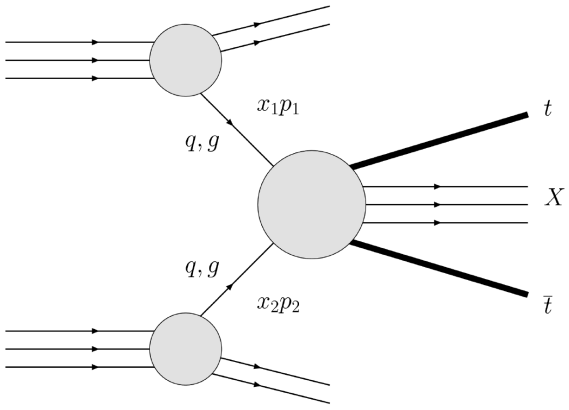

Figure 2.1.: Top quark pair production in the factorization picture. Figure taken from [2].

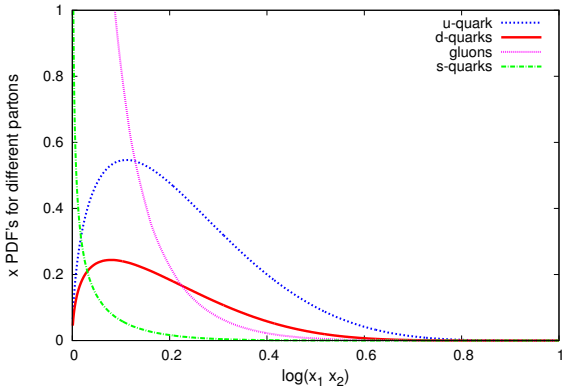

Figure 2.2.: The PDFs for the LHC at 14 TeV and $m_F = M_{top} = 173.1\text{GeV}$.

$$\frac{d\,\sigma(s, m_t)}{d\mu_F} = \frac{d\,\sigma(s, m_t)}{d\mu_R} = 0. \tag{2.2}$$

Nevertheless, at a finite order the partonic cross section depends on the scales. Both scales can be chosen independently, but should be given a value of the order of the relevant scale of the process $Q^2 = -q^2$ (see Figure 2.1) to avoid large logarithms of the form $\log(Q^2/\mu_F^2)$ and $\log(Q^2/\mu_R^2)$. Often both scales are set to a common value μ. The higher the order in the α_s-expansion, the weaker is the dependence of the PDFs and the short distance cross section on the scales. The variation of the scales can be used to estimate the error of a fixed order calculation. It is common to vary μ between $Q^2/2$ and $2\,Q^2$ to obtain an estimation for the scale uncertainty of the total cross section.

2.1.2. Parton Distribution Functions

The parton distribution functions (Figure 2.2) $\phi_{i,A}(x_1, \mu_F)$ indicates the probability to find a parton i in the hadron A with the momentum fraction $x_i = \frac{p_i}{p_A}$, whereas p is the longitudinal momentum of the particle. They depend on the factorization scale and of the kind of the hadron (e.g. proton, anti-proton, neutron).
In the section above it is illustrated that the long and short distance effects can be separated. The PDFs are therefore universal and can be measured in an experiment, for example with deep inelastic scattering, like it is done at HERA and afterwards it can be reused for pp collisions at the LHC.

The best source to determine PDFs experimentally are deep inelastic scattering experiments. For NNLO calculations it is important to have NNLO PDFs available, as large cancellations can occure between the PDFs and the short distance cross section. Three ingredients are necessary for NNLO PDFs. Firstly, high precision measurements as done at HERA (deep inelastic scattering). Secondly, the knowledge of the hard scattering cross section of the measured process at NNLO. Thirdly, NNLO PDFs can be extracted at a given scale. The splitting functions at NNLO-level are necessary [19, 20] to evaluate the PDFs to an arbitrary scale, using the DGLAP equations [21].

At the moment ABKM09, MSTW08 and JR08 PDFs are available at NNLO [22]. Although the error in the quark PDFs is in general smaller than for the gluons PDFs, the uncertainty for the Tevatron (where the quark production channel dominates) is higher than for the LHC (where the gluon channel dominates). Due to the lower energy of the Tevatron, only quarks with a high momentum fraction can produce a top quark pair and the uncertainty in these x-regions of the quark PDFs is large. PDF sets differ by the value of α_s, the choice of the parton parametrization and the included experimental data sets. Only with exact PDFs high precision predictions for cross sections are possible. The uncertainty of the PDFs is the largest contribution to the overall error of the top quark pair production cross section (see Chapter 1, Figure 1.12).

For hadron-hadron collisions it is convinient to rewrite Equation 2.1 in terms of the flux (Figure 2.3), which only depends on the PDFs.

$$\Phi_{ij}(\tau, \mu_F, \mu_R) = \tau \sum_{i,j} \int_0^1 \int_0^1 dx_1\, dx_2\, \phi_i(x_1, \mu_F)\, \phi_i(x_2, \mu_F)\, \delta(x_1 x_2 - \tau) \tag{2.3}$$

Thus the factorization theorem changes to:

$$\sigma(s, m_t^2) = \sum_{i,j} \int_{p_H}^1 \frac{d\tau}{\tau}\, \Phi_{ij}(\tau, \mu_F)\, \hat{\sigma}_{ij \to t\bar{t}}(\tau s, \mu_R, \mu_F, \alpha_s(\mu_R)) \tag{2.4}$$

In Figure 2.3 the luminosity is given for the LHC and for the Tevatron. Due to the fact that the Tevatron is a proton anti-proton collider more anti-quarks are available for the annihilation channel and it dominates by 90%. As it can be seen the gluon luminosity grows stronger with

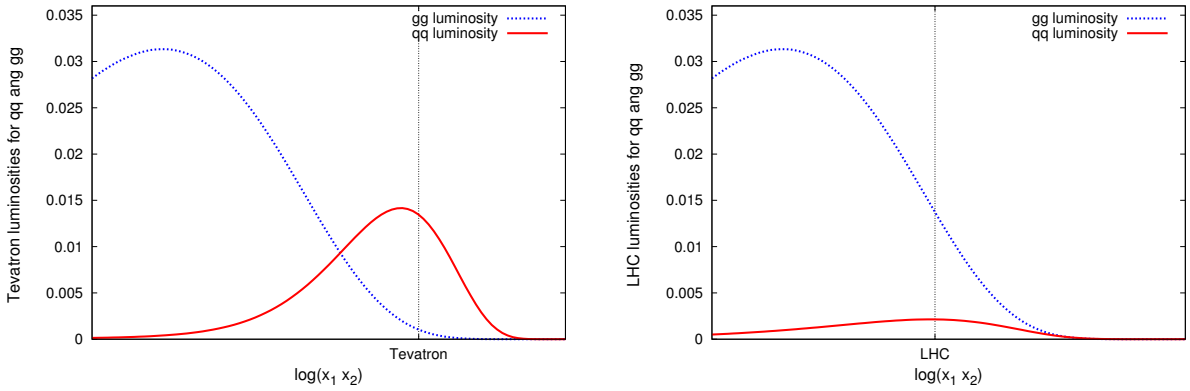

Figure 2.3.: gg and $\overline{q}q$ luminosity at the Tevatron and the LHC respectively.

higher accelerator energies. This fact and the absence of a large amount of anti-quarks lead to a domination of the gluon fusion channel of 90%.

2.1.3. Hard Scattering

The partonic cross section $\hat{\sigma}_{ij}$ can be calculated perturbatively and only depends on the scattering partons and the dimensionless scaling function $\rho = \frac{4m_t^2}{s}$. Setting $\mu_F = \mu_R = \mu$ leads to

$$\hat{\sigma}_{ij}(\rho, m_t^2, \alpha_s(\mu^2), \mu) = \frac{\alpha_s^2(\mu)}{m_t^2} \sum_{k=0}^{\infty} (4\pi\alpha_s(\mu))^k \sum_{l=0}^{2k} f_{ij}^{kl}(\rho) \log^l \left(\frac{\mu^2}{m_t^2}\right) . \tag{2.5}$$

k represents the order of the calculation ($k = 0 \to \text{LO}, ...$). The logarithms emerge in dimensional regularization from the expansion of $(\frac{\mu^2}{m_t^2})^\epsilon$ together with the ϵ-poles of the order $\frac{1}{\epsilon^{2n}}$ from the n-loop calculation. In the total cross section the infrared poles cancel with the infrared poles from real radiation, leaving only $\log \beta$ up to the order n. These remaining poles are canceled by the renormalization procedure or are absorbed into the PDFs. Explicit expressions for f_{ij}^{00} are [23]:

$$f_{q\overline{q}}^{00}(\rho) = \frac{\pi}{6} \frac{T_R C_F}{N_c} \beta\rho \, (2 + \rho) \tag{2.6}$$

$$f_{gg}^{00}(\rho) = \frac{\pi}{12} \frac{T_R}{N_c^2 - 1} \beta\rho \left\{ 3C_F \left[(4 + 4\rho - 2\rho^2) \frac{1}{\beta} \ln \frac{1+\beta}{1-\beta} - 4 - 4\rho \right] + C_A \left[3\rho^2 \frac{1}{\beta} \ln \frac{1+\beta}{1-\beta} - 4 - 5\rho \right] \right\} \tag{2.7}$$

where $\beta \equiv \sqrt{1-\rho}$ and $f_{ij}^{00}(\rho) = 0$ for all the other parton channels. Notice that close to the threshold ($\rho \to 1$, $\beta \to 0$) the LO contributions $f_{ij}^{00}(\rho)$ vanish due to the phase space suppression.

The functions $f_{q\bar{q}}^{1l}(\rho)$ and $f_{gg}^{1l}(\rho)$ have been calculated numerically in [24, 25] and analytically in [26]. The analytic results for the threshold region ($\rho \to 1$, $\beta \to 0$) at NLO are [24, 25]:

$$f_{q\bar{q}}^{00}(\rho) + f_{q\bar{q}}^{01}(\rho) \ln \frac{\mu^2}{m_t^2} = \frac{1}{4\pi^2} f_{q\bar{q}}^{(0)}(\rho) \left\{ \left(C_F - \frac{1}{2} C_A \right) \frac{\pi^2}{2\beta} + 2C_F \ln^2(8\beta^2) \right. \tag{2.8}$$
$$\left. -(8C_F + C_A) \ln(8\beta^2) - 2C_F \ln(4\beta^2) \ln \frac{\mu^2}{m^2} + C_2 \left(\frac{\mu^2}{m^2} \right) + \mathcal{O}(1-\rho) \right\},$$

$$f_{gg}^{00}(\rho) + f_{gg}^{01}(\rho) \ln \frac{\mu^2}{m_t^2} = \frac{1}{4\pi^2} f_{gg}^{(0)}(\rho) \left\{ \frac{N_c^2 + 2}{N_c(N_c^2 - 2)} \frac{\pi^2}{4\beta} + 2C_A \ln^2(8\beta^2) \right. \tag{2.9}$$
$$\left. -\frac{(9N_c^2 - 20)C_A}{N_c^2 - 2} \ln(8\beta^2) - 2C_A \ln(4\beta^2) \ln \frac{\mu^2}{m^2} + C_3 \left(\frac{\mu^2}{m^2} \right) + \mathcal{O}(1-\rho) \right\},$$

The result for all other parton channels is of the order $\mathcal{O}(\beta)$. The equations 2.8 and 2.9 allow to get an understanding of the structure of the total cross section.
At very low values for β the Coulomb interactions, which behave like $1/\beta$, dominate. The remaining logarithmic divergent terms $\ln(\beta)$ and $\ln^2(\beta)$ are produced by soft gluon radiation and dominate the region close to the threshold. The right hand sides of Equations 2.8 and 2.9 contain as well the constants C_2 and C_3, due to large momentum virtual corrections. These constant terms can only be determined by calculating the total cross section at NLO (in particular they cannot be determined using soft gluon resummation) and are given in [24, 23]. All terms, which are of higher order in β than 0 and are important in regions further away from the threshold.

Deriving numerical results for $f_{q\bar{q}}^{2l}(\rho)$ and $f_{gg}^{2l}(\rho)$ are the main goals of this thesis.

2.2. Dominant Effects

Instead of calculating the complete amplitude at NNLO, different working groups improved the NLO prediction by identifying and calculating dominant effects. In particularly these are soft-gluon resummation and Coulomb interactions. This section will briefly present these dominant effects and sketch the corresponding methods to calculate them. For detailed information references will be given.

Soft gluon radiation and Coulomb interactions can add large corrections to the total cross section and even spoil the convergence of the series Equation 2.5, e.g. in Higgs production. Techniques have been developed to resum these contributions and hence to reduce the uncertainty of the total cross section. There are two main techniques used today: The first is the calculation of the cross section in Mellin-space. This method was first successfully applied to the Drell-Yan process 15 years ago. The second is a more recent development. The resummation is accomplished in x-space [5] (SCET formalism) and turned out to be a fruitful approach for proving factorization theorems. The resummation of the large logarithms is done by evaluating the evolution equations. Different groups improved the top quark pair cross section by soft gluon resummation and published their results [27, 28, 29, 30, 31, 32]. These resummations differ by

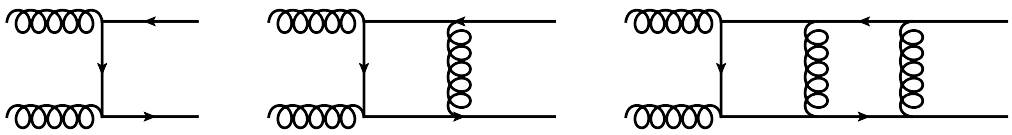

Figure 2.4.: Ladder diagrams for $gg \to t\bar{t}$. Each exchanged Coulomb gluon contributes with α_s/β.

the order of resummation (NLL, NNLL), included constants and using the x or the Mellin space formalism. Moreover there are different prescriptions and different kinematic limits where the resummation can be performed.

2.2.1. Soft Gluon and Coulomb Singularities

Close to the threshold ($\rho \to 1$, $\beta \to 0$) terms like $\alpha_s \log^2 \beta$ and $\frac{\alpha_s}{\beta}$ are large even if α_s is small. Therefore these contributions have to be resumed to all orders. In this section I want to explain which diagrams generate divergent terms of the form $1/\beta$ and $\log \beta$.

Coulomb Singularities

Coulomb singularities arise from the ladder diagram (Figure 2.4). Each additional loop generates an additional power of $1/\beta$. As can be seen easily in NRQCD[1]. The variable β is proportional to the velocity of the top quark v. The simplest example is the vertex presented in Figure 2.5 (left). The Feynman integral is

$$\sim \alpha_s \int d^4k \, \frac{1}{k^2} \frac{\not{k} + \not{p}_1 + m}{(k+p_1)^2 - m^2} \frac{\not{k} - \not{p}_2 + m}{(k-p_2)^2 - m^2} \, , \tag{2.10}$$

where p^0 and $\vec{p}$ scale in the non-relativistic limit as $p^0 \sim m + mv^2$ and $\vec{p} \sim mv$, respectively. The main contribution to the integral derives from the regime, in which k scales like $k^0 \sim mv^2$ and $\vec{k} \sim mv$. Hence d^4k behaves like m^4v^5 and the complete Feynman integral like:

$$\sim \alpha_s \; m^4 v^5 \, \frac{1}{m^2 v^2} \, \frac{m}{m^2 v^2} \, \frac{m}{m^2 v^2} \sim \frac{\alpha_s}{v} \sim \frac{\alpha_s}{\beta} \tag{2.11}$$

Each additional Coulomb gluon generates an additional $\frac{\alpha_s}{\beta}$ term. In higher order diagrams a $\log \beta$ can be generated as well. Close to threshold, these terms cause a singular behaviour of the partonic cross section. The divergent behaviour of the double virtual corrections can be seen in Figure 4.2 (left). These Coulomb corrections can be resumed.

[1] non-relativistic QCD

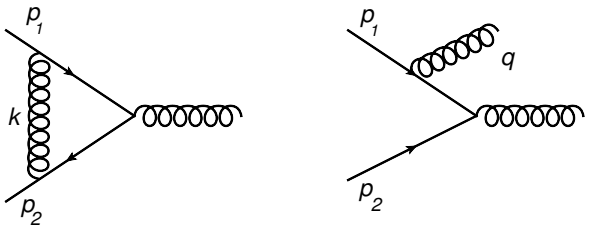

Figure 2.5.: Left: Coulomb singularity generating the term $\sim \alpha_s/\beta$. Right: Soft and collinear singularity producing the term $\log^2 \beta$.

Divergences from Soft Gluon Radiation

Figure 2.5 (right) shows a tree-level diagram with one radiated gluon. The propagator can be written in the limit, where the gluon is soft, as

$$\frac{1}{(p_1 - q)^2 - m^2} \sim \frac{1}{2\, p_1\, q} \sim \frac{1}{2\, |p_1||q|\, \cos\theta}\,. \tag{2.12}$$

Evidently, there is a divergence if the gluon momentum $|q|$ becomes soft and $\cos\theta$ generates a singularity if both particles are collinear. It is well known, that both lead to a logarithmic singularity in the squared amplitude $\mathcal{A}$, i.e.

$$\mathcal{A} \sim \mathcal{A}_0\, \alpha_s \int_\lambda^{\beta^2} \frac{dq_0}{q_0} \int_\lambda^{\beta^2} \frac{d\theta}{\theta} \sim \mathcal{A}_0\, \alpha_s\, \log^2 \beta \tag{2.13}$$

Due to the smallness of the phase space, i.e. $\beta \sim 0$, the generated $\log\beta$ are large and can spoil the series expansion in α_s. The large logarithms have to be calculated. The infrared singularities for $\lambda \to 0$ cancel with the infrared divergenties from the virtual contributions.

2.2.2. Exponentiating the Soft Gluon Contributions in Mellin-Space

My derivation of the exponentiation Formula 2.29 closely follows the papers [33, 34].

Soft-Gluon Effects The finite energy resolution of any particle detector implies that physical cross sections are calculated inclusively, by summing over an arbitrary number of soft final state particles. Infrared divergencies, which arise from the emission of undetected real gluons are exactly cancelled by the contributions of the virtual gluons in higher order perturbative QCD, resulting in finite cross sections. Let $1 - z$ denote the fraction of the center of mass energy $\hat{s}$ carried by unobserved final state particles. Clearly, close to the threshold $1 - z$ goes to zero. Virtual (v) and real (r) gluons affect the cross section by the following emission probabilities [33]:

$$\frac{dw_v(z)}{dz} = -2\,C\,\alpha_s\,\delta(1-z)\int_0^{1-\epsilon}\frac{dz'}{1-z'}\ln\frac{1}{1-z'} \tag{2.14}$$

$$\frac{dw_r(z)}{dz} = 2\,C\,\alpha_s\,\frac{1}{1-z}\ln\frac{1}{1-z}\,\Theta(1-z-\epsilon) \tag{2.15}$$

C depends on the process. The double logarithms in Equation 2.14 originate from bremsstrahlungs and collinear radiation. The unphysical cutoff ϵ is the minimal energy fraction of both gluons. After combining the real and the virtual parts the physical limit $\epsilon \to 0$ can be safely performed and result in:

$$\frac{dw(z)}{dz} == \frac{dw_r(z)}{dz} + \frac{dw_v(z)}{dz} = 2\,C\,\alpha_s\left[\frac{1}{1-z}\ln\frac{1}{1-z}\right]_+ , \tag{2.16}$$

where $[g(z)]_+$ stands for the plus distribution:$\int_x^1 dz\ f(z)\,[g(z)]_+ \equiv \int_x^1 dz[f(z)-f(1)]g(z)$. To derive the emission probability for a virtual or soft gluon Equation 2.16 is integrated from the energy fraction x of the tagged final state to one. In the case of heavy quark production x is $4m^2/\hat{s}$. Therefore the soft gluon correction to the total cross section is given by [33]

$$\int_x^1 dz\frac{dw(z)}{dz} = -\,a\,\ln^2(1-x)\ , \tag{2.17}$$

which denotes the finite heritage of the cancellation infrared singularity. If the production process is close to threshold ($1-z \to 0$ or $x \to 1$) the contributions of Equation 2.17 are large. This is due to the small-sized phase-space for additional real gluon radiation and therefore the radiative part is strongly suppressed. This results in an imbalance between the two parts and large contributions of the form

$$C_{mn}\alpha_s^n \log^m \beta \quad \text{with } m \leq 2n \tag{2.18}$$

remain. Terms of the form $\alpha_s \log^2 \beta \geq 1$ are large close to threshold even if α_s is small. The perturbative series in α_s is spoiled in this phase-space region. As a solution the contributions from the large logarithms can be resumed to all orders in α_s and used to improve the theoretical prediction and scale dependence [34].

Resummation and Exponentiation As shown in Formula 2.1 the cross section can be calculated by convoluting the partonic cross section $\hat{\sigma}_{ij\to t\bar{t}}$ with the PDFs ϕ_i as

$$\sigma_{ij\to t\bar{t}}(\rho, m_t^2) = \int_0^1\int_0^1 dx_1 dx_2 \phi_i(x_1)\phi_j(x_2)\Delta_{ij\to t\bar{t}}\left(\frac{\rho}{x_1x_2}, m_t^2, \alpha_s\right)\hat{\sigma}^0_{ij\to t\bar{t}}\left(\frac{\rho}{x_1x_2}, m_t^2\right) , \tag{2.19}$$

where $\rho = \frac{4m_t^2}{s}$, s is the square of the center of mass energy, $\hat{\sigma}^0$ is the Born-level cross section for the corresponding process and $\Delta_{ij\to t\bar{t}}$ takes into account all radiative corrections. The latter can be computed in perturbative QCD. The scale dependence is suppressed. If the top quark

pair is produced close to the threshold $\rho \to 1$, the radiative corrections in $\Delta_{ij\to t\bar{t}}\left(\frac{\rho}{x_1 x_2}, m_t^2, \alpha_s\right)$ are dominated by soft-gluon radiation as presented in Equation 2.16. It is conviniently to do the resummation of soft-gluon effects in Mellin-space. The Mellin transformation for any fixed ρ is defined as

$$\sigma_{ij}(N, m_t^2) = \int_0^1 d\rho\ \rho^{N-1}\ \sigma_{ij}(\rho, m_t^2) \tag{2.20}$$

and its inverse

$$\sigma_{ij}(\rho, m_t^2) = \frac{1}{2\pi i} \int_{C-i\infty}^{C+i\infty} dN\ \rho^{-N}\ \sigma_{ij}(N, m_t^2)\ , \tag{2.21}$$

where the constant C, that defines the integration contour, has to be chosen on the right of all the possible singularities of the N-moments, so that $\sigma_{ij}(N, m_t)$ are analytic functions in the right half-plane of the complex variable N. The threshold corresponds to $N \to \infty$. In this limit the weight factor ρ^{N-1} only contributes, if ρ is very close to 0.

In the Mellin-space the convolution of the PDFs and the partonic cross section transforms into a product

$$\sigma_{ij}(N, m_t^2) = \phi(N, m_t^2)\phi(N, m_t^2)\Delta(N, \alpha_s(m_t^2))\hat{\sigma}^0_{ij\to t\bar{t}}\left(\frac{\rho}{x_1 x_2}, m_t^2\right) \tag{2.22}$$

The radiative factor $\Delta(N, \alpha_s(m_t^2))$ can be calculated as

$$\Delta(z, \alpha_s) = \delta(1-z) + \sum_{n=1}^{+\infty} \int_0^1 dz_1 \dots dz_n\ \frac{dw_n(z_1, \dots, z_n)}{dz_1 \dots dz_n}\ \Theta_{\mathrm{PS}}(z; z_1, \dots, z_n)\ , \tag{2.23}$$

where dw_n (the probability to produce n soft-gluons) is integrated over the available phase space region denoted as $\Theta_{\mathrm{PS}}(z; z_1, \dots, z_n)$.
There are two basic properties of QCD which allow all-order resummation of soft gluons: dynamic and kinematic factorization. The first states that the emission of a gluon $dw_n(z_1, \dots, z_n)$ does not influence the probability of radiating another gluon, assuming the first one is sufficiently soft. So in the soft limit the multi-gluon amplitude can be factorized in the single-gluon emission probabilities $dw(z_i)$ of Equation 2.16

$$\frac{dw_n(z_1, \dots, z_n)}{dz_1 \dots dz_n} \simeq \frac{1}{n!} \prod_{i=1}^{n} \frac{dw(z_i)}{dz_i}\ . \tag{2.24}$$

The kinemtaic factorization is responsible for the simplification of the phase-space. Normally, the phase-space function depends not trivially on the multi-gluon phase-space, yet in the case of total cross sections, longitudinal-momentum conservation is the only relevant constraint. The phase-space does not factorize in x-space, but in N-space

$$\Theta_{\mathrm{PS}}(z; z_1, \ldots, z_n) = \delta(z - z_1 \ldots z_n) \tag{2.25}$$

$$\Theta_{\mathrm{PS}}(N) = \int_0^1 dz\, z^{N-1}\, \delta(z - z_1 \ldots z_n) \;=\; z_1^{N-1} \ldots z_n^{N-1} \tag{2.26}$$

Using the last two simplifications for Equation 2.23 the result is:

$$\Delta(N, \alpha_s) = \int_0^1 dz\, z^{N-1} \Delta(z, \alpha_s) \tag{2.27}$$

$$= 1 + \sum_{n=1}^{+\infty} \frac{1}{n!} \left(\int_0^1 dz\, \frac{dw(z)}{dz} z^{N-1} \right)^n = \exp\left(\int_0^1 dz_1\, \frac{dw(z)}{dz} z^{N-1} \right) . \tag{2.28}$$

$dw(z)$ can be replaced using Equation 2.16 resulting in

$$\Delta(N, \alpha_s) = \exp\left(C\, \alpha_s \int_0^1 dz \frac{z^{N-1} - 1}{1 - z} \ln \frac{1}{1 - z} \right) \tag{2.29}$$

$$= \exp\left(C'\, \alpha_s\, (\ln^2 N + \mathcal{O}(\ln N)) \right) . \tag{2.30}$$

Equation 2.30 is valid in massless QED. In QCD complications arise due to the color structure and from gluon radiation from gluon lines. Moreover the top quark cannot be assumed to be massless. Nevertheless, the essential features stay the same. Indeed, from gauge invariance and unitarity follows that for Drell-Yan and similar total cross sections a generalized exponentiation theorem is valid [33, 35, 36, 37, 38]. Using β instead of z, the partonic cross section $\hat{\sigma}_{t\bar{t}}(\beta)$ can be expanded in a series of enhanced radiative corrections [38]:

$$\hat{\sigma}_{t\bar{t}}(\beta) \;= \hat{\sigma}_{t\bar{t}}^{(0)} \textstyle\sum_{k=0} \left(\frac{\alpha_s}{\beta}\right)^k \exp\Big[\underbrace{\ln\beta\, g_0(\alpha_s \ln\beta)}_{\text{(LL)}} + \underbrace{g_1(\alpha_s \ln\beta)}_{\text{(NLL)}} + \underbrace{\alpha_s g_2(\alpha_s \ln\beta)}_{\text{(NNLL)}} + \ldots \Big]$$
$$\times \Big\{ 1(\mathrm{LL}, \mathrm{NLL}); \alpha_s, \beta(\mathrm{NNLL}); \ldots \Big\} \tag{2.31}$$

$\hat{\sigma}_{t\bar{t}}^{(0)}$ is the Born cross section. The different orders of resummation refer to

$$\mathrm{LL}\, \alpha_s \Big\{ \tfrac{1}{\beta}, \ln^2\beta \Big\};\; \alpha_s^2 \Big\{ \tfrac{1}{\beta^2}, \tfrac{\ln^2\beta}{\beta}, \ln^4\beta \Big\}; \ldots$$
$$\mathrm{NLL}: \quad \alpha_s \ln\beta;\; \alpha_s^2 \Big\{ \tfrac{\ln\beta}{\beta}, \ln^3\beta \Big\}; \ldots , \tag{2.32}$$

where $\alpha_s \log\beta$ is assumed to be of the order 1. Divergent terms (e.g. soft gluon effects) are resummed in the exponential function, whereas the terms in the curly bracket can be calculated perturbatively. The hadronic total cross section is obtained by integrating the partonic cross section from $\beta = 0$ up to $\beta_{\max} = (1 - 4m_t^2/s)^{1/2}$, weighted by the parton luminosity.

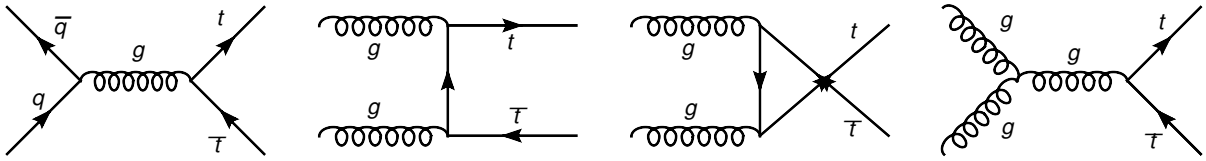

Figure 2.6.: LO Feynman diagrams for the $q\bar{q}$ annihilation and the gluon fusion channel.

2.2.3. Threshold Expansion up to $\mathcal{O}(\beta)$

Performing a threshold expansion of the total cross section in Formula 2.31 around the threshold ($\beta \sim 0$) up to $\mathcal{O}(\beta)$ neglects all terms of β^n with $n \geq 1$. The neglected terms at LO and NLO are restored by matching the resummed result to the exact result (see Section 2.2.1). Nevertheless, the expansion is soley valid in the area close to thr threshold, where $\beta \sim 0$. At the Tevatron and LHC this is questionable, as the $t\bar{t}$ mass distribution has a peak at 380 GeV for a 7 TeV LHC [38] corresponding to $\beta \sim 0.4$.
The results from the threshold expansion from Section 2.2.3 can be improved through adding terms which are resummed to all orders. To avoid double counting, only resumed terms of higher order than NLO are included. This is achieved by subtracting the up to NLO expanded resumed contribution.

$$\sigma_{t\bar{t}}^{\text{NNLL+NLO}} = \sigma_{t\bar{t}}^{\text{NLO}} + \sigma_{t\bar{t}}^{\text{NNLL}} - \sigma_{t\bar{t}}^{\text{NNLL}}\Big|_{\text{NLO}} \tag{2.33}$$

Similar for the NNLO. The NNLL contribution is added, but (again to avoid double counting) its NNLO expansion is subtracted.

$$\sigma_{t\bar{t}}^{\text{NNLL+NNLO}} = \sigma_{t\bar{t}}^{\text{NNLO}} + \sigma_{t\bar{t}}^{\text{NNLL}} - \sigma_{t\bar{t}}^{\text{NNLL}}\Big|_{\text{NNLO}} \tag{2.34}$$

2.3. Fixed Order Approximation

2.3.1. Leading Order

The diagrams for the top quark pair production at leading order are shown in Figure 2.6. One diagram contributes in the $q\bar{q}$ annihilation channel, three in the gluon fusion channel. At the Tevatron the first dominates the production rate with 90%, at the LHC the gluon fusion channel dominates with 90% (see Chapter 1). The results were already calculated analytically in the late 70's having charm quark production in mind. For the quark annihilation channel the result is

$$\frac{d\sigma_{q\bar{q}\to t\bar{t}}}{d\,t} = \frac{4\pi\alpha_s^2}{9s^4}[(m^2-t)^2 + (m^2-u)^2 + 2m^2 s], \tag{2.35}$$

and the three gluon diagrams result in

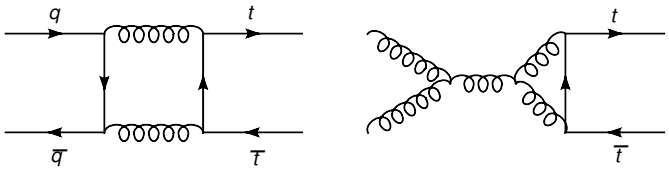

Figure 2.7.: Example diagrams for NLO virtual corrections.

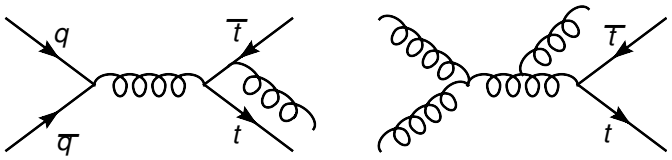

Figure 2.8.: Example diagrams for NLO real corrections.

$$\frac{d\sigma_{gg\to t\bar{t}}}{dt} = \frac{\pi\alpha_s^2}{8s^2}[\frac{6(m^2-t)(m^2-u)}{s^2} - \frac{m^2(s-4m^2)}{3(m^2-t)(m^2-u)} + \frac{4}{3}\frac{(m^2-t)(m^2-u)-2m^2(m^2+t)}{(m^2-t)^2} + \frac{4}{3}\frac{(m^2-t)(m^2-u)-2m^2(m^2+u)}{(m^2-u)^2} - 3\frac{(m^2-t)(m^2-u)-m^2(u-t)}{s(m^2-t)^2} - 3\frac{(m^2-t)(m^2-u)-m^2(t-u)}{s(m^2-u)^2}], \tag{2.36}$$

where, s,t,u are the Mandelstamm variables[2]. The scale uncertainty of $\sigma_{t\bar{t}}^{\mathrm{LO}}$, deriving from scale variation between $\mu = \frac{1}{2}m_T$ and $\mu = 2m_T$ is quite large (about 50%). Additional error sources are the PDFs, the top quark mass and $\alpha_s(M_z)$.

2.3.2. Next to Leading Order

A complete NLO calculation for the total top quark pair production cross section was done by Nason, Dawson and Ellis in 1987 [24], and two years later the same was done for the differential cross section [39]. The results agreed with Beenakkers's [25], obtained one year later. In 2008 the calculation was confirmed analytically by M. Czakon and A. Mitov and the results are given in [26]. The calculation contains the evaluation of 1-Loop integrals and tree-level integrals with one real radiation in both channels. Figure 2.7 shows two examples of the virtual diagrams, one in the $q\bar{q}$ and one in the gg-channel. Figure 2.8 displays two diagrams of the real contributions. The NLO calculation increases the value for the total cross section $\sigma_{t\bar{t}}$ by 25% for the Tevatron and by 50% for the LHC with respect to the LO calculation. The enlargement is due to an overall normalization factor. The shapes of the differential contributions stay the same. The NLO calculation reduces the uncertainty to 15%. The differential cross section, including off-shell effects and the leptonic decays are computed in [40, 41].

[2]These are defined as usual: $s = (p_1 + p_2)^2, t = (p_1 - p_3)^2, u = (p_1 - p_4)^2$.

2.3.3. Further Corrections

QCD corrections The process $qg \to t\bar{t}q$ has the highest flux at the LHC and therefore should be important. However, the parton level cross section starts at α_s^3. As it was shown in Section 2.1.3, the α_s^3 contributions is of the order $\mathcal{O}(\beta)$, which means it is 0 at the threshold and enhancements, like Coulomb singularities and soft gluon resummation, start at α_s^4 (NNLO). Hence this channel is suppressed with respect to $qq(gg) \to t\bar{t}$. The $\bar{q}g \to t\bar{t}\bar{q}$-channel is even more suppressed at the LHC due to its lower flux. Their contribution to the total cross section is at the percent level [42].

Electroweak corrections All corrections of the order $\alpha_s^2\alpha_g$ have been calculated in [43, 44, 45, 46], keeping the full dependence on the top quark spins. These contain the LO one-loop weak corrections to top pair production due to gluon fusion, quark annihilation and (anti-)quark-gluon scattering. Instead of a quark or a gluon, a W, Z, γ or Higgs boson is exchanged.
Contributions with a photon in the initial state are determined in [46], the most important one is $\gamma\, g \to t\bar{t}$. Another contribution derives from $b\bar{b} \to t\bar{t}$ via a t-channel W boson exchange or a s-channel annihilation into a Z boson or γ. In general, the electroweak contributions are smaller than the QCD uncertainty, yet they are important for certain distributions, especially in the high-energy regime (with a large $t\bar{t}$ invariant mass or high p_T), due to large Sudakov logarithms. With respect to the NLO cross section, the corrections are -1% for the weak, and 0.5% for the photonic contributions for the LHC [42].

2.4. Known Results at NNLO

Experimental experts claim, that they can measure the top quark pair production cross section $\sigma_{t\bar{t}}$ below 5% at the LHC [47]. The uncertainty will only be restricted by the error in the luminosity. As demonstrated in the last section, the error at NLO-level is about 15% and the resummation of soft gluons brings merely limited improvement. For accurate predictions of the top quark pair production cross section, a NNLO calculation is essential. Therefore four different parts are necessary (see Figure 2.9): The double real, the 1-loop 1-real, the 1-loop squared and the double virtual contributions. The calculation of the double virtual part $d\sigma^{VV}$ is described in detail in Chapter 4, whereas the computation of the other three parts, inclusive the phase space integration, is sketched in Chapter 3.

2.4.1. The High-Energy Limit at NNLO

The high-energy limits, i.e. $m_{top}^2 \ll s$, of the total cross sections $\hat{\sigma}_{q\bar{q}\to t\bar{t}}$ and $\hat{\sigma}_{gg\to t\bar{t}}$ have been calculated in [48, 49]. The amplitude has been partly determined with the same methods as will be introduced in Chapter 4.2 and partly using a relation between massless and massive QCD amplitudes. Comparing overlapping parts gives rise to highly non-trivial checks of both methods. Since the first method is explained in detail in Chapter 4, only the second will be sketched in the following:

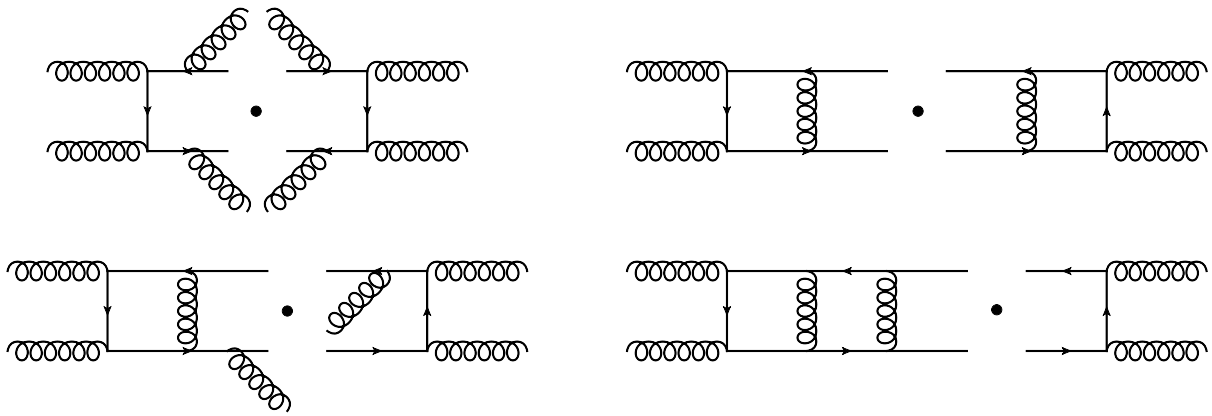

Figure 2.9.: The four different kinds of diagrams. The double real radiations $d\sigma^{RR}$, the 1-loop squared contribution $d\sigma^{SV}$, the 1-loop, 1-real part $d\sigma^{RV}$ and the double virtual contribution $d\sigma^{VV}$.

One-shell amplitudes for massless partonic processes can be factorized into the three functions $\mathcal{S}$, $\mathcal{J}$, $\mathcal{H}$ [50, 51, 52].

$$|\mathcal{M}\rangle^{(m=0)} = \mathcal{S}^{(m=0)} \otimes \mathcal{J}^{(m=0)} \otimes |\mathcal{H}\rangle\,, \tag{2.37}$$

These functions are called jet, soft and hard function and describe contributions to the amplitude emerging from the different momentum regions. The hard function $\mathcal{H}$ contains the short distance dynamics of the process and is finite after UV renormalization. The Jet function $\mathcal{J}$ only depends on the external partons and inherits all collinear contributions and the soft function $\mathcal{S}$ collects the soft contributions. Particularly, the soft and the jet functions are universal and do not depend on details of the hard scattering process.
In [52] a formula form massive external particles is derived, which is similar to Equation 2.37.

$$|\mathcal{M}\rangle^{(m)} = \mathcal{S}^{(m)} \otimes \mathcal{J}^{(m)} \otimes |\mathcal{H}\rangle\,, \tag{2.38}$$

Clearly, this affects the jet function $\mathcal{J}$, as it depends on the external particles. Since the gauge bosons in massive QCD stay massless, the infrared $\frac{1}{\varepsilon}$-poles coming from soft gluon radiation do not change. On the other hand, some of the collinear singularities are now screened by the top quark mass and they express themselves as logarithms of the mass. The form factor, which is connected to the jet function $\mathcal{J}$ by a simple relation, as well as the soft-function obey evolution equations. These equations resum the singular terms, i.e. $\frac{1}{\varepsilon}$-poles coming from soft gluons or large Sudakov-logarithms $\log(m)$ from collinear partons and lead to all-order exponentiation in terms of the corresponding anomalous dimension. This approach has been studied extensively in the literature e.g. [53, 54].

This transition from the massless to the massive amplitude in the small mass limit therefore can be seen as a change of the regularization scheme. The introduction of a small mass can be

thought of a way to regulate soft and collinear limits, instead doing dimensional regularization. The mass acts as a regulator and the massive amplitude must share crucial properties with the massless amplitude in the case $m \ll Q$ [52].

Equation 2.39 gives a direct relation between the massless and the massive amplitudes for physical processes.

$$\mathcal{M}^{(m)} \quad = \prod_{i \in \{\text{all legs}\}} \left(Z_{[i]}^{(m|0)}\right)^{\frac{1}{2}} \times \mathcal{M}^{(m=0)} \tag{2.39}$$

The process independent function Z is defined as the ratio of the massive and massless form factors and can be expanded in α_s. It can be seen as a kind of renormalization constant. Its result for different order in α_s is given in [52].

This limit cover only a tiny part of the phase space and unfortunately not all masters have been calculated in this limit. Therefore, they could not be plugged in the numeric differential equations (see Chapter 4.3) to obtain results for a much bigger phase space part. On the other hand, they serve as a verification of our final result.

2.4.2. Leading Color and Fermionic Results

Decomposing the next-to-next-to leading order result of the two loop virtual contributions into the color factors, gives the following result for the $q\bar{q}$-channel:

$$\begin{aligned}\mathcal{A}_{q\bar{q}}^{(0,2)} &= 2\mathrm{Re}\,\langle\mathcal{M}^{(0)}|\mathcal{M}^{(2)}\rangle = 2(N^2-1) \\ &\times\left(N^2A + B + \frac{1}{N^2}C + Nn_lD_l + Nn_hD_h + \frac{n_l}{N}E_l + \frac{n_h}{N}E_h + {n_l}^2F_l + n_ln_hF_{lh} + {n_h}^2F_h\right)\end{aligned} \tag{2.40}$$

N is the number of color, n_l and n_h denote the number of light or heavy fermions, respectively. The leading color term A and the fermionic contributions $D_l, D_h, E_l, E_h, F_l, F_h, F_{lh}$ were calculated fully analytically in [55] and [56]. The former one contains only planar graphs, the latter ones get contributions only from graphs which contain a closed light l and/or heavy h fermion loop. The results were obtained by using the method of differential equations and can be expressed in terms of one- and two-dimensional harmonic polylogarithms. The analytic result is evaluated numerically with C++, using GiNaC [57] for the calculation of the multiple polylogarithms.
In the gg-channel, the result for the interference of the two loop graphs with the born amplitude can be decomposed into the color factors:

$$\begin{aligned}\mathcal{A}_{gg}^{(0,2)} &= 2\mathrm{Re}\,\langle\mathcal{M}^{(0)}|\mathcal{M}^{(2)}\rangle = (N^2-1)\Bigg(N^3A + NB + \frac{1}{N}C + \frac{1}{N^3}D + N^2n_lE_l + N^2n_hE_h \\ &+n_lF_l + n_hF_h + \frac{n_l}{N^2}G_l + \frac{n_h}{N^2}G_h + N{n_l}^2H_l + Nn_ln_h\,H_{lh} + N{n_h}^2H_h + \frac{{n_l}^2}{N}I_l + \frac{n_ln_h}{N}I_{lh} + \frac{{n_h}^2}{N}I_h\Bigg)\end{aligned} \tag{2.41}$$

The leading color result of the double virtual corrections in the gg-channel A was calculated in in [58]. As in the $q\bar{q}$-channel, only planer graphs contribute. Moreover, no additional master integrals had to be calculated. The results were obtained by using the Laporta Algorithm [59] for the reduction to the master integrals. Afterwards the master integrals were determined using the method of differential equations. The analytic result of the master integrals can be written in terms of one- and two-dimensional harmonic polylogarithms and evaluated numerically by using the computer algebra system GiNaC [57].

The remaining pieces, in the quark-antiquark channel B and C and in the gluon fusion channel B, C, D, E_h, F_h and G_h, contain either non-planar topologies, or complicated massive subtopologies.
In the first case, the analytic evaluation of the master integrals (using the method of differential equations) is challenging, because of the large number of coupled master integrals for certain topologies. In the second case, it is already known from the sunrise diagram with three massive virtual and two massive external propagators that it can be expressed analytically only with the help of elliptic integrals [60]. Similar graphs appear in the color coefficient with the subscript h.

2.4.3. Pole Structure of $\sigma_{t\bar{t}}$

In the last years a lot of progress was done in understanding the IR-structure[3] of QCD scattering amplitudes. This IR-structure is generated by the collinear and soft limits of the amplitude. The cancellation of these divergences for any observable is granted by the factorization proofs [61, 62, 63]. Nevertheless, each of the four parts of the $\hat{\sigma}_{t\bar{t}}$ calculation (see Figure 2.9) contains IR-singularities. In [64] the complete IR-singularities of $d\sigma_{t\bar{t}}^{VV}$ was predicted only from general QCD properties, like the anomalous dimension Γ. This matrix only depends on the masses and the momenta of the external partons.

It is a well-known fact [65] that the partonic cross section can be divided into three parts, schematically written as

$$\hat{\sigma} = \mathcal{H} \otimes \mathcal{J} \otimes \mathcal{S} \,, \tag{2.42}$$

whereby $\mathcal{H}$ is the hard, $\mathcal{J}$ is the jet and,$\mathcal{S}$ is the soft function. The first contains all information about the nature of the heavy particles and the physical model. It is obtained from the threshold expansion of the amplitude and it is finite as $\epsilon \to 0$. $\mathcal{J}$ is called 'jet function' and contains the multiple exchange of coulomb gluons. They can be resumed by using methods from non-relativistic QCD and contain terms of the form (α_s/β). Finally, $\mathcal{S}$ is the soft function and describes the radiation of soft gluons. The resummation of the threshold logarithms $\log \beta$ is performed by solving the evolution equations for $\mathcal{S}$.

Let $|\mathcal{M}(\epsilon, \underline{p}, \underline{m})\rangle$ be an UV renormalized, n-parton on-shell scattering amplitude, where the IR-singularities are regularized in $d = 4 - 2\epsilon$ dimensions. It was proven in [66, 67, 29] that the IR divergences can be extracted from the amplitude using a multiplicative renormalization factor

[3] IR stands for infrared

$Z^{-1}(\epsilon, p, m, \mu)$.

$$Z^{-1}(\epsilon, p, m, \mu)\,|\mathcal{M}(\epsilon, p, m)\rangle = \text{finite}\ , \tag{2.43}$$

where $|\mathcal{M}(\epsilon, p, m)\rangle$ is the finite hard function $\mathcal{H}$, which can be expanded in a perturbative series in α_s

$$|\mathcal{M}\rangle = 4\pi\alpha_s \left[|\mathcal{M}^{(0)}\rangle + \frac{\alpha_s}{4\pi}\,|\mathcal{M}^{(1)}\rangle + \left(\frac{\alpha_s}{4\pi}\right)^2 |\mathcal{M}^{(2)}\rangle + \dots\right]. \tag{2.44}$$

and the factor $Z^{-1}(\epsilon, p, m, \mu)$, which contains all the singularities, is determined through the soft and jet functions $\mathcal{J}$ and $\mathcal{S}$. This can be expanded perturbatively as well, resulting in:

$$Z = 1 + \sum_{k=1}^{\infty} \left(\frac{\alpha_s(\mu)}{\pi}\right)^k \sum_{n=1}^{k} \left(\frac{1}{\epsilon}\right)^n Z^{(k)} \tag{2.45}$$

Expanding Equation 2.43 up to order two gives the singular terms

$$\begin{aligned}
|\mathcal{M}^{(0),\,\text{sing}}\rangle &= 0\,,\\
|\mathcal{M}^{(1),\,\text{sing}}\rangle &= Z^{(1)}\,|\mathcal{M}^{(0)}\rangle\,,\\
|\mathcal{M}^{(2),\,\text{sing}}\rangle &= \left[Z^{(2)} - \left(Z^{(1)}\right)^2\right]|\mathcal{M}^{(0)}\rangle + \left(Z^{(1)}\,|\mathcal{M}^{(1)}\rangle\right)_{\text{poles}}.
\end{aligned} \tag{2.46}$$

Note that in order to predict the IR poles at two-loop order, one needs the UV-renormalized one-loop amplitudes to $\mathcal{O}(\epsilon)$, since these terms contribute to the $1/\epsilon$ pole after cancelling with the $1/\epsilon^2$ pole of the one-loop Z-factor. The structure of Z is constraint by the renormalization group equation:

$$Z^{-1}(\epsilon, p, m, \mu)\,\frac{d}{d\ln\mu}\,Z(\epsilon, p, m, \mu) = -\Gamma(p, m, \mu) \tag{2.47}$$

The renormalization factor is connected with the universal anomalous dimension matrix $\Gamma(p, m, \mu)$. This matrix contains the scale behavior of the effective theory and has been calculated for massless particles at two-loop order in [68, 69]. Explicit results for heavy quark productions were calculated in [64].

$$\begin{aligned}
\mathbf{\Gamma}_{q\bar{q}} = &\left[C_F\,\gamma_{\text{cusp}}(\alpha_s)\,\ln\frac{-s}{\mu^2} + C_F\,\gamma_{\text{cusp}}(\beta_{34}, \alpha_s) + 2\gamma^q(\alpha_s) + 2\gamma^Q(\alpha_s)\right]\mathbf{1}\\
&+ \frac{N}{2}\left[\gamma_{\text{cusp}}(\alpha_s)\,\ln\frac{(-s_{13})(-s_{24})}{(-s)\,m_t^2} - \gamma_{\text{cusp}}(\beta_{34}, \alpha_s)\right]\begin{pmatrix}0 & 0\\ 0 & 1\end{pmatrix}\\
&+ \gamma_{\text{cusp}}(\alpha_s)\,\ln\frac{(-s_{13})(-s_{24})}{(-s_{14})(-s_{23})}\left[\begin{pmatrix}0 & \frac{C_F}{2N}\\ 1 & -\frac{1}{N}\end{pmatrix} + \frac{\alpha_s}{4\pi}\,g(\beta_{34})\begin{pmatrix}0 & \frac{C_F}{2}\\ -N & 0\end{pmatrix}\right] + \mathcal{O}(\alpha_s^3)\,,
\end{aligned} \tag{2.48}$$

where $s \equiv s_{12}$ is the square of the partonic center-of-mass energy.

$$\begin{aligned}\mathbf{\Gamma}_{gg} &= \left[N\,\gamma_{\text{cusp}}(\alpha_s)\,\ln\frac{-s}{\mu^2} + C_F\,\gamma_{\text{cusp}}(\beta_{34},\alpha_s) + 2\gamma^g(\alpha_s) + 2\gamma^Q(\alpha_s)\right]\mathbf{1} \\ &\quad + \frac{N}{2}\left[\gamma_{\text{cusp}}(\alpha_s)\,\ln\frac{(-s_{13})(-s_{24})}{(-s)\,m_t^2} - \gamma_{\text{cusp}}(\beta_{34},\alpha_s)\right]\begin{pmatrix}0&0&0\\0&1&0\\0&0&1\end{pmatrix} \\ &\quad + \gamma_{\text{cusp}}(\alpha_s)\,\ln\frac{(-s_{13})(-s_{24})}{(-s_{14})(-s_{23})}\left[\begin{pmatrix}0&\frac{1}{2}&0\\1&-\frac{N}{4}&\frac{N^2-4}{4N}\\0&\frac{N}{4}&-\frac{N}{4}\end{pmatrix} + \frac{\alpha_s}{4\pi}\,g(\beta_{34})\begin{pmatrix}0&\frac{N}{2}&0\\-N&0&0\\0&0&0\end{pmatrix}\right] + \mathcal{O}(\alpha_s^3)\,.\end{aligned} \tag{2.49}$$

This result was used to predict the IR-structure of the double virtual amplitudes $d\sigma^{VV}_{q\bar{q}\to t\bar{t}}$ and $d\sigma^{VV}_{gg\to t\bar{t}}$ and is shown in Table 4.2. It is used to validate our result for the double virtual contribution.

2.4.4. Uncertainty from Scale Variation at NNLO

The following section shows how the scale dependent logarithms at NNLO-level are calculated easily, when knowing the full NLO result. Therefore the scale dependence of the NNLO cross section can be estimated. The full NLO order result and the renormalization group equations have to be used. The ansatz uses the fact that the total cross section $\sigma_{t\bar{t}}$ does not depend on the scale $\mu = \mu_F = \mu_R$ at any given order.

$$\mu^2\frac{d}{d\mu^2}\sigma_{t\bar{t}} = 0 \tag{2.50}$$

After the insertion of Equation 2.1, and knowing the derivative of the PDFs after μ from the DGLAP evolution equations,

$$\mu^2\frac{d}{d\mu^2}f_{i,A}(x,\mu) = \frac{\alpha_s(\mu)}{\pi}[P_{ij}\otimes f_{j,A}(z,\mu)](x), \tag{2.51}$$

whereat P_{ij} are the splitting functions and $\otimes$ is a convolution [4] the following equation is obtained.

$$\sum_{ijk} f_{i,A}\otimes\left[\frac{\alpha_s(\mu)}{\pi}P_{ik}\otimes\frac{\sigma_{kj}(z,\mu)}{z} + \mu^2\frac{d}{d\mu^2}\frac{\sigma_{kj}(z,\mu)}{z} + \frac{\alpha_s(\mu)}{\pi}\frac{\sigma_{ik}(z,\mu)}{z}\otimes P_{kj}\right]\otimes f_{j,B} = 0 \tag{2.52}$$

As the equation is valid for arbitrary μ and z, the expression in the brackets must be zero. Thus:

$$\mu^2\frac{d}{d\mu^2}\frac{\sigma_{kj}(z,\mu)}{z} = -\frac{\alpha_s(\mu)}{\pi}\left[P_{ik}\otimes\frac{\sigma_{kj}(z,\mu)}{z} + \frac{\sigma_{ik}(z,\mu)}{z}\otimes P_{kj}\right] \tag{2.53}$$

For $\sigma_{kj}(z,\mu)$ the following ansatz

[4] $[P_{ij}\otimes f_{j,A}](x) := \int_0^1\int_0^1 dx_1dx_2P_{ij}(x_1)f_{j,A}(x_2)\delta(x_1x_2-x)$

$$\hat{\sigma}_{ij}(\mu) = \frac{\alpha_s(\mu)}{\pi}\hat{\sigma}^{LO}(\mu) + \left(\frac{\alpha_s(\mu)}{\pi}\right)^2 \hat{\sigma}^{NLO}(\mu) + \left(\frac{\alpha_s(\mu)}{\pi}\right)^3 \hat{\sigma}^{NNLO}(\mu) + ... \tag{2.54}$$

is plugged in Equation 2.53 and solved order for order in α_s. Only the integration constants stay unknown.
Nevertheless, the equation and a known n-th order result can be used to derive the μ dependence of the result of one order higher $(n+1)$. This term can be divided by $\sigma_{ij}^n(\mu)$, which is a good approximation to $\sigma_{ij}^{n+1}(\mu)$, to obtain the scale uncertainty on $n+1$ level. The calculation was done for the top quark pair production with the splitting functions from [21, 70] and the NLO result from [24]. The scale dependence on NNLO level is between 3% and 4% percent, if the scale is varied between $\frac{1}{2}m_{top}$ and $2m_{top}$.

3. The total cross section of the Quark Anti-Quark Annihilation Channel

The importance of the calculation of the top quark pair cross section $\sigma_{t\bar{t}}$ and the domination of the quark annihilation channel $\sigma_{q\bar{q}\to t\bar{t}}$ at the Tevatron with a rate of 90% has been the subject of Chapter 1 and 2. In this chapter the computation of the NNLO top quark pair production cross section $\sigma_{q\bar{q}\to t\bar{t}}$ is explained. For the calculation, four different classes of diagrams have to be calculated (see Figure 3.1). The author was involved in the calculation of the double virtual corrections only, which is described in detail in Chapter 4, nevertheless the calculatation of the other tree parts is sketched in this chapter.
Whereas the 1-loop squared and the double virtual contributions possess highly non-trivial matrix elements, the bottleneck of the 1-loop 1-real and the double real contributions is the phase space integration. Soft and collinear partons generate infrared divergences by the integration over the phase space.
The Kinoshita-Lee-Nauenberg theorem [61, 62] states that observables, like cross sections, calculated within the Standard Model are infrared safe. This implies that IR singularities, coming from real radiation, cancel with IR divergences from loop integrals (UV singularities are absorbed by the renormalization procedure). Inital state divergencies are absorbed into the PDFs. Therefore, the sum of all four different parts is finite, but the individual parts are not. In the case, where one of the emitted partons is soft or collinear, naive numeric integration fails due to phase space singularities. The subtraction method describes a way to solve this puzzle. It assumes that subtraction terms $d\sigma^{S_{RR}}$ and $d\sigma^{S_{RV}}$ can be constructed (see Equation 3.1), which on the one hand mimic the singular structure of the double real or the 1-loop 1-real contributions respectively, and on the other hand can be integrated analytically.

$$\begin{aligned}\sigma_{q\bar{q}\to t\bar{t}} = &\int_{d\Phi_4} \left(d\sigma^{RR} - d\sigma^{S_{RR}}\right) + \int_{d\Phi_3} \left(d\sigma^{RV} - d\sigma^{S_{RV}}\right) \\ &+ \int_{d\Phi_2} \left(d\sigma^{VV} + d\sigma^{SV}\right) + \int_{d\Phi_4} d\sigma^{S_{RR}} + \int_{d\Phi_3} d\sigma^{S_{RV}} \end{aligned} \tag{3.1}$$

Afterwards the phase space integration of the real contributions can be performed numerically, because all singularities vanish, and the analytically integrated subtraction terms cancel exactly the IR divergences from the double virtual and the one-loop squared contributions. In the following, the calculation of all four parts is described briefly. In the case of the virtual contributions the difficulties lie in the evaluation of the matrix elements, in the case of the real contributions in the construction of the subtraction terms.

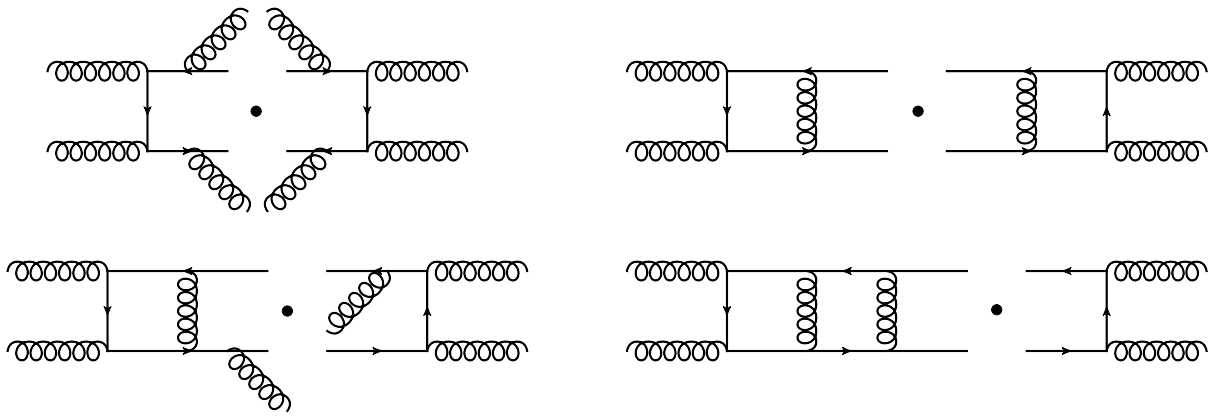

Figure 3.1.: The four different kinds of diagrams. The double real radiations $d\sigma^{RR}$, the 1-loop squared contribution $d\sigma^{SV}$, the 1-loop, 1-real part $d\sigma^{RV}$ and the double virtual contribution $d\sigma^{VV}$.

3.1. Evaluation of the Double Real Contributions

While the calculation of matrix element of the double real contributions is almost trivial, its integration over the phase space is complicated. This is due to the fact, that the two emitted partons (g, q, $\overline{q}$) can be soft and/or collinear, which generate singularities during the phase space integration. These IR-divergences cancel exactly the IR singularities coming from the virtual contributions.
At NLO-level various elaborated approaches are available. The most frequently used are the ones from Catani-Seymour [71], Nagy-Soper [72] and Frixione-Kunszt-Signer [73]. The first one uses a smooth interpolation of the subtraction terms between the different singular limits and a factorization formula permits the remapping of the phase space onto one with one parton less. The second is a good choice for parton shower algorithms. Finally, in the FSK-sheme the phase space is first decomposed into different sectors and afterwards a certain parametrisation is used to extract the subtraction terms [74, 75].

Different methods at NNLO-level have been proposed. Amongst others, Antenna subtraction [76] and sector decomposition [77], but none of them leads to a simple and general algorithm. The double real contributions were calculated with the new introduced `Stripper` approach, which is described in [74, 75] and we will follow these papers to explain the computation of the double real contribution.

First, the phase space is factorized into a three-particle production phase space of two massless particles and a particle with invariant mass Q^2.

$$\begin{aligned}\int d\Phi_{n+2} &= \int \frac{d^{d-1}k_1}{(2\pi)^{d-1}2k_1^0}\frac{d^{d-1}k_2}{(2\pi)^{d-1}2k_2^0} \\ &\times \int\prod_{i=1}^{n}\frac{d^{d-1}q_i}{(2\pi)^{d-1}2q_i^0}(2\pi)^d\delta^{(d)}(q_1+\cdots+q_n-Q) \\ &\equiv \int d\Phi_3\int d\Phi_n(Q)\;, \end{aligned} \tag{3.2}$$

where k_i are the massless and q_i are the massive partons. The motivation for this factorization is the fact that most of the divergencies originate from the vanishing of invariants, which involve only massless partons. In a second step, the pase space is decomposed taking into account only the collinear divergencies. These arise if $k_i||p_j$ or $k_1||k_2$. The result is a decomposition of the phase space into a triple-collinear, a double-collinear and a single-collinear sector:

$$\begin{aligned}1 = & \\ & \left.\begin{array}{l}+\theta_1(k_1)\theta_1(k_2)\\ +\theta_2(k_1)\theta_2(k_2)\end{array}\right\}\text{triple-collinear sector} \\ & \left.\begin{array}{l}+\theta_1(k_1)\theta_2(k_2)(1-\theta_3(k_1,k_2))\\ +\theta_2(k_1)\theta_1(k_2)(1-\theta_3(k_1,k_2))\end{array}\right\}\text{double-collinear sector} \\ & \left.+(\theta_1(k_1)\theta_2(k_2)+\theta_2(k_1)\theta_1(k_2))\theta_3(k_1,k_2)\;\right\}\text{single-collinear sector}\;, \end{aligned} \tag{3.3}$$

whereby $\theta_i(k)$ is defined in such a way, that $\theta_i(k)=1$ if $k||p_i$ and $\theta_i(k)=0$ if $k||p_j$ with $j\neq i$. Moreover the sum of the two functions has to be 1: $\theta_1(k)+\theta_2(k)=1$. A third function $\theta_3(k_1,k_2)$ seperates divergencies coming from $k_1||k_2$ and is 1 in this limit. The different sectors can be treated independently. With the parametrization used in [74] for the triple-collinear sector, the pase space $d\Phi_3$ can be written as

$$\begin{aligned}\int d\Phi_3 &= \frac{\pi^{2\epsilon}}{8(2\pi)^5\Gamma(1-2\epsilon)}s^{2-2\epsilon}\beta^{8-8\epsilon}\int_0^1 d\zeta\;(\zeta(1-\zeta))^{-\frac{1}{2}-\epsilon} \\ &\times \iint_0^1 d\eta_1 d\eta_2\;(\eta_1(1-\eta_1))^{-\epsilon}(\eta_2(1-\eta_2))^{-\epsilon}\frac{\eta_3^{1-2\epsilon}}{|\eta_1-\eta_2|^{1-2\epsilon}} \\ &\iint d\xi_1 d\xi_2\;\xi_1^{1-2\epsilon}\xi_2^{1-2\epsilon}\;, \end{aligned} \tag{3.4}$$

where η_i and ξ_i are defined by Formula 3.5:

$$\begin{aligned}-(p_1-k_1)^2 &= s\beta^2\xi_1\eta_1\;, \\ -(p_1-k_2)^2 &= s\beta^2\xi_2\eta_2\;, \\ (k_1+k_2)^2 &= s\beta^4\xi_1\xi_2\eta_3\;, \\ -(p_1-k_1-k_2)^2 &= s\beta^2(\xi_1\eta_1+\xi_2\eta_2-\beta^2\xi_1\xi_2\eta_3)\;, \end{aligned} \tag{3.5}$$

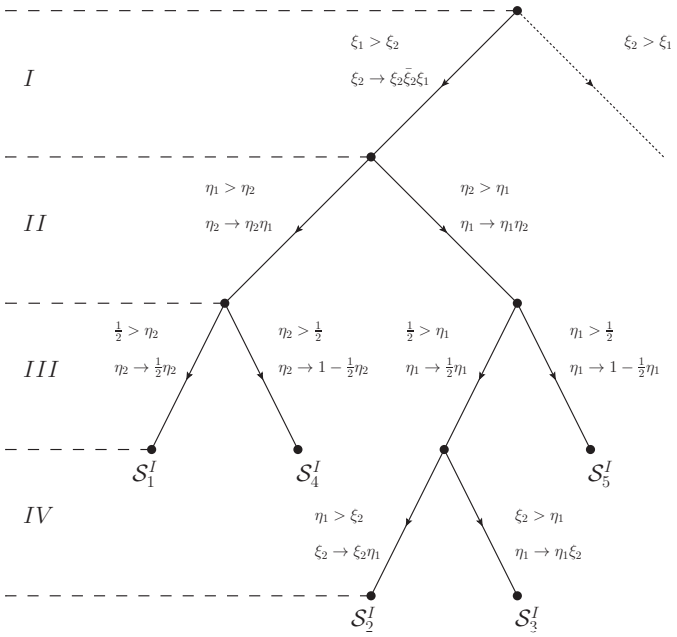

Figure 3.2.: Sector decomposition of the triple collinear phase space sector. It is shown how the soft-, collinear-, and soft-collinear divergencies are factorized. Plot taken from [74].

A further decomposition of the phase space can be achieved by exploiting the invariants introduced in Formula 3.5 and represented graphically in Figure 3.2 and Figure 3.3 for the triple and double collinear sector respectively. The result is a decomposition into 5 different sectors $\mathcal{S}_1 ... \mathcal{S}_5$. The physical interpretation of these decomposition is the factorization of soft divergencies (I), the factorization of the collinear divergencies (II) and the factorization of the soft-collinear divergencies (III) [74].

All different sectors can be computed independently, whereby Figure 3.2 and Figure 3.3 give an ordering of the relevant variables. The final result is the sum off all different sectors.

3.2. Calculation of the 1-Loop Square Contribution

The $d\sigma_{q\bar{q}}^{SV}$ and $d\sigma_{gg}^{SV}$ parts, that means the one-loop squared contributions, were calculated in [78, 79, 80, 81] fully analytically. These one-loop diagrams contain $1/\epsilon^2$ terms due to ultraviolet and infrared singularities. Therefore, to obtain the correct squared amplitude up to the order ϵ^0, the master integrals have to be known up to order ϵ^2. The imaginary part is also important, since the amplitude gets squared. The result for the master integrals are given in [78] in terms of so-called L-funtions and in [82] in terms of multiple polylogarithms. One scalar one-point function, five scalar two-point, six scalar three-point and three scalar four-point functions (given

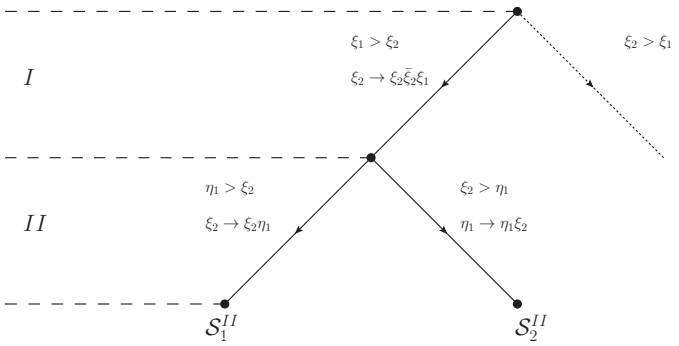

Figure 3.3.: Sector decomposition of the double collinear phase space sector. Plot taken from [74].

	Nomenclature of [[25]]	Comments
1-point	$A(m)$	Re
2-point	$B(p_4 - p_2, 0, m)$	Re
	$B(p_3 + p_4, m, m)$	Re, Im
	$B(p_4, 0, m)$	Re
	$B(p_2, m, m)$	Re
	$B(p_3 + p_4, 0, 0)$	Re, Im
3-point	$C(p_4, p_3, 0, m, 0)$	Re, Im
	$C(p_4, -p_2, 0, m, m)$	Re
	$C(-p_2, p_4, 0, 0, m)$	Re
	$C(-p_2, -p_1, 0, 0, 0)$	Re, Im
	$C(-p_2, -p_1, m, m, m)$	Re, Im
	$C(p_3, p_4, m, 0, m)$	Re, Im
4-point	$D(p_4, -p_2, -p_1, 0, m, m, m)$	Re, Im
	$D(-p_2, p_4, p_3, 0, 0, m, 0)$	Re, Im
	$D(-p_2, p_4, -p_1, 0, 0, m, m)$	Re

Table 3.1.: List of one-, two-, three- and four-point massive one-loop functions calculated in [78] up to $\mathcal{O}(\epsilon^2)$ in order to obtain the one-loop squared contribution.

in Table 3.1) had to be calculated. They are defined by:

$$A(m) = \mu^{2\epsilon} \int \frac{d^n q}{(2\pi)^n} \frac{1}{q^2 - m^2} \tag{3.6}$$

$$B(q_1, m_1, m_2) = \mu^{2\epsilon} \int \frac{d^n q}{(2\pi)^n} \frac{1}{(q^2 - m_1^2)[(q+q_1)^2 - m_2^2]}$$

$$C(q_1, q_2, m_1, m_2, m_3) = \mu^{2\epsilon} \int \frac{d^n q}{(2\pi)^n} \frac{1}{(q^2 - m_1^2)[(q+q_1)^2 - m_2^2][(q+q_1+q_2)^2 - m_3^2]}$$

$$D(q_1, q_2, q_3, m_1, m_2, m_3, m_4) =$$
$$\mu^{2\epsilon} \int \frac{d^n q}{(2\pi)^n} \frac{1}{(q^2 - m_1^2)[(q+q_1)^2 - m_2^2][(q+q_1+q_2)^2 - m_3^2][(q+q_1+q_2+q_3)^2 - m_4^2]}$$

The calculation was done analytically in dimensional regularization with the help of a Feynman parametrization. The result of the master integrals can be plugged in the squared amplitude. Needless to say that the accompanying Passarino-Feldman reduction and the spin algebra has to be performed up to order ϵ^2 as well. The most complex expressions arise from box contributions. There, multiple polylogarithms up to weight four are generated.

In a numerical computation of heavy flavor production, all four pieces have to be evaluated at many values of the kinematic variables. This requires efficient numerical code. The result in the $q\bar{q}$-annihilation channel [80] was given in one compact file, in contrast, in the gg-channel a lot of work had to be invested to combine the given partial result in the correct way. This was done in a C++ program to make fast computation possible. However, an evaluation of the appearing multiple polylogarithms with GiNaC turned out to be very slow (about 10 seconds for multiple polylogarithms of weight four), what makes a numeric computation impossible. On the other hand, the evaluation of the L-functions [82] with a Fortran routine was a factor of 1000 faster (10 milliseconds instead of 10 seconds).

3.3. Determination of the 1-Loop, 1-Real-Radiation Part

The third class of diagrams (see Figure 3.1) is the interference of the tree-level graph and the one-loop graph, where both graphs emit an additional soft gluon. There are three tasks to perform. First, the calculation of the amplitude $\langle M^{(0)}(n+1)|M^{(1)}(n+1)\rangle$, second the determination of the subtraction terms, i.e. the calculation of $\langle M^{(0)}(n+1;q)|M^{(1)}(n+1;q)\rangle$ in the limit where the additional gluon q becomes soft and third, the phase space integration. Thereby, the soft limit imitates the complete infrared structure and therefore provides the subtraction term for the phase space integration. For massless particles the soft limit was known before [83, 84, 85, 86, 87].

Evaluation of the Amplitude

The amplitude $\langle \mathcal{M}^{(0)}(n+1)|\mathcal{M}^{(1)}(n+1)\rangle$ is computed using the same methods as presented in Chapter 4. It contains 60 master integrals. Due to the 5 independent variables (4 Mandelstamm

variables and ϵ, instead of 3 independent variables in the $2 \to 2$ case) the reduction of the amplitude is enormous.

Calculation of the Subtraction Term

In order to integrate the 1-loop 1-real amplitude $\langle \mathcal{M}^{(0)}(n+1)|\mathcal{M}^{(1)}(n+1)\rangle$ the subtraction terms, which contains the complete singularities, are needed for the phase space integration to be finite. Due to the massive top quarks, there are no singularities coming from the collinear limit and therefore the only divergent ingredient is the limit, where the emitted gluon becomes soft.
The $n+1$ final particle state amplitude $\mathcal{M}(n+1;q)$ with the soft gluon q can be expanded in α_s:

$$\mathcal{M}(n+1;q) = \mathcal{M}^{(0)}(n+1;q) + \mathcal{M}^{(1)}(n+1;q) + ... \tag{3.7}$$

In the limit, where the emitted gluon becomes soft (i.e. $\lambda \to 0$, if the gluon momentum q scales as $q \to \lambda q$), the scattering amplitude satisfies the following factorization property [87]:

$$|\mathcal{M}(n+1;q)\rangle = J(q)|\mathcal{M}(n)\rangle \ , \tag{3.8}$$

where $|\mathcal{M}(n)\rangle$ is obtained from $|\mathcal{M}(n+1;q)\rangle$ by removing the soft gluon. Its complete dependence on the soft gluon is factorized into the soft current $J(q) \equiv \epsilon^\mu J_\mu(q)$. Power suppressed terms are neglected. $\mathcal{M}(n)$ has a similar expansion in the strong coupling constant like $\mathcal{M}(n+1;q)$ in Equation 3.7 and the soft current J can be expanded as:

$$J(q) = g_s \mu^\varepsilon (J^{(0)}(q) + J^{(1)}(q) + ...) \ , \tag{3.9}$$

where higher powers implicate a higher order in α_s and the color dependence is here and in the following suppressed. Therefore, the matrix element can be written as

$$\begin{aligned} \langle \mathcal{M}^{(0)}(n+1;q)|\mathcal{M}^{(1)}(n+1;q)\rangle = {} & g_s^2 \mu^{2\varepsilon} \langle \mathcal{M}^{(0)}(n)|J^{(0)}(q)J^{(0)}(q)|\mathcal{M}^{(1)}(n)\rangle \\ & + g_s^2 \mu^{2\varepsilon} \langle \mathcal{M}^{(0)}(n)|J^{(0)}(q)J^{(1)}(q)|\mathcal{M}^{(0)}(n)\rangle \end{aligned} \tag{3.10}$$

and the challenge is the evaluation of the soft currents $J^{(0)}(q)$, $J^{(1)}(q)$, what will be described below.
The tree-level current can be written with the help of the color charge T_i of the i-th parton as

$$J^{\mu(0)}(q) = \sum_{i=1}^{m} T_i \, \frac{p_i^\mu}{p_i \cdot q} \tag{3.11}$$

The soft one-loop gluon current was calculated in [87] for massless particles:

$$\begin{aligned} \mathbf{J}_a^{\mu\,(1)}(q,\epsilon) = {} & -\frac{1}{16\pi^2} \, \frac{1}{\epsilon^2} \, \frac{\Gamma^3(1-\epsilon)\,\Gamma^2(1+\epsilon)}{\Gamma(1-2\epsilon)} \\ & \cdot \ i \, f_{abc} \sum_{i \neq j} T_i^b \, T_j^c \left(\frac{p_i^\mu}{p_i \cdot q} - \frac{p_j^\mu}{p_j \cdot q} \right) \left[\frac{4\pi \, p_i \cdot p_j \, e^{-i\lambda_{ij}\pi}}{2(p_i \cdot q)\,(p_j \cdot q)\, e^{-i\lambda_{iq}\pi}\, e^{-i\lambda_{jq}\pi}} \right]^\epsilon \end{aligned} \tag{3.12}$$

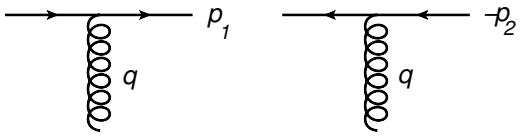

Figure 3.4.: A gluon couples on a fermion line. These two graph are used for the calculation of the soft current $J^{\mu(0)}(q)$.

Thereby $e^{-i\lambda_{ij}\pi}$ is $+1$ if both particle are incoming or outgoing and 0 otherwise. As it can be seen in Equation 3.12, the soft current does not depend on the color flows and the momenta of the internal particles. It only contains informations about the soft gluon and the external particles. Therefore the currents are process independent and universal. They contain the complete description of the soft gluon and control the the singular behavior of one loop massive QCD amplitudes in the limit when one external gluon becomes soft. The result of the massive case can be found in [88].

Calculation of $J^{(0)}$ Figure 3.4 represents two gluons which couple to a fermion line. Employing the Feynman rules, the first one (and the second one similar) can be expressed as:

$$\overline{u}\, i\, \gamma^{\mu}\, T^{a}\, i\, \frac{\not{p}_1 - \not{k} + m}{(p_1 - k)^2 - m^2} \tag{3.13}$$

After performing the Dirac algebra and using the equations of motion the result is:

$$\overline{u}\, T^{a}\, \frac{2p^{\mu} - k^{\mu}}{2\, p_1\, k - k^2} \tag{3.14}$$

In the limit of $k \to 0$ its contribution is:

$$\overline{u}\, T^{a}\, \frac{p^{\mu}}{p_1\, k} \tag{3.15}$$

and a similar expression for the left diagram in Figure 3.4. Equation 3.11 is therefore justified.

Derivation of $J^{(1)}$ In principle, all 1-loop 1-real diagrams have to be calculated. [87] describes a way, which simplifies the calculation considerably. There are two different types of one-loop diagrams, which are represented in Figure 3.5. The blob denotes the tree-level amplitude. The virtual gluon k can either connect two different particles (left) or can couple two times on the same parton (right). The additionally emitted gluon q can be inserted in all possible ways.
The amplitude $\mathcal{M}^{(1)}$ can be split, depending on the kinematic region of the momentum k.

$$|\mathcal{M}^{(1)}\rangle = |\mathcal{M}^{(1)}_{hard}\rangle + |\mathcal{M}^{(1)}_{coll}\rangle + |\mathcal{M}^{(1)}_{soft}\rangle \ , \tag{3.16}$$

If the gluon k is hard, the soft gluon decouples decouples:

$$|\, \mathcal{M}^{(1)}_{hard}(q, p_i)\rangle \simeq g_S \mu^{\epsilon} \varepsilon^{\mu}(q) J^{(0)}_{\mu}(q)\, |\, \mathcal{M}^{(1)}_{hard}(p_i)\rangle\, , \tag{3.17}$$

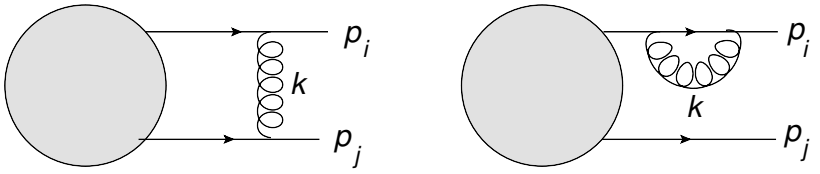

Figure 3.5.: The two types of Feynman diagrams. Left: The gluon couples on two different external lines. Right: The gluon couples only on one external momentum. Figure taken from [87].

where $J_\mu^{a\,(0)}(q)$ is the soft-gluon current given in Equation 3.9.
In the case that the momentum k is collinear to the momentum of one of the external legs, the amplitude factorizes:

$$|\,\mathcal{M}^{(1)}_{coll}(q,p_i)\rangle \simeq g_S \mu^\epsilon \varepsilon^\mu(q) J^{(0)}_\mu(q)\;|\,\mathcal{M}^{(1)}_{coll}(p_i)\rangle\,. \tag{3.18}$$

If the gluon k is soft, the amplitude does not completely factorize, but it can be written as:

$$\begin{aligned}|\mathcal{M}^{(1)}_{soft}(q,p_i)\rangle &= g_S\,\mu^\epsilon\,\varepsilon^\mu(q)\,J^{(0)}_\mu(q)\,|\mathcal{M}^{(1)}_{soft}(p_i)\rangle \\ &\quad + (\,(\,|\mathcal{M}^{(1)}_{soft}(q,p_i)\rangle - g_S\mu^\epsilon\varepsilon^\mu(q)J^{(0)}_\mu(q)|\mathcal{M}^{(1)}_{soft}(p_i)\rangle\,)\;\;, \end{aligned}\tag{3.19}$$

where we have added and subtracted the 'factorized' contribution. Combining the contributions from the hard, collinear and soft regions by adding the Equations 3.17, 3.18 and 3.19, we obtain

$$\begin{aligned}|\mathcal{M}^{(1)}(q,p_i)\rangle &= g_S\,\mu^\epsilon\,\varepsilon^\mu(q)\,\boldsymbol{J}^{(0)}_\mu(q)\,|\mathcal{M}^{(1)}(p_i)\rangle \\ &\quad + \Big(\,|\mathcal{M}^{(1)}_{soft}(q,p_i)\rangle - g_S\mu^\epsilon\varepsilon^\mu(q)\boldsymbol{J}^{(0)}_\mu(q)|\mathcal{M}^{(1)}_{soft}(p_i)\rangle\Big)\;\;. \end{aligned}\tag{3.20}$$

The challenge is to evaluate the second bracket of Equation 3.20, which simultaneously supplies the definition of $J^{(1)}_\mu(q)|\mathcal{M}^{(0)}(p_i)\rangle$. It states, that $|\mathcal{M}^{(1)}(q,p_i)\rangle$ can be split into a factorisable term, which is proportional to $J^{(0)}_\mu(q)$ and the non-factorisable term $J^{(1)}_\mu(q)$. The diagrams, which have to be evaluated are pictured in Figure 3.6 and 3.7. The calculation is performed in the eikonal approximation, i.e. energy and momentum conservation is enforced and soft and collinear gluons are treated as being of the similar magnitude. Exploiting the color structure of the diagrams, gauge symmetry and current conservation simplifies the calculation of $J^{(1)}_\mu(q)$.
The result of the massless current $J^{(1)}_\mu(q)$ is given in Equation 3.12. The result for massive external particles can be found in [88], where two independent analytic and a numeric calculation have been performed. The resulting term for $\langle\mathcal{M}^{(0)}(n+1;q)|\mathcal{M}^{(1)}(n+1;q)\rangle$ from Equation 3.10 and its complex conjugate can be used as the subtraction term.

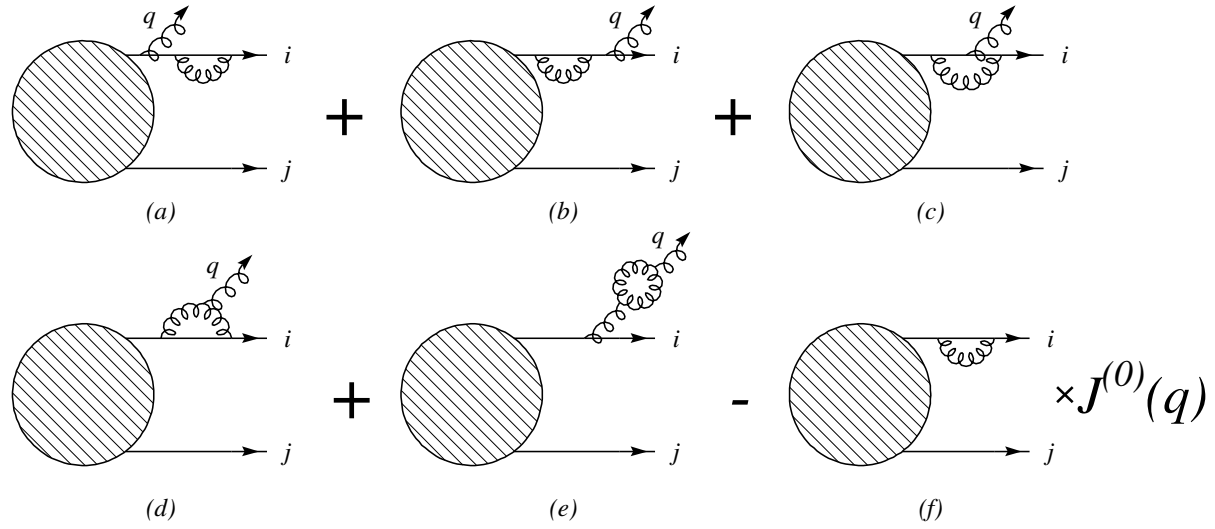

Figure 3.6.: Feynman diagrams, where the momentum k only couples to one external line. Figure taken from [87].

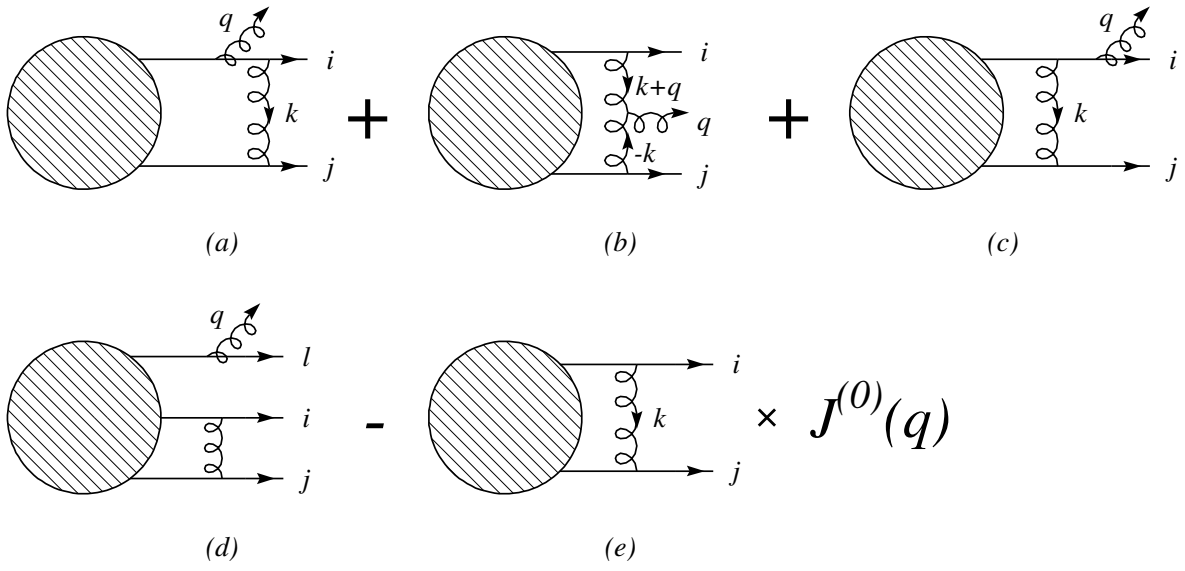

Figure 3.7.: Feynman diagrams, where the momentum k couples to to or three external momenta. Figure taken from [87].

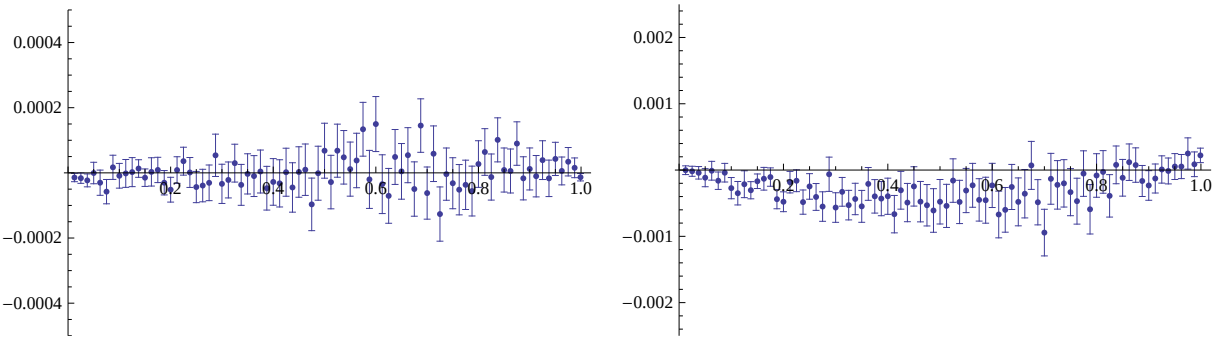

Figure 3.8.: The numeric error of the NNLO cross section can be estimated from the rest, which remains after the cancellation of the ϵ^{-2} and ϵ^{-1} terms. Left: Absolute error in the ϵ^{-2} nl^0 term. Right: Absolute error in the ϵ^{-1} nl^0 term.

3.4. Results of the Total Cross Section $\sigma_{q\bar{q}\to t\bar{t}}$

Combining the three different parts, which were described above, and the double virtual correction, which will be described in the next chapter, results in the total cross section $\sigma_{q\bar{q}\to t\bar{t}}$. In this section I want to present the results of the NNLO QCD cross section in the quark anti-quark annihilation channel [89], which dominates the top quark pair production at the Tevatron by 90%. It is the first two-to-two process for hadron colliders, which was calculated at NNLO level and involves massive fermions.

While the single parts are divergent the overall result must be finite. This is guaranteed by the Kinoshita-Lee-Nauenberg theorem, which states that observables, like cross sections, calculated within the Standard Model are infrared safe. This implies that IR singularities, coming from real radiation, cancel with IR divergences from loop integrals. UV singularities are absorbed by the renormalization procedure. Therefore, all four renormalized parts (see Figure 3.1) combined have to be completely of free of divergences. The cancellation of the divergencies can be used as a check and it reveals the quality of the numerical methods. The absolut numeric errors, estimated by the the rest of the divergency cancellation, are given in Figure 3.8 and 3.9. Both, the difference of the ϵ^{-2} term and the ϵ^{-1} term are plotted and they are seperated for terms which are proporsional to nl^0 and nl^1 respectively (nl is the number of light flavours) . The result for nl^2 is known analytically and is:

$$\sigma_{nl^2}(\beta) = \sigma_0(\beta)(25 - 3\pi^2 + 30\log[(1-\beta^2)/4] + 9\log[(1-\beta^2)/4]^2)/(108\pi^2), \tag{3.21}$$

where $\sigma_0(\beta)$ is the Born cross section.

The individual parts of $\sigma_{q\bar{q}\to t\bar{t}}$ could partly be checked, as was shown in the sections above. For the whole cross section no independent calculation was performed. Nevertheless, results from threshold expansion allow a comparison in the threshold region. Soft gluon und Coulomb resummation constraints the result of the amplitude in the low energy limit. The total cross

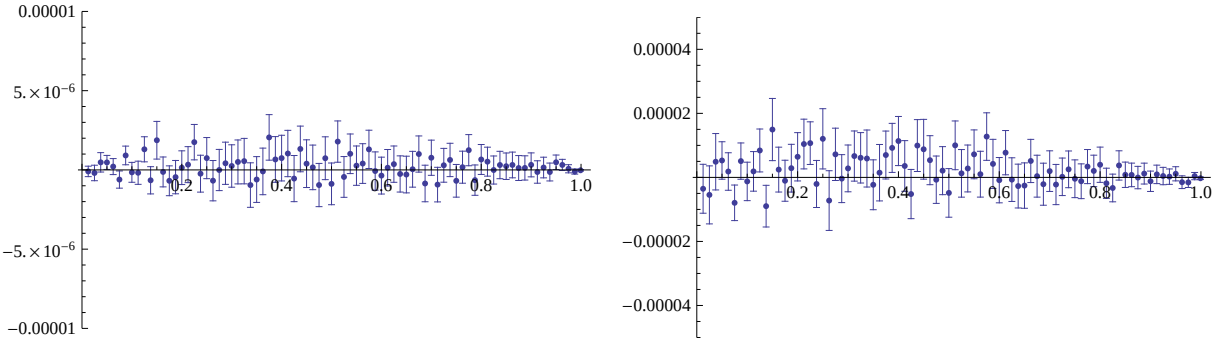

Figure 3.9.: Left: Absolute error in the ϵ^{-2} nl^1 term. Right: Absolute error in the ϵ^{-1} nl^1 term. The nl^2 term is known completely analytically.

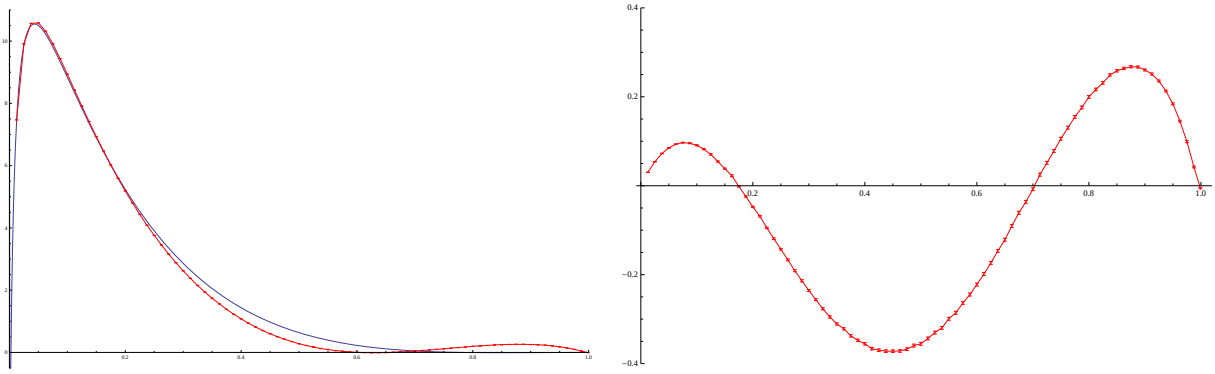

Figure 3.10.: Left: Comparison of the exact numeric result of the nl^0 term of $\sigma_{q\bar{q}\to t\bar{t}}$ with the approximated result from threshold expansion (given in [90]). The constant $C_{q\bar{q}}$ was set to 0. Right: Difference that needs to be added to the approximated cross section to obtain the exact result for nl^0. The slope of the curve near threshold can be used to extract an approximation for the value of the constant $C_{q\bar{q}}$.

section in the threshold region was computed in e.g. [5] and is completely known up to NNLL order up to a constant. This gives a check in the low-energy regime for the total cross section. In the Figures 3.10 and 3.11 both results, the exact numeric NNLO result, and the threshold approximation are plotted for the nl^0 and nl^1 term respectively. On the right hand side the absolute difference of the two results is plotted.

Finally, in Figure 3.12 the numeric combined NNLO result (which includes nl^0, nl^1 and nl^2 terms) is plotted, whereby nl is set to 5. This result is compared with the approximated result from threshold expansion. A lucky circumstance for the threshold expansion is that the exact calculation is bigger at small values for β and smaller at medium values for β (high values for β are suppressed by the flux). Therefore the difference between these two independent calculations cancels partly and the finial difference is small.

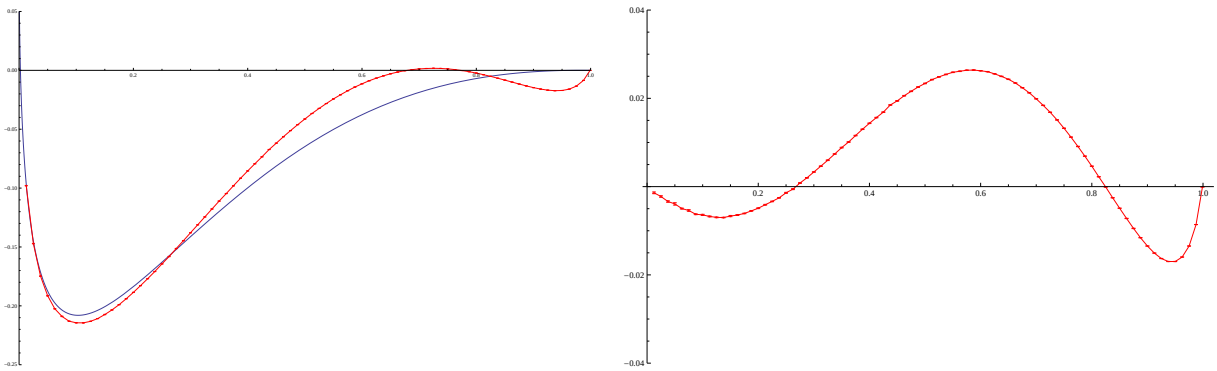

Figure 3.11.: Left: Comparison of the numeric result of the nl^1 term of $\sigma_{q\bar{q}\to t\bar{t}}$ with the approximated result from threshold expansion (given in [90]). The constant $C_{q\bar{q}}$ was set to 0. Right: Difference that needs to be added to the approximated cross section to obtain the exact result for nl^1. The slope of the curve near threshold can be used to extract an approximation for the value of the $C_{q\bar{q}}$ constant.

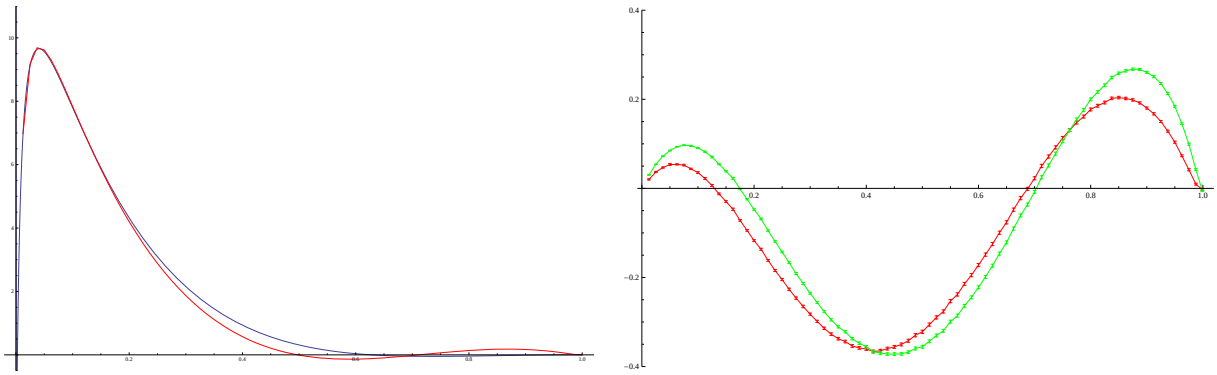

Figure 3.12.: Left: Comparison of the numeric result of $\sigma_{q\bar{q}\to t\bar{t}}$ (nl=5) with the approximated result from threshold expansion (given in [90]). The constant $C_{q\bar{q}}$ was set to 0. Right: Difference that needs to be added to the approximated cross section in order to obtain the exact NNLO result. The green curve only takes the nl^0 contribution into account, the red one the nl^1 an nl^2 as well.

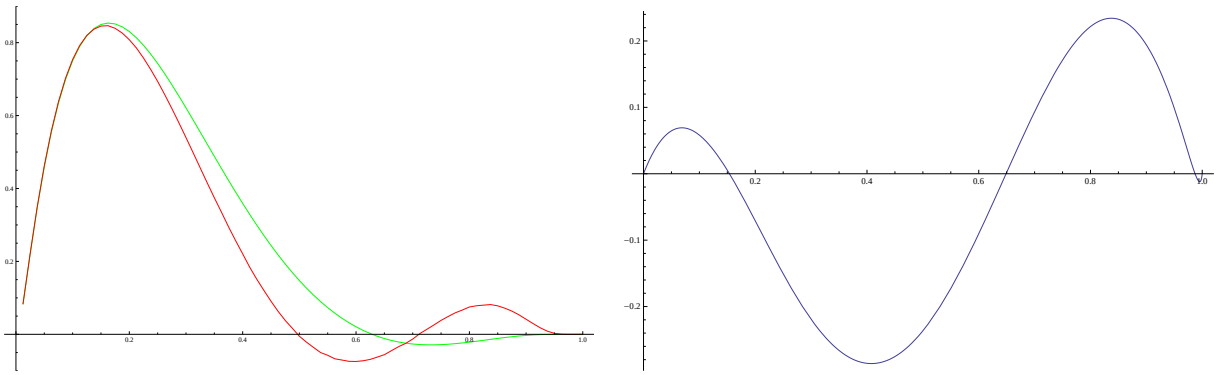

Figure 3.13.: Left: Plots generated after inclusion of the flux. The red curve shows the exact numeric NNLO result, whereas the approximated result is shown by the green curve. Right: The difference which has to be added to the approximated result in order to get the exact NNLO result is shown. Both plots only contain the nl^0 and nl^1 corrections, since the nl^2 contributions are known analytically.

In Figure 3.13 the cross section is plotted after the convolution with the flux. For the two-loop contribution, the finite part was taken from [75], and the analytically known poles were taken from [64]. The calculation of the other three parts is described above.

From numeric investigation we found that the error of each point of the NNLO partonic cross section is normally much lower than 1%. Higher numeric errors only appear in the low energy limit, where $\beta > 0.999$. While this region is completely irrelevant for top quark pair production it might be relevant for light quark production, like bottom quarks. The reason that this tiny region $0.999 < \beta < 1$ could influence the value of the cross section is that the partonic flux ϕ has a peak at $\beta \sim 1$.
The results can be used to estimate the constant $C^2_{q\bar{q}}$, which could not be calculated by the soft-gluon resummation approach, explained in Section 2.2.1. As result we get the following values:

$$C^2_{q\bar{q}} = 1195.82 - 44.1841\mathrm{nl} - 4.28168\mathrm{nl}^2, \tag{3.22}$$

where nl is the number of light flavors. Assuming a polynomial fit in β, the constant can be determined to a precision better than 10%, what results in a an error of the cross section in the sub-permil region. For more information see [89].

Finally, the impact of the cross section calculation to the Tevatron data is described. This new results were implemented in the program top++ [91]. Setting the top mass to $m_t = 173.3$ GeV and using the MSTW2008nnlo68cl pdf-set, the result for the cross section is:

$$\sigma^{NNLO}_{tot} = 7.005\ ^{+0.202}_{-0.310}[\mathrm{scales}]\ ^{+0.170}_{-0.122}[\mathrm{pdf}] \tag{3.23}$$

This includes the NNLO contribution in the $q\overline{q}$-channel and the approximated NNLO result in the gg-channel [92]. Thereby, the unknown constant was set to zero, $C_{gg}^2 = 0$, and it is verified that the choice of the constant has a very small impact on the final result.
The result can be improved by adding higher order resummation effects: $\sigma_{tot}^{res} = \sigma_{tot}^{NNLO+NNLL}$. Thereby the NNLL resummation [92] is matched to the exact NNLO result for the $q\overline{q}$-channel and to the approximated NNLO result for the gg-channel.

$$\sigma_{tot}^{res} = 7.067\ ^{+0.143}_{-0.232}[\text{scales}]\ ^{+0.186}_{-0.122}[\text{pdf}] \tag{3.24}$$

This is up to now the best theoretical result for the total cross section. The predicted theoretical uncertainty due to scale variation is with $\pm 2.7\%$ very small and it is exacted that this value could even drop below 2% including all kinds of effects. This makes the total top quark pair production cross section to the best known collider observable. The same methods will be used to improve the prediction for the LHC and for different processes like the production of di-$jets$, W + jet and $Higgs$ + jet.

4. The NNLO Virtual Contributions of the Gluon Fusion Channel

4.1. Overview

In this Chapter the evaluation of the double virtual contributions $\hat{\sigma}^{VV}_{gg\to t\bar{t}}$, is explained in detail. Together with the double real contribution, it is the most challenging one. The double real corrections of the quark anti-quark annihilation channel were published in 2008 [93], but necessary improvements for small values of β where implemented by the author. The double real corrections of the gluon fusion channel was obtained by the author alone.

As in all $2 \to 2$ processes, the differential cross section $d\hat{\sigma}_{gg\to t\bar{t}}$ depends on the two Mandelstam varibles s and t, where s is the total energy of the two colliding partons and t describes the direction in which the two outgoing top quarks are scattered with respect to the beam line[1]. The phase space of the differential cross section is pictured in Figure 4.1. It is parametrized in the independent variables β and x, where

$$\begin{aligned} m_s &= \frac{m_{top}^2}{s} \\ \beta &= \sqrt{(1 - 4\, m_s)} \\ x &= m_s + \frac{t}{s} \end{aligned} \tag{4.1}$$

Consequentially,

$$x \in \left[\frac{1}{2}(1-\beta),\ \frac{1}{2}(1+\beta)\right] \tag{4.2}$$

Figure 4.2 and Figure 4.3 show the result of the soft gluon resummation taken from [90] and the contribution of the double virtual diagrams in the $q\bar{q}$-channel and in the gg-channel respectively. The first can be taken as an approximation to the complete cross section, at least for $\beta \leq 0.5$. At low and at high values for beta, the double virtual contributions are large, relative to the result obtained from soft gluon resummation. This is especially true for low values for β in the $q\bar{q}$-channel. Hence, in these regions large cancellations occur between the 4 different kinds of

[1] $s = (p_1 + p_2)^2, t = (p_1 - p_3)^2, u = (p_1 - p_4)^2$

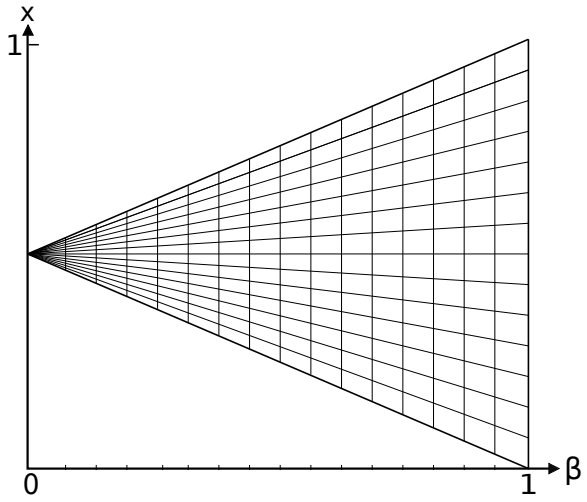

Figure 4.1.: Phase space of the double virtual corrections as a function of β and x (see Equation 4.1 for their definition) with grid.

diagramms (see Figure 2.9 and therefore the result of the double virtual part has to be known to a high precision. Therefore different methods had to be developed for the calculation of the phase space points, each fitted to the special condition of their phase space region (see Figure 4.4).

The high-energy region ($m_{top}^2 \ll s$) was obtained using the Mellin-Barnes method (see Section 4.2). For the determination of the middle range the method of differential equations was used (Section 4.3) and the low-energy regime was evaluated with an expansion around the threshold (Section 4.4). Our results and checks are presented in Section 4.5 and 4.6 respectively.

4.2. The High-Energy Limit

The following section explains the procedure for the calculation of the high-energy limit. It starts with the 2-loop virtual diagrams and how to derive the master integrals through IBP relations. Afterwards, the method of differential equations is introduced which determines the structure of the master integrals. The following subsection deals with the calculation of the boundaries, which cannot be determined from the differential equations. Several tools are presented.

4.2.1. From Feynman Diagrams to Master Integrals

As shown in Chapter 2, four different parts have to be calculated in order to obtain the top quark pair cross section at NNLO-level. The calculation of the NNLO virtual contribution in the gluon fusion channel turned out to be much more difficult than for the $q\overline{q}$-channel [93]. There are several reasons for this. First, there are more 2-loop diagrams in the gg-channel (726 different

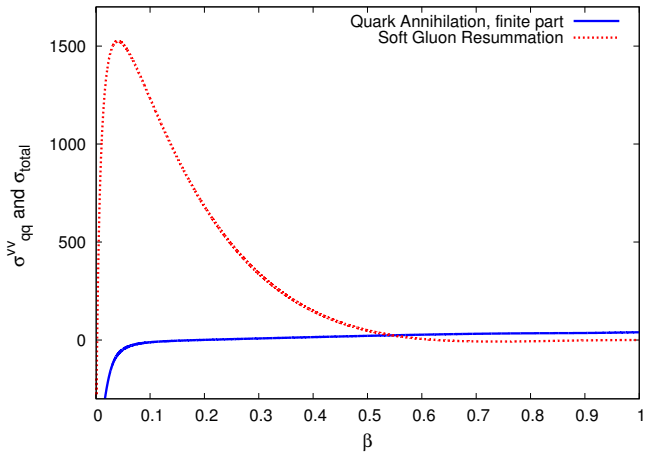

Figure 4.2.: Result of the double virtual contributions (in the $q\bar{q}$-channel) taken from [93] (blue-continuous) and the result of the soft gluon resummation as given in [90] to NNLL (red-dashed). These plots are used to estimate in which areas the calculation has to be particularly precise.

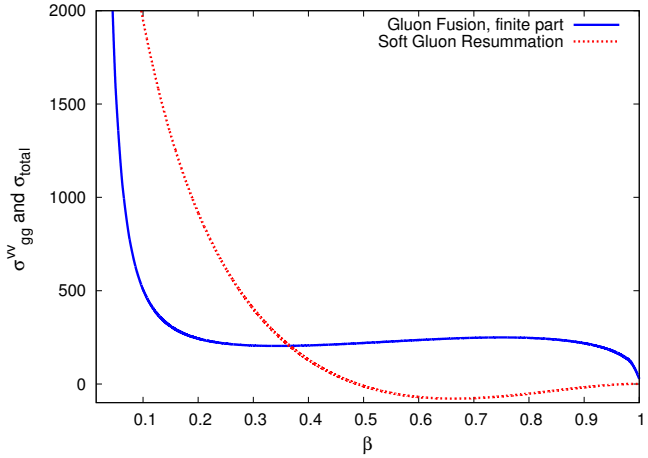

Figure 4.3.: Low precision preliminary result of the double virtual contributions to the gluon fusion channel (blue) and the result of the soft gluon resummation as given in [90] to NNLL (red-dashed).

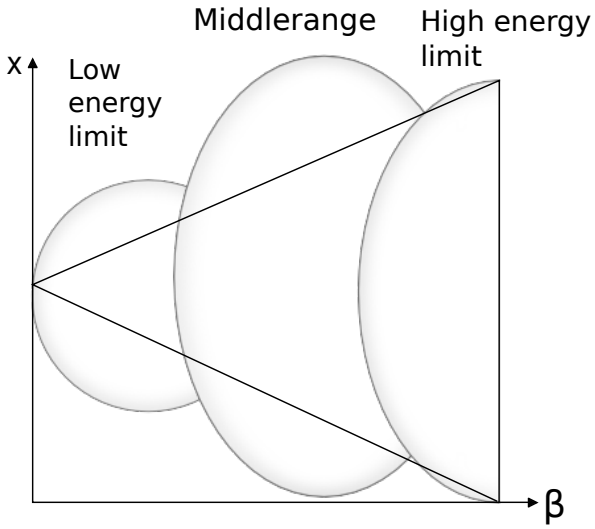

Figure 4.4.: Phase space of the double virtual corrections. In each region a different method had to be used to get excellent results.

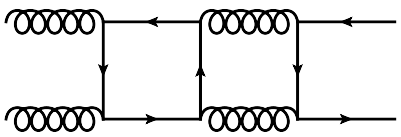

Figure 4.5.: 2-loop diagram with one closed fermion loop inside. Such diagrams do not appear in the $q\bar{q}$-channel.

diagrams), because gluons have more possibilities to couple to other particles than quarks (190 different NNLO diagrams in the $q\bar{q}$-channel). Second, these diagrams get multiplied by the Born diagrams. There are three different ones in the gg-channel, but only one in the $q\bar{q}$-channel. After using the Laporta algorithm [59], 145 Master integrals have to be calculated in the $q\bar{q}$-channel and 422 in the gg-channel. Moreover, the number of NP-integrals[2], which are especially difficult to calculate, increases drastically. There are 6 NP 7-liner diagrams in the quark channel and 60 in the gluon channel. These were by far the most time consuming master integrals. In addition, the NP-master integrals in the gluon channel contain in general more massive lines, which lead to worse Mellin-Barnes representations. For example, in the gluon channel there are 2-loop diagrams with a closed heavy-fermion box inside Figure 4.5, which do not appear in the $q\bar{q}$-channel.

For the calculation of the master integrals the same methods have been used in the $q\bar{q}$- and gg-channels. In this section the procedure of their calculation is outlined.
For the calculation of the cross section all Feynman diagrams up to order α_s^3 were generated

[2]NP stands for non-planar

by `DiaGen` [94]. The number of diagrams depends heavily on the requested order of α_s. In the gg-channel there are 3 diagrams at tree-level, 33 diagrams at NLO and 726 at NNLO-level for the virtual two-loop contributions.
Applying Feynman rules, these diagrams can be written as Feynman integrals, where a loop is expressed as an integration over a loop momentum. To obtain the cross section, they get multiplied by the tree-level diagrams.
In general, these Feynman integrals contain a rich structure of Lorentz and color indices, which get contracted by `form` [95] routines. The result is averaged over spins and colors, so that it is only a function of the number of colors N_C. Therefore, we will consider in the following only integrals without Lorentz and color indices. In the $q\overline{q}$-channel 2812, in the gg-channel 8676 integrals have to be calculated.
Fortunately, there exist relations between these integrals. Therefore the calculation of a small group of so-called 'master integrals' is sufficient to get a result for all integrals. The relations between the integrals are the result of integration-by-parts (IBP) relations [96], which are based on a disappearance of the surface terms $\int d^dk \frac{\partial}{\partial k^\mu}(k^\mu f) = 0$ and $\int d^dk \frac{\partial}{\partial k^\mu}(q^\mu f) = 0$. In the following, an example for the reduction of a set of integrals to master integrals via IBP relations is given:

The one-loop self-energy diagram from Figure 4.6 can be written as Feynman integral as

$$I(q^2, m^2, d, a_1, a_2) = \int \frac{d^dk}{(k^2-m^2)^{a_1}((q-k)^2)^{a_2}}. \tag{4.3}$$

An explicit calculation of the IBP relations $\frac{\partial}{\partial k^\mu} k^\mu f(a_1, a_2)$ and $q^\mu \frac{\partial}{\partial k^\mu} f(a_1, a_2)$ (where f is the integrand of Formula 4.3) gives the relations

$$(d-2a_1-a_2)f(a_1,a_2)-2m^2a_1f(a_1+1,a_2)-a_2f(a_1-1,a_2+1)+a_2(q^2-m^2)f(a_1,a_2+1) = 0 \tag{4.4}$$

and

$$\begin{aligned}(a_2-a_1)f(a_1,a_2) + a_1f(a_1+1,a_2-1) - a_1(q^2+m^2)f(a_1+1,a_2)\\ -a_2f(a_1-1,a_2+1) + a_2(q^2-m^2)f(a_1,a_2+2) = 0.\end{aligned} \tag{4.5}$$

Setting a_1 to $a_1 - 1$, the difference of both equations results in

$$f(a_1,a_2) = \frac{1}{(a_1-1)(q^2-m^2)}((-d-1+a_1+2a_2)f(a_1-1,a_2) + (a_1-1)f(a_1,a_2-1)) \tag{4.6}$$

For $a_1 = 2$ and $a_2 = 1$ the result is $f(2,1) = \frac{1}{(q^2-m^2)}((-1+2\varepsilon)f(1,1) + f(2,0))$. It is important to notice that integrals of higher order in a_1 and a_2 can be expressed through integrals of lower order. Applying the reduction formula recursively, all integrals can be reduced to a set of master integrals, which contains $f(1,1)$, $f(0,a_2)$ (which are massless tadpole diagrams and hence 0) and $f(a_1,0)$, which have to be calculated. Knowing these master integrals all integrals can be obtained by using the IBP relations above.

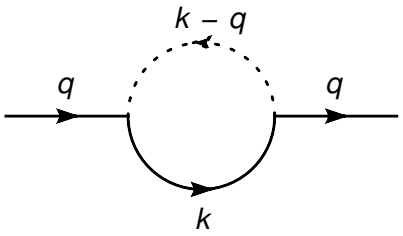

Figure 4.6.: One loop self-energy diagram of a particle with spin 0 and mass m. The datched line symbolizes a massless spin 0 particle.

Selection of the Master Integrals There is an ambiguity within the choice of the master integrals and therefore a basis, which is as simple as possible to calculate, should be chosen. Using the Laporta algorithm [59] ensures that the remaining master integrals are tensor integrals with the lowest possible order, since these are normally the easiest to calculate. Often an ambiguity in the selection remains.
The cross section, like all observables, is finite in 4 dimensions for any physical process. This implies that the ε poles cancel each other. The cross section σ is the squared sum of all the Feynman diagrams F, $\sigma \approx |\sum_i F_i|^2$. Hence it is sufficient to know all Feynman diagrams to order $\mathrm{O}(\varepsilon^0)$. In the case of master integrals the cross section is given as $\sigma \approx \sum_i C_i M_i$. The coefficients C_i can have so called spurious poles in ε, so that the master integral M_i has to be known to a higher order in ε, which complicates the calculation considerably. In principle a basis of master integrals can be found, which has no spurious poles in ε and m_s, in practice no prescription is known to derive it. In the calculation for $\sigma_{t\bar{t}}$ it was necessary to ensure, that diagrams with 6 or 7 internal propagators did not have spurious poles, because a calculation of these would have been impossible. This is achieved by a change of basis.

4.2.2. Method of Differential Equations

The idea of the method of differential equations is to differentiate a master integral M and express the result again in terms of master integrals by using IBP relations

$$\frac{d}{dy} M_i = \sum \text{tensor integrals} = \sum J_{ij}\, M_j, \tag{4.7}$$

where J_{ij} are the coefficients and y is a kinematic invariant.

Construction of the differential equations

In the case of top quark pair production the kinematic invariants m_s and x (see Equation 4.1) are used. We can perform a Laurent expansion for the master integrals

$$M_i = \sum_{j=-4}^{j_i^{max}} \varepsilon^j z_{n+j}(x, m_s) \tag{4.8}$$

and treat each coefficient z_k independently. In the $q\bar{q}$-channel 595 equations were generated, in the gg-channel 1263 equations, for each kinematic invariant.

$$\begin{aligned} \frac{d}{dm_s} z_i(x, m_s) &= \sum \text{tensor integrals} = \sum J_{ij}^{m_s}(x, m_s)\ z_j(x, m_s) \\ \frac{d}{dx} z_i(x, m_s) &= \sum \text{tensor integrals} = \sum J_{ij}^{x}(x, m_s)\ z_j(x, m_s) \end{aligned} \tag{4.9}$$

It is important to notice that, if the left-hand side is an n-liner[3], the right-hand side only depends on master integrals which are of order n or less. This means the (only) 2-liner depends only on itself, the 3-liners on the the 2-liner and the other 3-liners and so on. The whole system can hence be written in block-diagonal form of 1263 (or 595 in th $q\bar{q}$-channel respectively) linear inhomogeneous differential equations

$$\frac{d}{dy} \vec{Z}(x, m_s) = J^y(x, m_s)\ \vec{Z}(x, m_s)\ , \tag{4.10}$$

where $\vec{Z}$ is a vector with 595 (1263) entries and J^y is a quadratic, lower triangular block-matrix and y stands for x or m_s respectively.

Solving the differential equations

Unfortunately a direct integration of the system 4.9 is not possible, because the appearing functions are not known at present, but the system can be solved in the high-energy limit where $m_s \ll \frac{1}{4}$. Solving the differential equations recursively up to order m_s^0, determines the whole analytic structure of the master integrals up to that order (this means the complete dependence on the two kinematic variables m_s and x (like $log(m_s)$) is fixed). Only the boundaries cannot be determined and remain unknown (see Section 4.2.3 for their calculation). Therefore, the differential equations provide a powerful tool to calculate and to check the analytic structure of the master integrals.
The system of differential equations gets solved recursively, due to its triangular block structure. Problems arise when there are more than two coupled differential equations. In these cases no general solution is known. In practice I use two tricks:

- Firstly, it was often possible to decouple at least one master from the system by choosing another basis of master integrals.
- Secondly, a sophisticated ansatz in m_s and x was made for the master integrals belonging to the coupled system. This ansatz was entered into both differential equations, which yields relations between the different terms in the ansatz. The remaining expression is the solution of the coupled system of differential equations (because it fulfills both equations by construction) and depends only on the boundaries of the master integrals. The ansatz was correct if as many boundaries remain as there are coupled equations.

[3]This means, it has n internal propagators.

The position of the boundary with respect to m_s and x is determined by the homogeneous system of the differential equations. It is defined by

$$\frac{d}{dy}\vec{Z}(x, m_s) = J^y(x, m_s)\ \vec{Z}(x, m_s), \tag{4.11}$$

with the block-diagonal matrix J^y. In most cases the boundary lies at the 0-th order of the two kinematic invariants, but a negative order simplified the calculation of the boundary significantly (see Section 4.2.3). In both channels some masters have their boundary at half-integer power like $m_s^{-\frac{1}{2}}$. These square root contributions cancel in the amplitude of the $q\overline{q}$-channel, but remain in the gg-channel.

Generating the master integrals to arbitrary power in m_s

Having obtained the result up to order m_s^0, Equation 4.9 can be used in principle to obtain all masters to arbitrary power in m_s by using a power-log ansatz for z:

$$\vec{Z}_i(m_s) = \sum_{j=-2}^{j=10} \sum_{k=0}^{k=4} c(i, j, k)\ m_s^j\ \log(m_s)^k, \tag{4.12}$$

In practice, this is restricted by the available computer resources. In both channels we achieve the result up to order m_s^{10}, which leads to a high precision result for the amplitude in the high-energy region (see Figure 4.4), where $m_s \to 0$, or $\beta \to 1$. Unfortunately, the radius of convergence for the master integrals and the amplitude turned out to be small, so that it covers only a tiny area.

Error estimation for the high-energy limit

The valid precision in the high-energy limit is only limited by the finite expansion in m_s. The quotient of the m_s^{10} term and the complete result to that power is taken as an error estimate. For $\beta = 0.9990$ ($m_s = 0.0005$) the error estimation for the amplitude gives $\sim 10^{-18}$. It turns out that the convergence radius of the amplitude is very small and only for values where β is very close to 1, the high-energy limit can be used as an approximation.
It is important to know, that the small mass expansion is actually an expansion in $\max(m_s, -m^2/t, -m^2/u)$, instead of m_s, where s, t, u are the Mandelstam variables. For small m and at the kinematical boundary which corresponds to forward scattering ($-m^2/t \gg 0$)

$$-\frac{m^2}{t} = -\frac{2m^2}{s\left(1 - \sqrt{1 - \frac{4m^2}{s}}\right)} \approx -1\ . \tag{4.13}$$

A similar relation is correct for backward scattering ($-m^2/u \gg 0$). In consequence, the convergence of the series will be worst at the kinematic boundaries ($x \sim 0$ or $x \sim 1$).

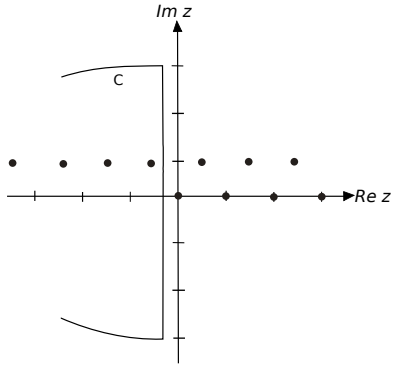

Figure 4.7.: Contour C and the poles of the Γ-function of the Feynman integral 4.18 with $\varepsilon = -\frac{1}{2} - i$.

4.2.3. Determination of the Boundaries

One of the main tasks of my work was the calculation of the boundaries of the differential equations introduced in Section 4.2.2. The methods used to calculate them will be presented in the following. The procedure is to generate a Mellin-Barnes representation, expanding it in ε and afterwards in m_s and x. Various tools stand to one's disposal for the final calculation. Among them, Barnes Lemmas [97], XSummer [98] or the PSLQ algorithm [99].

The Mellin-Barnes Representation

The necessity for the calculation of Feynman integrals arises naturally in perturbative quantum field theory. Various different methods have been developed during the last 60 years to obtain analytic or numeric results, like the Feynman parameters, α parameters or Cutkosky rules. A very powerful method is the Mellin-Barnes (MB) method. The basic idea for MB and Feynman parameters is easy and similar. New integrals over auxiliary parameters x_i (or z_i respectively) are introduced to simplify the integrand. Afterwards it is possible to integrate over the loop momenta and simpler integrals over the auxiliary parameter remain.
The Mellin-Barnes formula is given by:

$$\frac{1}{(X+Y)^\lambda} = \frac{1}{2\pi i}\frac{1}{\Gamma(\lambda)}\int_{-i\infty}^{i\infty} dz\, \Gamma(\lambda+z)\Gamma(-z)\frac{Y^z}{X^{\lambda+z}} \tag{4.14}$$

The Γ-functions have singularities at negative integers and 0. The integration contour runs from $-i\,\infty$ to $i\,\infty$, whereas all poles of the form $\Gamma(...+z)$ lie on the left hand side of the contour (left poles) and all poles of the form $\Gamma(...-z)$ lie on the right hand side of the contour (right poles) [4]. Such contours and poles are shown in Figure 4.7 and Figure 4.8.
As an example, we will come back to the Feynman integral from Figure 4.6, or Equation 4.3 respectively. Using Equation 4.14 gives:

[4] As it can be seen in Figure 4.8, it can happen that right poles lie more left than left poles and vice versa.

$$\frac{1}{(m^2-k^2)^{a_1}} = \frac{1}{2\pi i}\frac{1}{\Gamma(a_1)}\int_{-i\infty}^{i\infty} dz\,\Gamma(a_1+z)\Gamma(-z)\frac{(m^2)^z}{(-k^2)^{a_1+z}} \tag{4.15}$$

Plugging the result into Equation 4.3 yields:

$$I(q^2,m^2,d,a_1,a_2) = \frac{1}{2\pi i}\frac{(-1)^{a_1}}{\Gamma(a_1)}\int d^dk\int_{-i\infty}^{i\infty} dz\,\Gamma(a_1+z)\Gamma(-z)\frac{(m^2)^z}{(-k^2)^{a_1+z}}\frac{1}{((q-k)^2)^{a_2}} \tag{4.16}$$

After the interchange of the integrals and integrating over the loop momenta k, we obtain the following result, where the contour runs between the left and right poles along the imaginary axis.

$$\begin{aligned} I(q^2,m^2,d,a_1,a_2) = {} & \frac{i\pi^{d/2}(-1)^{a_1+a_2}\Gamma(2-\varepsilon-a_2)}{\Gamma(a_1)\Gamma(a_2)(-q^2)^{a_1+a_2+\varepsilon-2}}\frac{1}{2\pi i}\int_{-i\infty}^{i\infty} dz\left(\frac{m^2}{-q^2}\right)^z \\ & \Gamma(a_1+a_2+\varepsilon-2+z)\frac{\Gamma(2-\varepsilon-a_1-z)\Gamma(-z)}{\Gamma(4-2\varepsilon-a_1-a_2-z)} \end{aligned} \tag{4.17}$$

The formula can be used for the calculation of the Feynman integral for arbitrary values of a_1, a_2 For the special case of $a_1 = 1, a_2 = 1$ or $a_1 = 2, a_2 = 1$ the following formula are obtained. In Figure 4.7, the contour and poles are given for $a_1 = 2, a_2 = 1$ and in Figure 4.8 for $a_1 = 1, a_2 = 1$.

$$I(q^2,m^2,d,2,1) = \frac{-i\pi^{d/2}\Gamma(1-\varepsilon)}{(-q^2)^{1+\varepsilon}}\frac{1}{2\pi i}\int_{-i\infty}^{i\infty} dz\left(\frac{m^2}{-q^2}\right)^z\Gamma(1+\varepsilon+z)\frac{\Gamma(-\varepsilon-z)\Gamma(-z)}{\Gamma(1-2\varepsilon-z)} \tag{4.18}$$

$$I(q^2,m^2,d,1,1) = \frac{i\pi^{d/2}\Gamma(1-\varepsilon)}{(-q^2)^{\varepsilon}}\frac{1}{2\pi i}\int_{-i\infty}^{i\infty} dz\left(\frac{m^2}{-q^2}\right)^z\Gamma(\varepsilon+z)\frac{\Gamma(1-\varepsilon-z)\Gamma(-z)}{\Gamma(2-2\varepsilon-z)} \tag{4.19}$$

MBrepresentation The approach described above has the disadvantage that the integration over the loop momenta cannot be implemented as a computer algorithm. On the other hand it is known, that every Feynman integral can be transformed with the help of the Feynman parameters to the following form [96, 100]:

$$\mathrm{G[T(k)]} = \frac{(-1)^{N_\nu}\Gamma(N_\nu-\frac{d}{2}L)}{\prod_{i=1}^N\Gamma(\nu_i)}\int_0^1\prod_{j=1}^N dx^j x_j^{\nu_j-1}\delta(1-\sum_{i=1}^N x_i)\frac{U(x^{N_\nu-d(L+1)/2})}{F(x)^{N_\nu-dL/2}}P(T(k)) \tag{4.20}$$

ν_i are the exponents of the propagators of the Feynman integral, $N_\nu = \sum\nu_i$, x_i are called Feynman parameters, N is the number of propagators, L the number of loops and P is a function

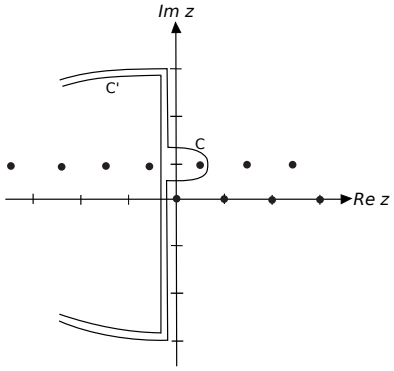

Figure 4.8.: The poles of the Γ-function and the contour C of the Feynman integral 4.19 with $\varepsilon = -\frac{1}{2} - i$. Moreover the contour C' is plotted, which results from taking the residue at $z = -\varepsilon$.

of the tensor structure $T(k)$ of the Feynman integral. F(x) and U(x) are polynomials and characterize the topology of the Feynman integral. In order to carry out the integration over the Feynman parameters, the F-polynomial gets fractionized into monomials with the help of the Mellin-Barnes representation (Equation 4.14). This method was implemented in the Mathematica package `MBrepresentation` [101]. In the case of non-planar diagrams, different polynomials were tried manually, to obtain the most convenient representation for further calculation.

Expansion in ε

In quantum field theory Feynman diagrams are often singular. These singularities have to cancel when physical observables are calculated. Various methods, like Cut Off or Pauli-Villars have been introduced to handle these singularities. The most common regularization scheme nowadays is dimensional regularization. Instead of integrating the diagrams over 4 dimension, it is integrated over d dimensions, where $d = 4 - 2\,\varepsilon$, with a small parameter ε. Expanding around $\varepsilon = 0$ gives the Laurent series and diverges in the limit $\varepsilon \to 0$. In a physical observables, like a cross section, these divergent ε poles cancel, so that the limit $\varepsilon \to 0$ can be done safely.
In the last section we derived a MB representation for Figure 4.6, or Formula 3.15 respectively. An expansion in ε simplifies the following integration significantly. Only finite terms in ε have to be kept. The singular behavior of Feynman diagrams expresses itself in a MB representation, that for $\varepsilon \to 0$ a right and a left pole collide. At $\varepsilon = 0$ their distance is zero, so that the contour cannot pass between these poles.

For the special case of $a_1 = 2$ and $a_2 = 1$ (Equation 4.18), the contour is a straight line along the imaginary axis (Figure 4.7) . Assuming that the integrand vanishes at infinity, the integral can be closed with a semi circle to either side. The Cauchy theorem states, that the value of an integral over a closed loop is the same as the sum of the enclosed residues. So, the integral transforms into a sum. For the following special case no divergences arise.

$$
\begin{aligned}
I(q^2, m^2, d = 4, 2, 1) &= \frac{i\pi^2}{q^2} \frac{1}{2\pi i} \int_{-i\infty}^{i\infty} dz \left(\frac{m^2}{-q^2}\right)^z \frac{\Gamma(1+z)\Gamma(-z)^2}{\Gamma(1-z)} \\
&= -\frac{i\pi^2}{q^2} \frac{1}{2\pi i} \int_{-i\infty}^{i\infty} dz \left(\frac{m^2}{-q^2}\right)^z \Gamma(+z)\Gamma(-z) \qquad (4.21)
\end{aligned}
$$

The residue of $\Gamma(-z)$ is $\frac{(-1)^z}{z!}$ for $z = 0, 1, 2, 3....$ Taking the residues results in the series:

$$
I(q^2, m^2, 4, 2, 1) = \frac{i\pi^2}{q^2} \ln\left(\frac{-q^2}{m^2}\right) + \frac{i\pi^2}{q^2} \sum_{n=1}^{\infty} \frac{1}{n} \left(\frac{m^2}{q^2}\right)^n = \frac{i\pi^2}{q^2} \ln(1 - \frac{q^2}{m^2}) \qquad (4.22)
$$

The case $a_1 = 1$ and $a_2 = 1$ leads to

$$
I(q^2, m^2, d, 1, 1) = \frac{i\pi^{d/2}\Gamma(1-\varepsilon)}{(-q^2)^{\varepsilon}} \frac{1}{2\pi i} \int_{-i\infty}^{i\infty} dz \left(\frac{m^2}{-q^2}\right)^z \Gamma(\varepsilon + z) \frac{\Gamma(1-\varepsilon-z)\Gamma(-z)}{\Gamma(2-2\varepsilon-z)} \qquad (4.23)
$$

and is slightly more complicated. As it can be seen in Figure 4.8, the contour is no straight line and for $\varepsilon \to 0$ the poles of the functions $\Gamma(\varepsilon + z)$ and $\Gamma(-z)$ from Equation 4.23 collide. The limit $\varepsilon = 0$ is forbidden, since the contour cannot pass between the left and the right pole. To solve this problem, contour C is transformed to a contour C' (compare Figure 4.8) by raising contour over the left pole which is located most right. This means mathematically that the residue is taken at $z = -\varepsilon$. Afterwards ε can be set to zero. The integral gets split into two pieces. The first one is the original integral over the new contour C', the second is the residue at the critical point $z = -\varepsilon$. This part contains the singularity for $\varepsilon \to 0$.

$$
\mathrm{Res}(z = -\varepsilon) = i\pi^2 \frac{\Gamma(\varepsilon)}{(m^2)^{\varepsilon}(1-\varepsilon)} \qquad (4.24)
$$

The divergence is hidden inside the term $\Gamma(\varepsilon) \approx \frac{1}{\varepsilon} - \gamma_E$, where γ_E[5] is the Euler-Mascheroni constant. The integral over the new contour C' can be calculated for $\varepsilon \to 0$, as it was done for the case $a_1 = 2$ and $a_2 = 1$. The contour is closed by a semicircle, and the residues which lie within the enclosed area are taken.

$$
I'(q^2, m^2, d, 1, 1) = i\pi^2 \frac{1}{2\pi i} \int_{-i\infty}^{i\infty} dz \left(\frac{m^2}{-q^2}\right)^z \frac{\Gamma(-z)\Gamma(z)\Gamma(1-z)}{\Gamma(2-z)} \qquad (4.25)
$$

The final result is the sum of these two parts and up to $\mathrm{O}(\varepsilon^0)$ it is:

$$
I(q^2, m^2, d, 1, 1) = i\pi^2 e^{\gamma_E \varepsilon} \left[\frac{1}{\varepsilon} - \ln(m^2) + 2 - \left(1 - \frac{m^2}{q^2}\right) \ln\left(1 - \frac{m^2}{q^2}\right) + O(\varepsilon))\right] \qquad (4.26)
$$

In my thesis, I used the Mathematica implementation `MB.m` [102] to generate the expansions automatically. The way described above was invented by Smirnov, however in `MB.m` a related method is implemented [103] with is suited better for an computational approach.

[5] $\gamma_E \approx 0.57721$

Asymptotics in m_s and x

After the expansion in ε, it is in general not possible to calculate the integral analytically, except for the easiest cases. In Section 4.2.2 it was shown that the whole analytic structure of the master integrals is known, only the boundaries of the master integrals have to be calculated, whereby their position (in powers of m_s and x) is determined by the the homogeneous differential equations (Equation 4.11). Often the boundary is at m_s^0 and x^0, but some 7 non-planar master integrals only can be calculated because their boundary lies at some negative power of x. The asymptotics of small values for m_s and x (or $1-x$ respectively) was done with the help of the Mathematica package `MB.m` [102]. This limit is used to determine the boundaries of the differential equations (see Section 4.2.2) and serves as starting point for the numerical integration (see Section 4.3).

Toolkit for the Calculation of Mellin-Barnes Integrals

A Mellin-Barnes representation is generated by repeatedly applying Equation 4.14. The result is an n-fold integral, where n is the number of applications of Equation 4.14 and it is a good measure for the complexity of the integral. Usually one obtains 7- up to 13-fold integrals for Feynman diagrams with 6 or 7 internal lines. Normally the non-planar diagrams have much worse representations than the planar ones. After the expansion in ε and m_s, typically the highest remaining dimension are 4- up to 6-fold integrals. As it can been seen in the following sections, only 1-folds and the most 2-folds can be evaluated.

Barnes Lemmas Barnes lemmas are used to reduce high-order folds to 1- and 2- folds which can be calculated. They state that if a contour in the complex space divides left and right poles (see Section 4.2.3), then the following holds:
First Barnes lemma:

$$\frac{1}{2\pi i}\int_{-i\infty}^{+i\infty} dz\, \Gamma(\alpha+z)\Gamma(\beta+z)\Gamma(\gamma-z)\Gamma(\delta-z) = \frac{\Gamma(\alpha+\gamma)\Gamma(\alpha+\delta)\Gamma(\beta+\gamma)\Gamma(\beta+\delta)}{\Gamma(\alpha+\beta+\gamma+\delta)} \tag{4.27}$$

Second Barnes lemma:

$$\begin{aligned}\frac{1}{2\pi i}\int_{-i\infty}^{+i\infty} dz\, \frac{\Gamma(\alpha+z)\Gamma(\beta+z)\Gamma(\gamma+z)\Gamma(\delta-z)\Gamma(\zeta-z)}{\Gamma(\alpha+\beta+\gamma+\delta+\zeta+z)} = \\ \frac{\Gamma(\alpha+\delta)\Gamma(\alpha+\zeta)\Gamma(\beta+\delta)\Gamma(\beta+\zeta)\Gamma(\gamma+\delta)\Gamma(\gamma+\zeta)}{\Gamma(\alpha+\beta+\delta+\zeta)\Gamma(\alpha+\gamma+\delta+\zeta)\Gamma(\beta+\gamma+\delta+\zeta)}\end{aligned} \tag{4.28}$$

Both lemmas reduce the dimensionality of integrals by one. Through applying both lemmas repeatedly, it was possible in my PhD. thesis to reduce most integrals to 1- up to 4-fold integrals. In my PhD thesis I used the Mathematica package `barnesroutines.m` [97], which automatically looks for linear transformations of the integrand in order to apply Barnes Lemmas.

Calculation of 1- and 2-fold integrals

After using Barnes Lemmas, often only 1- up to 4-fold integrals remain. The following section gives tools for further simplification and the evaluation of these integrals.
The table stated below shows which class of n-fold integrals can be calculated directly, and which need further simplifications. 'Double arguments' means that in the arguments of the Γ-functions the coefficients before the variables are different from 1 or -1, for example $\Gamma(2\ z1 + z2)$. The solutions belonging to these integrals are often unknown and therefore not calculable analytically. Power dependence of an integral of a kinematic invariant can be seen, for example, in Equation 4.30.

	Double arguments	Exponential Dep.	Double Arg and Exp. Dep.
1-fold Int.	Numeric Integr. + PSLQ	XSummer	no general solution
2-fold Int.	`Quadprec` + PSLQ	XSummer2	no general solution
n-fold Int.	Using Barnes Lemmas and Γ identities		

XSummer and XSummer2 The analytic solutions of Feynman integrals often contain hypergeometric functions, which are defined through hypergeometric sums. These sums are power series, whereby the k-th coefficient is a rational function with the argument k. One example is the following hypergeometric function:

$$ {}_2F_1(a,b,c,x) = \sum_{k=0}^{\infty} \frac{\Gamma(k+a)\Gamma(k+b)\Gamma(c)}{\Gamma(a)\Gamma(b)\Gamma(k+c)} \frac{x^k}{k!} \tag{4.29} $$

Furthermore, polylogarithms or their generalization, the Nielsen polylogarithms [104] belong to the group of hypergeometrical functions.
In this work all appearing functions could be transformed to harmonic polylogarithms (HPL's) [105]. They are a generalization of the Nielsen polylogarithms and form a product algebra. They are defined through recursive integration over so-called weighting functions. The number of integrations determines the weight of the harmonic polylogarithm. The weighting functions are $f_1(x) = \frac{1}{1-x}$, $f_0(x) = \frac{1}{x}$, $f_{-1}(x) = \frac{1}{1+x}$. The associated HPL's with weight 1 are $H(1,x) = \int_0^x f_1(t)\ dt$, $H(0,x) = \log x$, $H(-1,x) = \int_0^x f_{-1}(t)\ dt$. HPL's with higher weights are defined recursively through $H(a_{k+1}, a_k, ..., a_1) = \int_0^x f_a(t) H(a_k, ..., a_1)\ dt$. The question why all appearing Feynman diagrams can be expressed trough harmonic polylogarithms stays unsolved.
The program XSummer permits the calculation of the most 1- and 2-fold integrals, through adding the residua. Only integrals which contain double arguments in the Γ-functions (like $\Gamma(2z_2)$) cannot be evaluated.
One example from my work is the following function:

$$ \int_{-i\infty}^{+i\infty} dz_1\, dz_2\, \frac{-2\varepsilon Y^{z_1} \Gamma(1-z_1)^2 \Gamma(2-z_1)\Gamma(-1+z_2)^2\Gamma(z_1)}{t^2} \tag{4.30} $$

As a result of the exponential dependence of the integrand on the kinematic variable Y^{z_4}, the integral can not be calculated numerically to a high precision (this would be necessary for the

PSLQ algorithm, see next section). Nevertheless the contour can be closed and the residua can be summed up. The result is:

$$\frac{\varepsilon Y(6H(0,0,1,-Y)+3H(1,-Y)(\pi^2+\log^2(Y))+\log(Y)(3\pi^2-6H(0,1,-Y))+\log^2(Y))}{3t^2}, \tag{4.31}$$

where H stands for harmonic polylogarithms. To work properly, the integrand has contain a kinematic variable which has a power dependence on one of the integration variable. In cases of integrands without this, the PSLQ algorithm can be used or an auxiliary parameter A^z is introduced, which is sent to 1 after resuming with XSummer. XSummer2 can calculate even 2-fold integrals.

PSLQ If the integrand does not have any exponential dependence on an integration variable, it can simply be integrated numerically along the imaginary axis. The number of obtained digits depends strongly on the dimensionality of the Feynman integral. 1-folds can be calculated without problems to 100 correct digits or more in a few minutes with the function MBintegrate from the package MB.m [102]. The calculation of 2- or 3-fold integrals was done with the program `Quadprec` [106]. Within one day it was possible to get 40 to 60 correct digits of a 2-fold (depends on the complexity of the integral). For 3-dimensional integrals three days were needed to get 15-20 digits.
Although a proof is missing, calculations show that the amplitude and the results of the master integrals are in generally simple and can be expressed through a few functions and certain numbers. In the case of top quark pair production these functions are the HPL's up to weight 4 and the numbers are $\zeta(2)$, $\zeta(2)\log(2)$, $\zeta(3)$, $\zeta(4)$[6]. The master integrals can contain additional functions, like in my case $\zeta(5)$ or $\zeta(2)\zeta(3)$, which cancel by calculating the amplitude.
Now all integrals of a master integral were calculated numerically to some precision, and one tries to find analytic coefficients a_i in front of the basis, in such a way that the numerical result matches the analytic result up to the given numbers of digits.

$$\text{Numerical result} = a_1 + a_2\zeta(2) + a_3\zeta(2)\cdot\log(2) + a_4\zeta(3) + a_5\zeta(4) + a_6\zeta(5) + a_7\zeta(2)\cdot\zeta(3) \tag{4.32}$$

The coefficients a_i can be determined with the help of the PSLQ algorithm [99], which converts the former numerical result in an analytic result. Although the PSLQ algorithm provides no proof for the correctness of the transformation, it is extremely unlikely that another set of small basis coefficients exist, which fulfill the equation up to the given precision. Moreover, the solution was always checked if it was stable under giving some more or less exact digits.

To demonstrate the proceeding on one example, the 2-fold integral

[6] $\zeta(a)$ is the Riemann Zeta-function $\zeta(a) = \sum_{n=1}^{\infty} \frac{1}{n^a}$.

$$\int\int dz_1 dz_2 \frac{-2\Gamma(-z_1)^2\Gamma(1+z_1)\Gamma(-z_2)\Gamma(-z_2+z_1)^2\Gamma(z_2-z_1)\Gamma(1+2z_1)\psi^{(0)}(1+z_1-z_2)}{\Gamma(1-z_1)\Gamma(1-z_2+z1)} \tag{4.33}$$

with the polygamma-function ψ, cannot be evaluated with XSummer, due to double arguments. With `Quadprec` it was possible to obtain a numerical result with 31 correct digits within few hours.

$$\text{Value}_{\text{numeric}} = 3.18219942067904236066900663153 84 \tag{4.34}$$

As Basis $\zeta(2)$, $\zeta(2)\cdot\log(2), \zeta(3)$, $\zeta(4)$, $\zeta(5)$, $\zeta(2)\cdot\zeta(3)$ was assumed.
The PSLQ algorithm gives the analytic result

$$\text{Value}_{\text{analytic}} = 10\cdot\zeta(2)\cdot\zeta(3) - 16\cdot\zeta(5) \tag{4.35}$$

A check of the results gives an agreement up to the claimed 31 digits.

$$\text{Value}_{\text{numeric}} - \text{Value}_{\text{analytic}} = 5\cdot 10^{-32} \tag{4.36}$$

Γ-functions identities If Barnes Lemmas do not provide results, it often is possible to transform the Mellin-Barnes integrals by hand and apply Barnes Lemmas afterwards. Typically simple transformation have been used like $\Gamma(z+1) = -\Gamma(z)\frac{\Gamma(1-z)}{\Gamma(-z)}$ or $\psi^{(m)}(z+1) = \psi^{(m)}(z) + (-1)^m\ m!\ z^{-(m+1)}$, where ψ is the polylogarithm function. Another trick which often worked was the splitting or merging from different MB integrals like in $\Gamma(z_1+z_2+1)/\Gamma(z_1+z_2) \to \Gamma(z_1+1)/\Gamma(z_1) + \Gamma(z_2+1)/\Gamma(z_2)$. Some additional transformations can be found with the Mathematica routine `FullSimplify`.

Further Methods

Especially the non-planar diagrams were difficult to calculate, various tricks had to be invented to find a representation which was calculable at all.

Change of Basis One possibility of avoiding the calculation of a difficult master integral is to replace a master integral by a new one and the cross section gets expressed through the new set of master integrals. The new master integral has to be related to the old one by partial integration. This method often had to be used if a master integral was difficult to calculate or generated spurious poles.

Change of the F and/or U Polynomial The representation of a MB integral is not unique. Through a change in the F- or U-polynomial (see Equation 4.20) different representations are generated. Especially for the non-planar diagrams it was necessary to try different representations to find one which could be calculated.

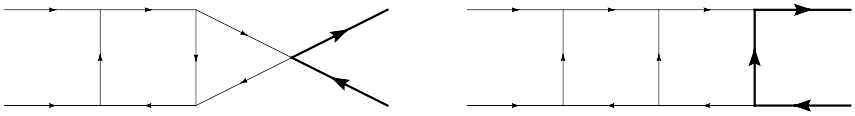

Figure 4.9.: Left: A master integral which has a difficult MB-representation. Right: An additional propagator is introduced with power α. The MB-representation gets expanded around $\alpha = 0$. This may simplify the calculation considerably.

Introduction of an Additional Propagator Another trick is the introduction of additional propagators. For example, instead of generating a representation of a 6-liner (see Figure 4.9), a representation of a 7-liner is calculated with an additional propagator with exponent α. Afterwards this representation gets expanded around $\alpha = 0$.

4.3. The Middle Range

4.3.1. Numerical Evaluation of the Differential Equations

The analytic expansion of the amplitude up to m_s^{10} (see Equation 4.12) does not give the correct result when β is slightly smaller than 1. Therefore, the differential equations for the master integrals are solved numerically and the result is plugged into the amplitude. The right selection of the numeric integration algorithm makes the difference between success and failure. A fast implementation is as important as a high precision result and reliable error control.

As seen in Section 4.2.2 the whole system can be written in block-diagonal form of 1263 (or 595 in the $q\overline{q}$-channel respectively) inhomogeneous linear differential equations.

$$\begin{aligned} \frac{d}{dm_s}\vec{Z}(x,m_s) &= J^{m_s}(x,m_s)\ \vec{Z}(x,m_s) \\ \frac{d}{dx}\vec{Z}(x,m_s) &= J^{x}(x,m_s)\ \vec{Z}(x,m_s) \end{aligned} \tag{4.37}$$

where $\vec{Z}$ is a vector with 595 (1263) entries and J is a quadratic, lower triangular block-matrix.

Singularities of the Differential Equations

A numeric integration has to fight with two different sources of singularities. First, the physical singularities. These appear at the s-, t-, and u-channel thresholds (i.e. $\beta = 0$, $x = 0$ and $x = 1$ respectively) and in collinear limit at $\beta = 1$. Second, unphysical 'spurious' singularities which appear in the differential equations and can in principle be eliminated by a change of master integrals. In practice, however, no prescription is available. For an overview of the singularities in the gluon fusion channel see Table 4.1. There are 37 additional singularities, which do not slice the phase space. Six entries (see Figure 4.10) do only touch the phase space at the following points $\beta = \sqrt{5} - 2$, $\beta = 1/2$, $\beta = (\sqrt{3} - 1)/2$. Neverthless, they can strengthen the singularities

Jacobian singularity	comment
$\beta = 0$	s-channel threshold
$\beta = 1$	collinear singularity
$\beta = \sqrt{\sqrt{2} - 1}$	
$x = 0$	t-channel threshold
$x = 1$	u-channel threshold
$x = 1/2$	perpendicular scattering
$x = (1 \pm \beta)/2$	forward/backward scattering
$x = (-1 + \beta^2)^2/(2(1 + \beta^2))$	no symmetric counterpart
$x = (2(-1 + \beta^2))/(-5 + \beta^2)$	no symmetric counterpart
$x = 1/2 \pm \beta^2/2$	slices phase space
$x = 1/2 \pm (-1/2 + \beta^2)$	slices phase space
$x = 1/2 \pm \sqrt{-1 + 2\beta^2}/2$	slices phase space
$x = 1/2 \pm (1 + 22\beta^2 - 7\beta^4)/(2(3 + \beta^2)^2)$	touching phase space
$x = 1/2 \pm (1 - \beta^2 - \sqrt{5 - 4\beta^2}/2)$	touching phase space
$x = 1/2 \pm (-3/2 + \beta^2 + (1 - \beta^2)\sqrt{2 - \beta^2})$	touching phase space

Table 4.1.: Singularities of the Jacobian, J^{m_s} and J^x, of the system of differential equations 4.37, which slice the phase space. Additionally, the table indicates the presence of a branching point at a given singularity (a blank entry denotes a regular point of the solution).

close to these points. Three singularities are absent in only one half of the phase space. Here the TU symmetric masters have been chosen differently, so that only one has a singularity in the differential equations. The numeric approach to both kinds of singularities leads to large numeric cancellations and hence reduces the precision and increases the runtime of the routines.

The phase space points at $\beta = 0.5$ and $\beta = 0.7875$ can not be calculated due to unphysical singularities inside the system of differential equations. These points are therefore determined by interpolation. For the Gauss-Kronrod phase space, the points at $\beta = 0.9875$ and $\beta = 0.999$ with the highest value in x extrapolation have to be used. This is due to the physical singularity at $x = 1$.

Numerical Solution

Several different integration methods can be found in the literature. Demanding a high precision result and assuming smoothness of the master integrals a variable coefficient multistep method is expected to be the most efficient [93], [107], [108]. The algorithm uses inter- and extrapolation. The smoothness of the master integrals guarantees a fast convergence and therefore a brief runtime. Another requirement with regard to the algorithm is its ability to work with complex functions. An alternative way would be to split the complex master integrals into two

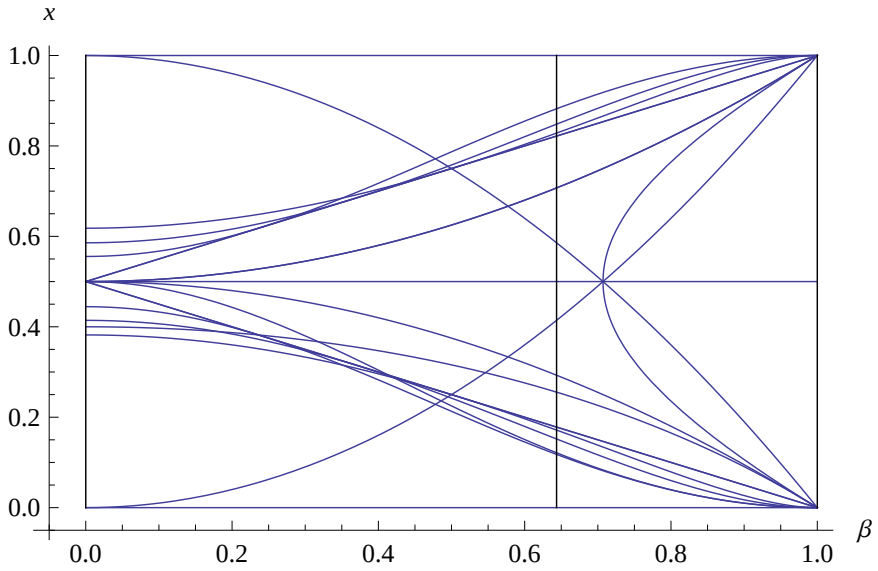

Figure 4.10.: Graphical representation of the singularities of the system of differential equations in β and x in the gluon fusion channel, as stated in Table 4.1. Both systems have exactly the same singularities. Those not touching the phase space are excluded.

component real functions. Yet, this procedure would double the size of the Jacobian, which increases the runtime, and would have further disadvantages as far as error control is concerned. Although the majority of algorithms are only for real arguments, one of the most advanced packages `ODEPACK` [109], containing the multi-step method, is available for complex arguments.

While for high-precision applications Bulirsch-Stoer dominates as integration routine, for moderate precision, adaptive-step-size Runge-Kutta methods prevail. The preferred areas of applications of the multi-step algorithm are high-precision solution of very smooth equations with very complicated right-hand sides [108], while is the case for the double virtual contributions. The differential equation $y'(x) = f(x, y(x))$ can be written as

$$y(x_{n+1}) = y(x_n) + \int_{x_n}^{x_{n+1}} dx\, f(x_n, y(x_n)) \tag{4.38}$$

In single step algorithms like Runge-Kutta, the value of $y(x_{n+1})$ only depends on $y(x_n)$. In the multisteps method $f(x, y)$ gets approximated by a polynomial of order n (in our implementation up to order 12), where the n coefficients of the polynomial are determined by demanding that it passes through the previous n points $(x_i, y(x_i))$ [108].

From the singularities given in Table 4.1 it is clear that an integration along the real axis should be avoided. An integration along a path in the complex plane (see Figure 4.11) has two advantages. Firstly, it avoids the singularities which lie on the real axis. Secondly, the integration can be done with different elliptic contours and the difference yields a simple estimate for the global

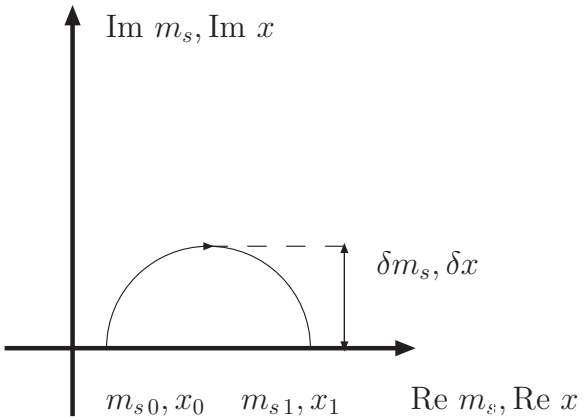

Figure 4.11.: An integration over the variable m_s or x in the complex plane. The user specified eccentricities δm_s and δx provide a global error estimation. Figure taken from [93].

error.

The numerical integration was done in two independent steps. Firstly, the integration in m_s was accomplished, secondly, the integration in x, in order to derive the desired phase space point. The single point $(m_s, x) = (0.0005, 0.45)$, from which all the other grid point are calculated (Figure 4.12) is taken as boundary. m_s has to be small to increase the precision of the high-energy limit boundaries. The best convergence would be for the point $x = 0.5$, but due to a singularity in the system of differential equations, it cannot be used. For no master integral the error exceeds 10^{-20}.

The gluon fusion channel turned out to be much more difficult than the quark annihilation channel due to a larger system of differential equations and large cancellations because of abundant singularities. Thus, double quad precision (64 digits) (`QD Library` [110]) had to be implemented into the ordinary differential equation solver. Since this increased the runtime significantly (to around a day per point for points close to the singularities), we developed other methods in the region of small β (see Section 4.4).

Combining the `Fortran`-package `ODEPACK` [109] and the quad-double `QD Library` [110], the system of differential Equations 4.37 can be solved numerically and provides high precision results of the master integrals for a wide phase space region (in the gluon channel, values for β up to 0.06 can be achieved). The calculation of the master integral to order 10 in m_s thereby provides precise values for the boundaries of the master integrals in the region where $\beta \approx 1$ ($m_s \approx 0$).

Once all 1263 integrals have been calculated this way, the result is plugged into the amplitude, which is evaluated at the corresponding phase space point.

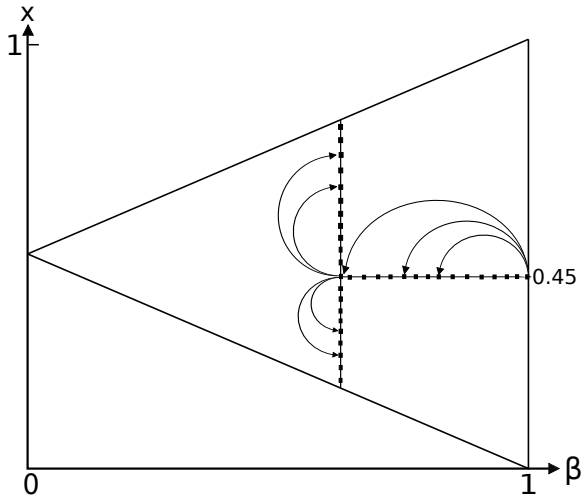

Figure 4.12.: From the starting point $(m_s, x) = (0.0005, 0.45)$ all other points are obtained by using the numeric differential equations.

Efficiency and Stability

In the $q\overline{q}$ annihilation channel the computation of a single phase space point took around 15 minutes [93]. The increase of the running time in the gluon fusion channel has three causes:

- The Jacobian is a factor four bigger, the data size a factor 25
- and the gluon fusion channel contains considerably more singularities
- Instead of double (16 digits) or quadruple (32 digits) double-quad precision (64 digits) is used

To increase efficiency and stability, the value for x and m_s is hard-coded, when doing the m_s and x integration respectively. More specifically, from the starting point $(m_s, x) = (0.0005, 0.45)$ all m_s-integrations to $(\beta, x) = (0.4500, 0.45), (0.4625, 0.45), ..., (0.9875, 0.45), (0.999, 0.45)$ are accomplished, where x is hard-coded as 0.45 in the Jacobian. Afterwards 42 different Jacobians are calculated, where m_s (i.e. β) is hard-coded (see Figure 4.12). The compilation for each Jacobian needs 12 hours (Intel Fortran compiler without optimizations).

The multi-step method requires a maximal local error δ_l as input, that means an error which is not allowed to be exceeded at any step. The global error δ_g scales like $\delta_g = \sqrt{n}\delta_l$, where n is the number of executed steps. A typical number of steps is 5000 for the m_s evaluation and 500 for the x evaluation, but they strongly depend on the phase space point. The number of necessary steps in the x evolution is usually lower, because the distance is smaller and the starting point is far from any singularity. Typical values of the requested local error δ_l are 10^{-18} for the m_s and 10^{-16} for the x. Consequentially, the final global error δ_g should not exceed 10^{-15}.

4.3.2. Gauss-Kronrod Quadrature

For each value of the 36 different β values within the middle range, 42 points are calculated (see Figure 4.1) with the numeric evaluation of the differential equations.
The method of estimating the integral over x (along a phase space cut with constant β) on basis of these 42 calculated points is called numeric quadrature and has been long known in the literature. The integration is approximated transforming the integral to a weighted sum of function values at specific points.

$$\int_{-1}^{1} f(x)\,dx \sim \sum_{i=1}^{N} w_i\, f(x_i) \tag{4.39}$$

By convention, the domain of integration goes from -1 to 1. To produce acceptable results the integral has to be well approximated by a polynomial, that means it needs to be smooth and should not contain singularities.
The most widely known, however outdated, method is the Simpson rule. Methods, which are still in use and are based on equally divided abscissas are the *extended Midpoint rule* where the integral is approximated by

$$\int_{x_1}^{x_N} f(x)dx \sim h[\frac{1}{3}f(x_1) + \frac{4}{3}f(x_2) + ... + \frac{4}{3}f(x_{N-1}) + \frac{1}{3}f(x_N)] + O(\frac{1}{N^4}), \tag{4.40}$$

and the *extended trapezoidal rule* [108]:

$$\int_{x_1}^{x_N} f(x)dx \sim h[f(x_{\frac{3}{2}}) + f(x_{\frac{5}{2}}) + ... + f(x_{\frac{2N-1}{2}})] + O(\frac{1}{N^2}), \tag{4.41}$$

In general, these methods calculate an integral correctly if it is a polynomial of order $N-1$.
Gaussian quadrature rules are constructed in such a way, that they allow to obtain an exact result for polynomials up to the order $2\,N-1$. The quadrature rule fixes not only the integration weights w_i, but also the integration points x_i. To derive an error approximation, it is common to perform a new Gaussian quadrature with only half of the points and use the difference of the two results as an error estimation. Unfortunately, the abscissa points of the two quadratures have no points in common, so $N + \frac{1}{2}N$ calculations have to be carried out to get a result to the order $2\,N-1$ and a reliable error approximation.

There are various extensions of the Gaussian quadrature. A common one requires some nodes to be included in the set of abscissas and the question arises of how to calculate the weights w_i and remaining abscissas x_i. The Gauss-Radau quadrature is an algorithm to include one endpoint of the integration domain, Gauss-Lobatto, in contrast, includes both endpoints as nodes.

The Gauss-Kronrod (GK) quadrature is an extension of the Gaussian quadrature where the additional points are chosen in such a way that the error can be estimated by re-using the already computed points. After a Gaussian quadrature is done with n points additional N points are added, which yields $2N+n$ degrees of freedom ($n+N$ weights and N values for

the abscissas). A new Gaussian quadrature is performed with $n + N$ points (by re-using the result for the n already calculated points). This gives an exact results for polynomials up to order $2N + n - 1$. The difference between the result with n and $N + n$ points is used for error estimation. In his work Kronrod proved, that in case of $N = n + 1$ an optimal extension can be found for the Gauss-Legendre quadrature. Popular values for n are $10, 21, 43, 87, 175, ...$ Therefore the Gauss-Kronrod quadrature with $2N + 1$ points gives exact results for polynomials up to order $3N - 1$ and a reliable error approximation by using the difference of the Gauss-Kronrod quadrature with $2N + 1$ points and the Gauss quadrature with N points.

Error Estimation for the Middle Range

The obtained error in the middle range is small and in general it is much better for the quark annihilation channel than for the gluon fusion channel. The total error is composed from the error:

- at the starting points $(m_s, x) = (0.0005, 0.45)$ and $(m_s, x) = (0.0005, 0.35)$. It is below 10^{-20} for each master integral. This error propagates with the differential equations and can be reduced by choosing a starting point with a smaller value for m_s.
- from the numeric integration. It is estimated to $\sim 10^{-10}$, by using different contours in the complex plane by using different starting points to the desired point.
- from the Gauss-Kronrod integration. It is usually better than $\sim 10^{-7}$, but for large values of $\beta \geq 0.9000$ it becomes larger, since the cross section is more complicated as can be seen from the Figures 4.17, 4.18 and 4.19.

This overall error is determined by using two different starting points (in our case $(m_s, x) = (0.0005, 0.45)$ and $(m_s, x) = (0.0005, 0.35)$) and comparing the difference of the total cross section. Only for a few points the value is worse than 10^{-6}, see Figure 4.13. Moreover, the contribution of the double virtual part $\hat{\sigma}^{VV}_{gg\to t\bar{t}}$ to the total partonic cross section $\hat{\sigma}_{gg\to t\bar{t}}$ is only around $\sim 1\% - 10\%$ in the middle range (see Figure 4.2), so that the total error decreases further. Another method to estimate the error is to compare the results obtained by the methods of the middle range and the result obtained by the methods of the low-energy limit (see Section 4.4) at the common points from $\beta = 0.1000$ to $\beta = 0.1500$. The absolute difference is 10^{-4} (10^{-6} relative difference) and the source of the error is probably from the low-energy limit. Keeping in mind that the uncertainties in the PDFs and the luminosity will not be better than 1%, the relative error of 10^{-6} can be neglected.

4.4. The Low-Energy Limit

Figure 4.2 demonstrates, that the relative contribution of the double virtual correction is large at very low and at very high values for β. At low β values the Coulomb singularities dominate, which are encoded in the double virtual corrections and at high β values the contributions of the other parts, like soft gluon radiations, are small.

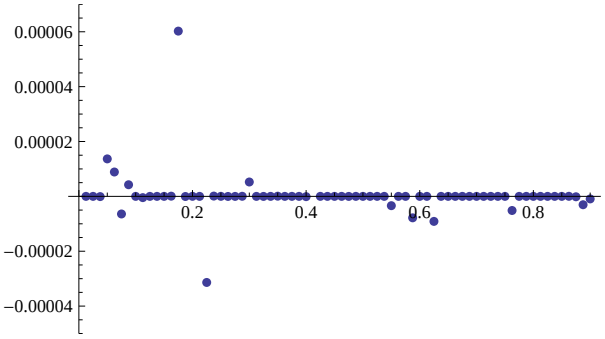

Figure 4.13.: Absolute error from comparing the total cross sections derived from two different starting points. Its almost always smaller than 10^{-6}. The relative error is only around a factor 10^{-8}.

The absolute error of the double virtual contribution thus needs to be small in these two regions. Moreover, the numerical integration faces problems in this part of the phase space region, due to the physical singularity at $\beta = 0$ and unphysical singularities inherent to the system of differential equations (see Section 4.3).
Hence a new method had to be developed for the low-energy region of the phase space (see Figure 4.4).

4.4.1. Differential Equations

We expand the differential equations around the threshold $\beta = 0$ instead of the high-energy limit $\beta = 1$. This suites much better this phase space region. The expansion is done as a parametrization around t, which is proportional to β. $t_1(t) = \frac{1}{2} - 1/4t$ and $t_2(t) = \frac{1}{2} + 1/4t$ divide the upper and the lower half of the phase space (see Figure 4.14). Again, the differential equations determine the whole analytic structure of the master integrals as function of t.

$$\frac{d}{dt}\vec{Z}(t) = J^t(t)\ \vec{Z}(t), \tag{4.42}$$

$\vec{Z}(t)$ is the vector of the Laurent expanded master integrals with 1263 (see Equation 4.8) entries and J^t is a quadratic, lower triangular block-matrix. For the master integrals a power-log ansatz

$$\vec{Z}_i(t) = \sum_{j=-3}^{j=N} \sum_{k=0}^{k=4} c(i,j,k)\ t^j\ \log(t)^k \tag{4.43}$$

is used to solve the system of differential equations. Equations 4.42 result in relations between the coefficients $c(i,j,k)$. Only the coefficient of the boundary remains unsolved for each master. Surprisingly, the boundaries do not only appear in integer and half-integer order in t, but one in $t^{-\frac{5}{4}}$ as well. The lowest order was t^{-3}. The boundaries are determined by matching in a phase space area, where the low-energy limit and the numerical integration (see Section 4.3) are

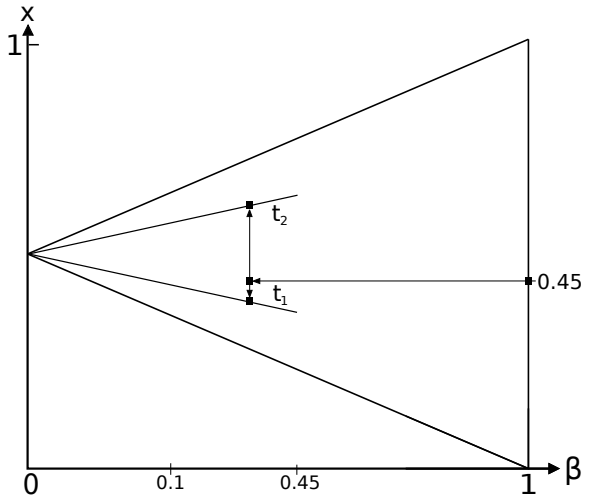

Figure 4.14.: The master integrals are computed using the method of differential equations around the lines t_1 and t_2 and depend only on the boundaries. These are determined by matching the master integrals to the result obtained by using the numerical differential equations and the high energy limit.

valid. In my work I took $\beta = 0.1$ and $\beta = 0.11$ to determine the boundary coefficients through matching (see Figure 4.14).
This gives the result for the master integrals along the two lines t_1 and t_2. It was planned to do the same with 42 lines and then use the Gauss-Kronrod integration (like in Section 4.3.2) to integrate along the x-variable. However it could not be accomplished since that the lines close to the middle line ($x = 0.5$ is a singularity of the system of differential equations) diverge. Therefore a completely different method had to be invented.

4.4.2. Taylor Expansion

At each of the desired 45 values for $\beta = (0.0125, ..., 0.4500)$ in the $q\overline{q}$-channel and at the 13 values for $\beta = (0.0125, ..., 0.1625)$ in the gluon fusion channel in the low-energy regime, the two points lying on t_1 and t_2 are known from the differential equations 4.42 in t and the matching condition (see Figure 4.14). Around these two points a Taylor expansion is performed in x direction.
In order to obtain an expression for the amplitude in dependence of a small expansion parameter d, one has to apply a Taylor expansion to two parts. Firstly, the amplitude is expanded around the two points in the parameter the d. This is done by simply replacing x_0 by $x_0 + d$ in the amplitude and by expanding around small values for d. This step is repeated independently for all of the desired values for β (see Figure 4.15).
Secondly, the derivatives of the master integrals in x direction are expanded in the small parameter d as well, after replacing x_0 by $x_0 + d$. Putting in a polynomial ansatz for the master integrals in d, and knowing the *boundary result* at $d = 0$ from the matching condition (Section

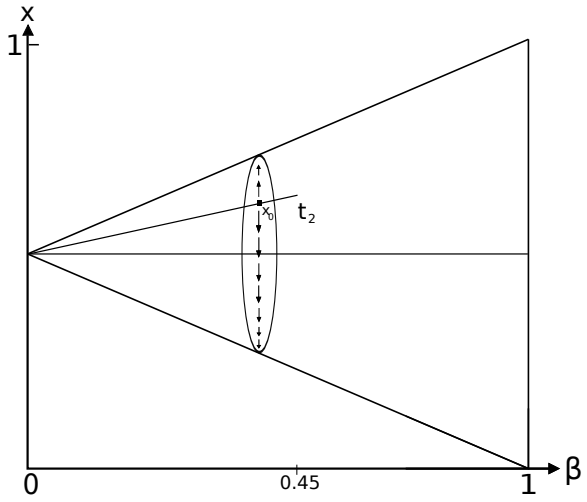

Figure 4.15.: Taylor expansion around the point x_0 in the x direction.

4.4.1) this system of equations can be solved. As a result one obtains the expansion of the master integrals in the small parameter d around the point (β, x_0). This expansion is valid up to the convergence radius is reached, which is a priori unknown.
Plugging the master integrals into the amplitude yields the amplitude as a function of d. This amplitude can then be integrated over x from $-\frac{1}{4}\beta$ to $\frac{3}{4}\beta$ (or $-\frac{3}{4}\beta$ to $\frac{1}{4}\beta$ for the upper point), to obtain the value of the partonic cross section at the given value for β. The Taylor expansion around both points is used for error control by comparing the difference of both results.

Error estimation for the low-energy limit

The low-energy limit delivers excellent results in quark annihilation channel till $\beta \sim 0.45$, where it breaks down by running close to a singularity placed at $\beta = 0.5$. In the gluon fusion channel the results are only valid till $\beta \sim 0.15$.
The error in the low-energy region comes from four sources:

- Matching error, arising from numerical integration to different phase space points ($\sim 10^{-13}$ $q\bar{q}$-channel and $\sim 10^{-8}$ $g\bar{g}$-channel)
- Finite order in t of the ansatz Equation 4.43 ($\sim 10^{-15}$)
- Taylor expansion around x_0 (limited convergence radius) and ambiguity at which order the Taylor series is cut ($\sim 10^{-12}$ $q\bar{q}$-channel and $\sim 10^{-5}$ $g\bar{g}$-channel) The Taylor series was used to determine the values at the Gauss-Kronrod points.
- The relative error from Gauss-Kronrod integration $\leq 10^{-6}$ for the first ($\beta = 0.0125$ and $\beta = 0.025$) and much smaller for the following points

4.5. Results

4.5.1. Renormalization Procedure

The coupling constant renormalization is performed in the $\overline{\text{MS}}$ scheme with n_l massless and n_h massive flavors.

$$\alpha_s^{\text{bar}} = (4\pi)^{-\epsilon} e^{\epsilon\gamma_{\text{E}}} \alpha_s \left[1 - \left(\frac{\alpha_s}{2\pi}\right) \frac{\beta_0}{\epsilon} + \left(\frac{\alpha_s}{2\pi}\right)^2 \left(\frac{\beta_0^2}{\epsilon^2} - \frac{1}{2}\frac{\beta_1}{\epsilon} \right) + \mathcal{O}(\alpha_s^3) \right], \tag{4.44}$$

β_0 and β_1 are the both first terms of the QCD β-function. The strong coupling renormalization is known up to four-loop accuracy [111, 112]
The mass m of the top quark is taken to be the pole mass and the necessary constants for the mass and on-shell field renormalization is given at 3-loop accuracy in [113, 114, 115]. The renormalization constants Z_2 and Z_3 for the light quarks and gluons do not disappear, due to closed top quark loops and are explicitly given in [49, 48].
In perturbative quantum field theory the amplitude $|\mathcal{M}\rangle$ for the process $gg \to t\bar{t}$ can be expanded in terms of the strong coupling constant α_s.

$$|\mathcal{M}\rangle = 4\pi\alpha_s [\, |\mathcal{M}^{(0)}\rangle + \left(\frac{\alpha_s}{2\pi}\right) |\mathcal{M}^{(1)}\rangle + \left(\frac{\alpha_s}{2\pi}\right)^2 |\mathcal{M}^{(2)}\rangle + \mathcal{O}(\alpha_s^3) \,] \tag{4.45}$$

The squared amplitude gets averaged over all spins and colors in the initial and the final state:

$$\mathcal{A}(\varepsilon, m_s, x) = \frac{1}{(d-2)^2} \sum_{spin} \frac{1}{(N_c^2-1)^2} \sum_{color} |\mathcal{M}\rangle^2 \tag{4.46}$$

The perturbative expansion of bare squared amplitude $\mathcal{A}(\varepsilon, m_s, x)$ is presented as:

$$\mathcal{A}(\varepsilon, m_s, x) = 16\pi^2\alpha_s^2 [\mathcal{A}^{(0)} + \left(\frac{\alpha_s}{2\pi}\right) \mathcal{A}^{(1)} + \left(\frac{\alpha_s}{2\pi}\right)^2 \mathcal{A}^{(2)} + \mathcal{O}(\alpha_s^3) \,] \tag{4.47}$$

The perturbative coefficients of $\mathcal{A}(\varepsilon, m_s, x)$ can be expressed through the coefficients of the amplitude $\mathcal{M}$ via:

$$\mathcal{A}^{(0)} = \langle \mathcal{M}^{(0)} | \mathcal{M}^{(0)} \rangle \tag{4.48}$$

$$\mathcal{A}^{(1)} = \langle \mathcal{M}^{(1)} | \mathcal{M}^{(0)} \rangle + \langle \mathcal{M}^{(0)} | \mathcal{M}^{(1)} \rangle \tag{4.49}$$

$$\mathcal{A}^{(2)} = \langle \mathcal{M}^{(1)} | \mathcal{M}^{(1)} \rangle + \langle \mathcal{M}^{(0)} | \mathcal{M}^{(2)} \rangle + \langle \mathcal{M}^{(2)} | \mathcal{M}^{(0)} \rangle \tag{4.50}$$

The renormalized term $\mathcal{A}^{(2)}_{\text{ren}}$ gets additional contributions from mass renormalization of $\mathcal{A}^{(0)}$ and $\mathcal{A}^{(1)}$ and from the multiplication of these terms with the renormalization constants Z_2, Z_3 and Z_{α_s} given in [49, 48].
The correctness of our renormalization procedure is checked by comparison with available incomplete results from the literature. Moreover, it is well-known from NRQCD, that the highest negative order of β is -2. The bare squared amplitude had poles in β down to order -3, but these cancel exactly with the mass renormalized diagrams pictured on the left hand side of Figure 4.16.

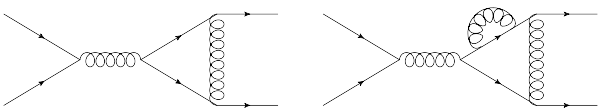

Figure 4.16.: Left: One-loop diagram, which has poles down to β^{-1}. Its mass renormalization contains poles of β^{-3}. Right: These poles are canceled by the β^{-3} poles of the two-loop diagram on the right hand side.

4.5.2. Result for the Phase Space Point $(m_s, x) = (0.2, 0.45)$

The renormalized result of the phase space point $(m_s, x) = (0.2, 0.45)$ of the double virtual corrections in the gg-channel is given in Table 4.2. The letter A to I describe the different color coefficients, n_l is the numer of light quarks, nh is the number of heavy quarks:

$$\mathcal{A}_{gg}^{(0,2)} = 2\mathrm{Re}\,\langle\mathcal{M}^{(0)}|\mathcal{M}^{(2)}\rangle = (N^2-1)\Bigg(N^3A + NB + \frac{1}{N}C + \frac{1}{N^3}D + N^2 n_l E_l + N^2 n_h E_h \tag{4.51}$$

$$+ n_l F_l + n_h F_h + \frac{n_l}{N^2}G_l + \frac{n_h}{N^2}G_h + N {n_l}^2 H_l + N n_l n_h H_{lh} + N {n_h}^2 H_h + \frac{{n_l}^2}{N} I_l + \frac{n_l n_h}{N} I_{lh} + \frac{{n_h}^2}{N} I_h\Bigg),$$

In the gluon fusion channel only the ε-poles [32] and the leading color coefficient is known analytically [58] and given in Table 4.2. We agree up to all given 5 digits of the poles and up to all given 10 digits in the leading color coefficient.
In the quark annihilation channel the ε-poles [32], the leading color coefficient [116] and the fermionic contributions [55] are known analytically and given in Table 4.2. We agree up to all given 5 digits of the poles and up to all given 10 digits in the leading color coefficient as can be seen in Table 4.3.

4.5.3. Results for the double virtual cross section for both channels

Our results of the double virtual part in both channels can be found as attachment to our papers.They are given in table-form in dependence of β for the total cross section and in dependence of β and x for the differential cross sections.

In the following plots of the renormalized differential and total cross section $\mathrm{d}\sigma_{gg}^{\mathrm{VV}}$ are presented. Figure 4.17 shows the the bosonic contributions of $\mathrm{d}\sigma_{gg}^{\mathrm{VV}}$, where the color coefficients are defined as in Equation 4.51. The Figures 4.18 and 4.19 show the single and double fermionic part. The bosonic, single- and double fermionic part of the renomalized total cross section are plotted in 4.20.

4.6. Checks

No second independent calculation of the double virtual cross section was performed, therefore thorough checks had to be implemented to guarantee the correctness of the obtained results.

	ϵ^{-4}	ϵ^{-3}	ϵ^{-2}	ϵ^{-1}	ϵ^{0}
A_{LC}	10.74942557	18.69389337	-156.8237244	262.1482588	12.72180680
A	10.74942557	18.69389337	-156.8237244	262.1482588	12.72180680
B	-21.28599123	-55.99039551	-235.0412564	1459.833288	-509.6019155
C		-6.199051597	-68.70297402	-268.1060373	804.0981895
D			94.08660818	-130.9619794	-283.3496755
E_l		-12.54099650	18.20646589	27.95708293	-112.6060988
E_h			0.012907497	11.79259573	-47.68412574
F_l		24.83365643	-26.60868620	-50.75380859	125.0537955
F_h			0.0	-23.32918072	132.5618962
G_l			3.099525798	67.04300456	-214.1081462
G_h				0.0	-179.3374874
H_l			2.388761238	-5.452031425	3.632861953
H_{lh}				-0.004302499	-3.945712447
H_h					0.00439856
I_l			-4.730220272	10.81032548	-7.182940516
I_{lh}				0.0	7.780900470
I_h					0.0
A^{Poles}	10.749	18.694	−156.82	262.15	
B^{Poles}	−21.286	−55.990	−235.04	1459.8	
C^{Poles}		−6.1991	−68.703	−268.11	
D^{Poles}			94.087	−130.96	
E_l^{Poles}		−12.541	18.207	27.957	
E_h^{Poles}			0.012908	11.793	
F_l^{Poles}		24.834	−26.609	−50.754	
F_h^{Poles}			0.0	−23.329	
G_l^{Poles}			3.0995	67.043	
G_h^{Poles}				0.0	
H_l^{Poles}			2.3888	−5.4520	
H_{lh}^{Poles}				−0.0043025	
H_h^{Poles}					
I_l^{Poles}			−4.7302	10.810	
I_{lh}^{Poles}				0.0	
I_h^{Poles}					

Table 4.2.: Values of the color coefficients of the two-loop gluon fusion amplitude at the point $m_s = 0.2$, $x = 0.45$ and $\mu^2/s = 1/5$ rounded at 10 digits precision (the given digits are unaffected by numerical uncertainties). A_{LC} is the leading color contribution calculated in [58], the values for X^{Poles} were calculated in [32].

	ϵ^{-4}	ϵ^{-3}	ϵ^{-2}	ϵ^{-1}	ϵ^{0}
A	0.22625	1.391733154	-2.298174307	-4.145752449	17.37136599
B	-0.4525	-1.323646320	8.507455541	6.035611156	-35.12861106
C	0.22625	-0.06808683395	-18.00716652	6.302454931	3.524044913
D_l		-0.22625	0.2605057339	-0.7250180282	-1.935417247
D_h			0.5623350684	0.1045606449	-1.704747998
E_l		0.22625	-0.3323207300	7.904121951	2.848697837
E_h			-0.5623350684	4.528240788	12.73232424
F_l					-1.984228442
F_{lh}					-2.442562819
F_h					-0.07924540546

Table 4.3.: Values of the color coefficients of the two-loop amplitude at the point $m_s = 0.2$, $x = 0.45$ rounded at 10 digits precision (the given digits are unaffected by numerical uncertainties).

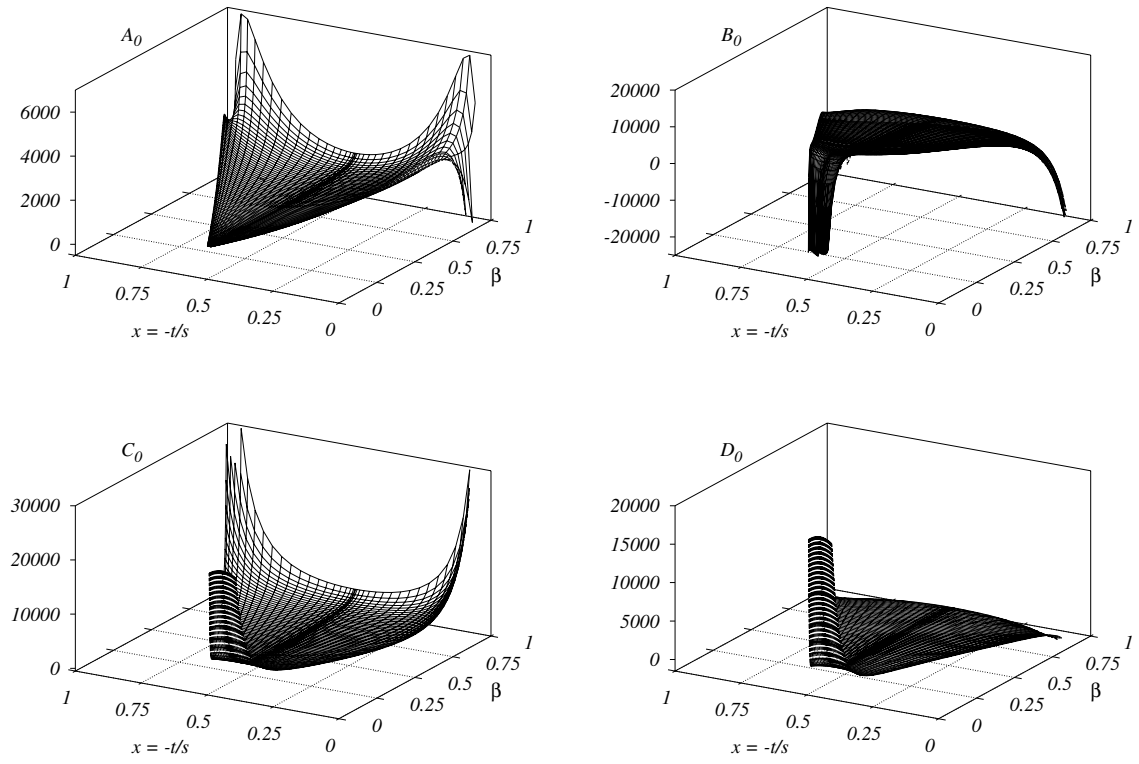

Figure 4.17.: Result of the different color factors of the finite part of the renormalized, differential double virtual cross section $\mathrm{d}\sigma_{gg}^{\mathrm{VV}}$.

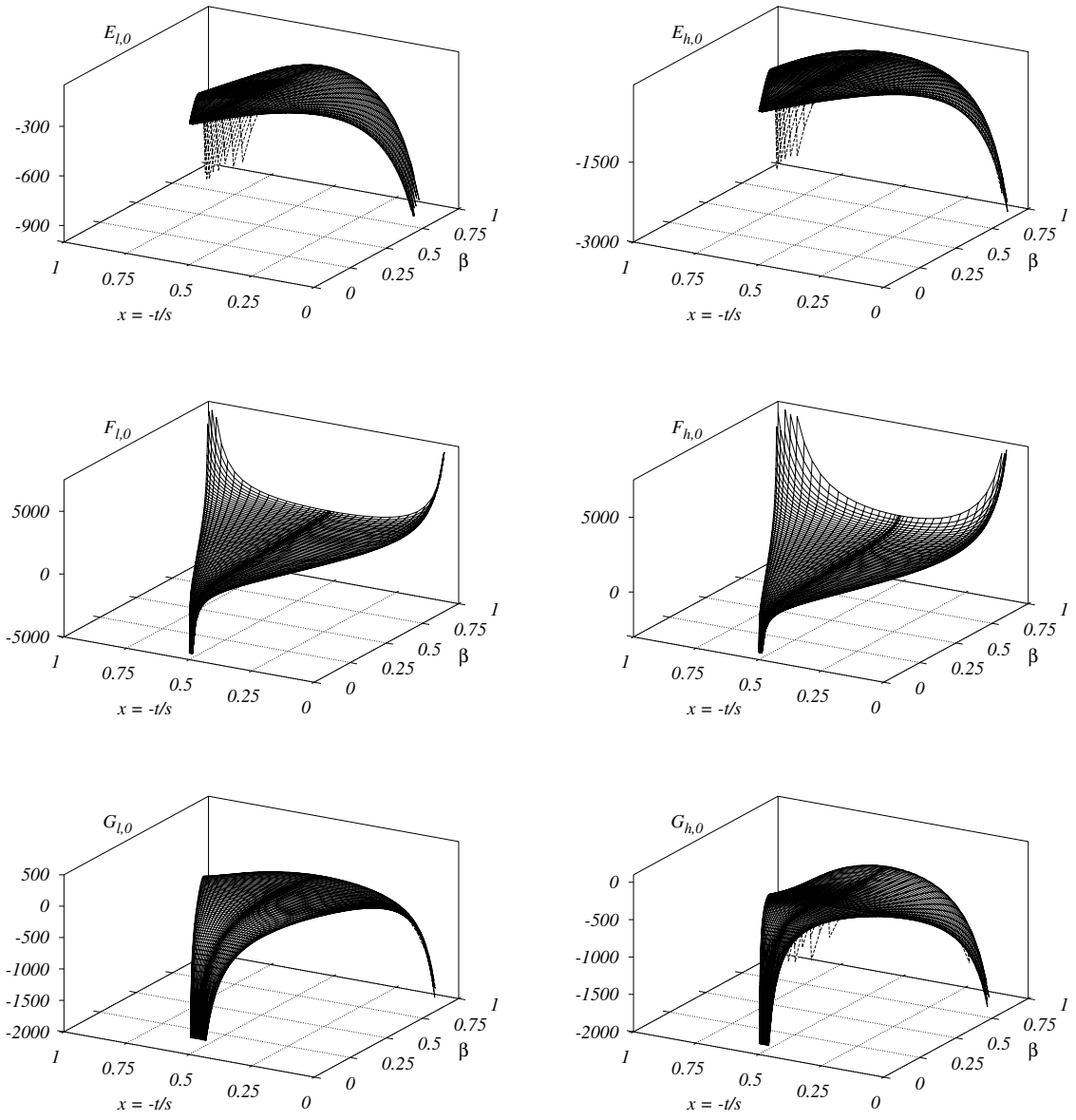

Figure 4.18.: Result of the different color factors of the finite part of the renormalized, differential fermionic cross section $\mathrm{d}\sigma_{gg}^{\mathrm{VV}}$.

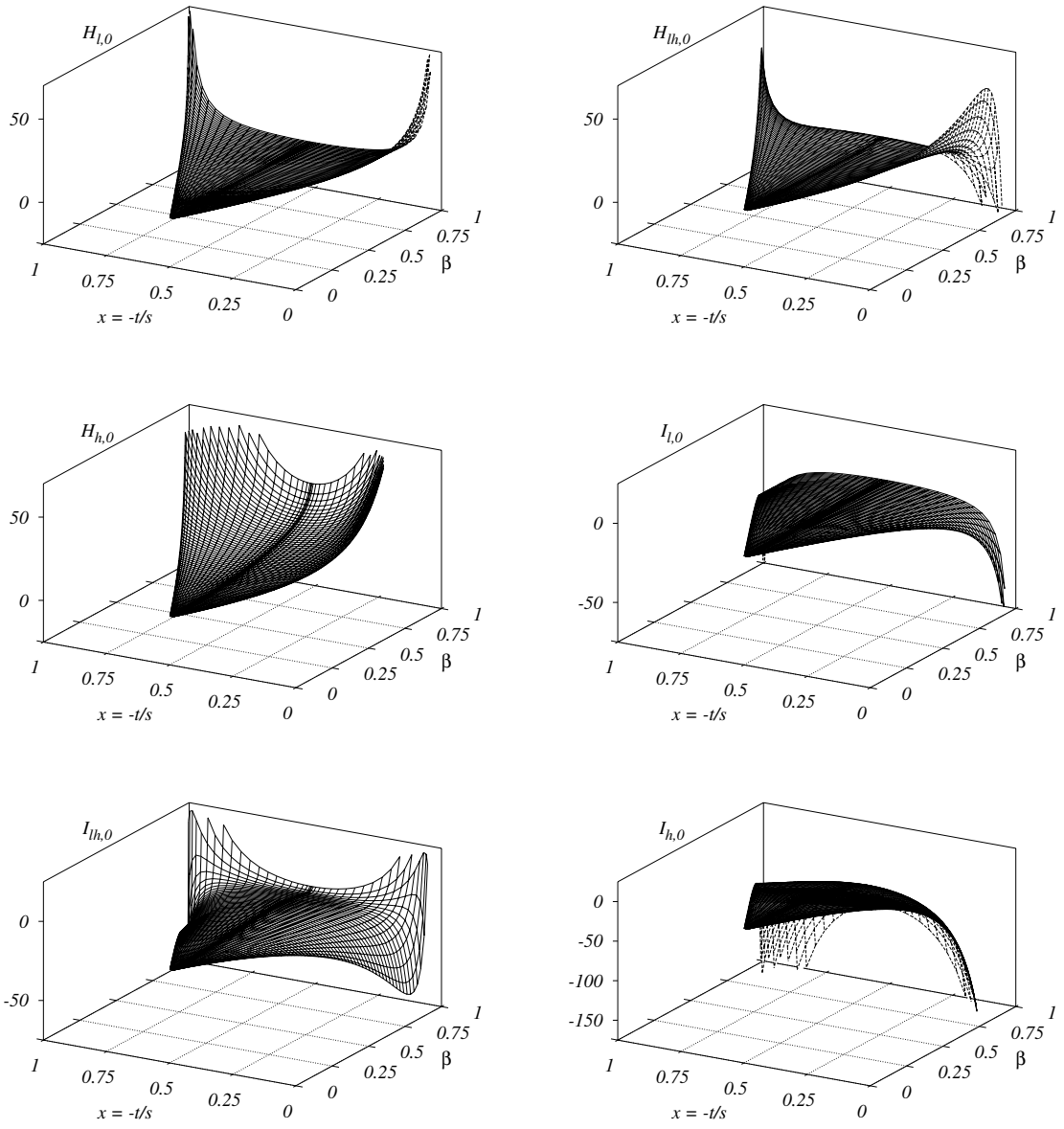

Figure 4.19.: Result of the different color factors of the finite part of the renormalized, differential double-fermionic cross section $\mathrm{d}\sigma_{gg}^{\mathrm{VV}}$.

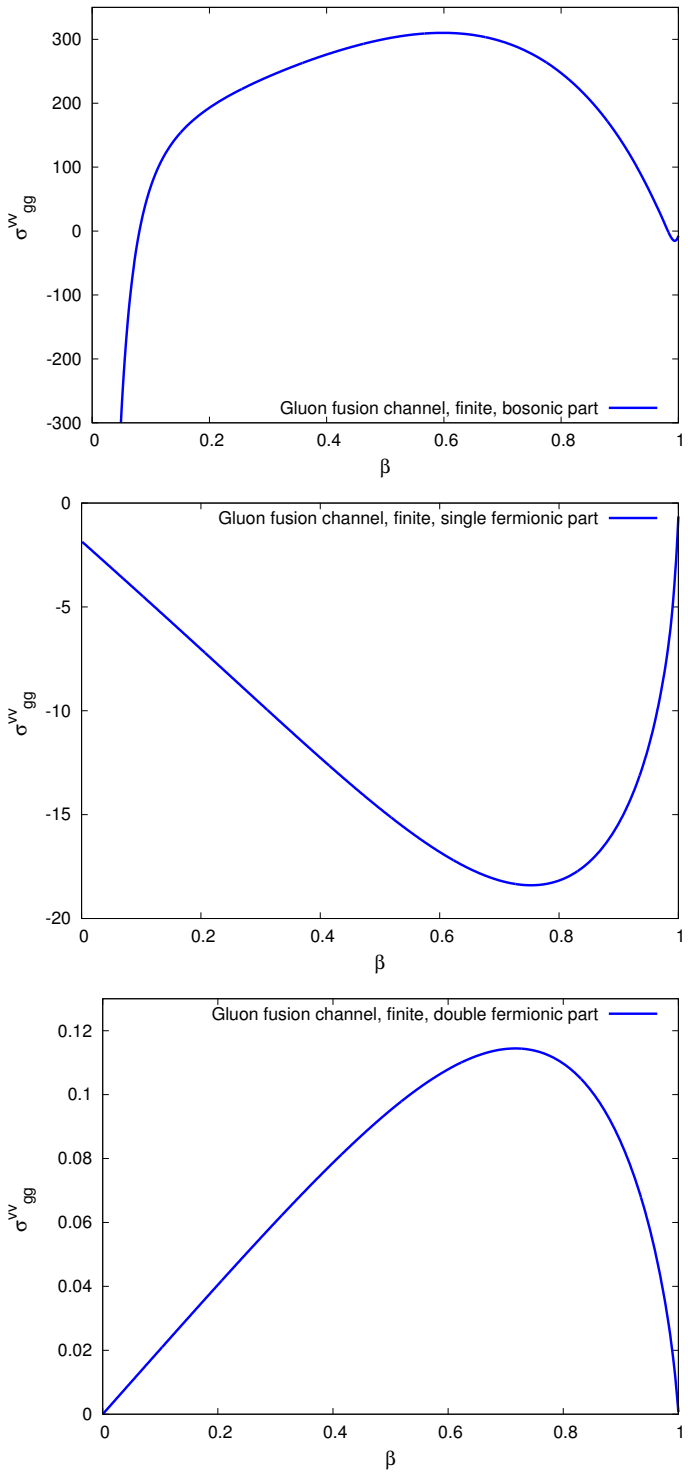

Figure 4.20.: Results for the bosonic, single- and double fermionic parts of the finite, renormalized total cross section $\sigma_{gg}^{\mathrm{VV}}$.

I checked my results against partial results of the NNLO virtual contributions, which were available in the literature, and implemented routines to check the master integrals.

4.6.1. Comparison with the Literature

There were four different partial results for the top quark pair cross section available in the literature. These were used to verify the correctness of our result.

Leading Color In the gluon fusion channel the leading color term A ($\sim N^5$) of equation 4.51 was calculated fully analytically in [58]. In the quark annihilation channel the double virtual part of the NNLO cross section can be color-expanded as:

$$\begin{aligned} &2\mathrm{Re}\,\langle\mathcal{M}^{(0)}|\mathcal{M}^{(2)}\rangle = \\ &\quad 2(N^2-1)\left(N^2A + B + \frac{1}{N^2}C + Nn_lD_l + Nn_hD_h + \frac{n_l}{N}E_l + \frac{n_h}{N}E_h + (n_l+n_h)^2F\right), \end{aligned} \tag{4.52}$$

where the leading color term was determined in [116] (see Section 2.4.2). Moreover, in the $q\overline{q}$-channel all terms proportional to n_l or n_h where calculated in [55] analytically as well. Since the leading color terms do not contain any non-planar diagrams they are much easier to computate. Our results agree up to ten digits, as it can be seen in Table 4.2. This comparison allows us to check all master integrals appearing at leading color, our implementation of the differential equations and the renormalization procedure.

Poles Structure In Section 2.4.3 it has been shown, how to derive the poles of the double virtual cross section from general properties of the amplitude. These were calculated in [32] analytically and agree with our result to all the 6 digits given in their paper (see Table 4.2). This allowed us to check the renormalization, the numerical integration and the correctness of the poles of the planar and non-planar diagrams.

High Energy Constraints The high-energy result (see Section2.4.1) was already published in [49] and was determined using a different method. Both numerical results agree. Here we could check the diagrams (planar and non-planar) in the high energy limit and the renormalization.

Low Energy Constraints From soft gluon resummation an additional constraint exists. For small β the total cross section was computed in [90] up to to NNLL order. This checked can only be used after adding the other three (partly unkown) pieces.

Overlap of Middlerange and Low-Energy Limit A completely independent check is given in the overlap region, where both, the numerical evaluation of the differential equations and the the threshold expansion work. The comparison of both results is done at the point $x = 0.45$ in the qq-channel and is 10^{-6}.

4.6.2. Additional Checks for the Master Integrals

Vanishing of 'Forbidden' Terms Although no proof exists, a conclusion from many multi-loops calculations is that only a certain set of numbers and functions appears in the amplitude. In the case of top quark Pair production at NNLO-level these are harmonic polylogarithms (HPL's) of weight up to order 4 and transcendental number up to the same weight (i.e. $\zeta(2)$, $\zeta(2)\log(2)$, $\zeta(3)$, $\zeta(4)$[7]). Albeit, the master integrals can contain complicated functions. In my case there appeared HPL's up to order 6 and transcendental numbers up to order 5 (that means in addition $\zeta(3)\zeta(2)$ and $\zeta(5)$). Plugging in the masters into the amplitude these terms vanished.

In the low-energy regime an expansion of the masters in the variable $t \sim \beta$ was performed. These are plugged into the the amplitude, which is expressed through β and x as well. From non-relativistic QCD it is known, that β starts at the order β^{-2} at NNLO-level (these terms arise from the Coulomb interaction). In fact, all terms of the order β^{-6}, β^{-5}, β^{-4} cancel. The term of the order β^{-3} vanished by renormalization of the amplitude.

Differential Equations The method of differential equations was introduced in Section 4.2.2. It can be used as a powerful check. If all the master integrals fulfill the differential equations, both in m_s and in x, then the whole analytic structure of the master integrals is verified. The only possible source of error is the boundary of the differential equations, which cannot be checked with the differential equations.

Numeric Evaluation of the Master Integrals In order to check the boundary as well, a numerical check through direct integration, was implemented. All master integrals were checked numerically in the unphysical, euclidean space, where $m_s < 0$. I tried to avoid the routines, which were used to calculate the master integrals in the first place. The representation was generated by an independent routine of `MBrepresentation`. The ε-expansion was done by the independent package `MBresolve.m` [117]. Then the master integrals were integrated, after doing the asymptotics in m_s, with the help of the function MBintegrate from the package `MB.m`. Due to bad convergence of the integrals this could only be done in the euclidean region. However, I implemented an algorithm in `MB.m` [118], that allowed us to check all the integrals in the physical Minkowski space as well (see Appendix A). This includes the correctness of all the programs contributing to solve the differential equations.

Moreover, a lot of master integrals were originally calculated by using relations coming from TU-symmetry. An numeric agreement of the, by TU-symmetry derived, partner gives strong hints to the correctness of the calculated one.

With these two methods, the method of differential equations and the numeric evaluation, both the analytic structure and the boundary have been checked.

[7] $\zeta(a)$ is the Riemann Zeta-function $\zeta(a) = \sum_{n=1}^{\infty} \frac{1}{n^a}$

A. Integration in Minkowski Space

Higher order integrals appear naturally in multi-loop calculations, like after the ϵ-expansion of Mellin-Barnes representations. Analytic calculations are challenging, or can only be done in some limit of the kinematic variables. Numerical methods are often easier or are used as a check of results, obtained by analytic calculations. For reasons, which are explained below, integrals with massive propagators and physical branch cuts suffer from bad convergence and could only be integrated in the euclidian, unphysical space, where the kinematic invariant k^2 is smaller than 0. Based on a paper of Freitas and Huang[118], I implemented a new numerical routine in the MB.m[102] package for the integration of multi-loop integrals. This improves the convergence of the integrals in the physical region ($k^2 > 0$) drastically, and allowed us to check our results even close to threshold.
Like explained in Chapter 4, a Mellin-Barnes representation is a contour integral in the complex plane, which contains products of gamma functions, their derivatives and powers of kinematic and mass invariants. There are two ways to calculate it. The first one is to sum up the residues which are enclosed by the contour. This is used to get analytic results. The second one is to obtain a numeric result by integrating along the imaginary axis. The arc is neglected since the integrals fall off sufficiently fast.

$$\int_{C_i} dz_i \, f(z_i) = i \int_{-\infty}^{\infty} dy_i \, f(c_i + iy_i), \tag{A.1}$$

In the euclidian region ($k^2 < 0$), powers of the kinematics and mass invariants contribute with an oscillating factor $(k_i^2)^{z_i} = Const. * (k_i^2)^{iy_i}$, which gets suppressed, since gamma and polygamma functions with big imaginary arguments rapidly tend to zero. Therefore the integrals converge quickly.
However, in regions with physical momenta, additional exponential growing factors arises,

$$(-k^2)^{z_i} = (k^2)^{c_i+iy_i}(-1 - i\epsilon)^{c_i+iy_i} = (k^2)^{z_i} e^{i\pi c_i} e^{\pi y_i}, \tag{A.2}$$

where $z_i = c_i + iy_i$ and k^2 is a kinematic invariant.
Although the integral is finite, the exponential factor $e^{\pi y_i}$ may spoil the numerical convergence. The integrals decreases slowly and conventional integration routines fail, since they have difficulties to integrate the tails over many oscillation periods. This is an inherent problem of Mellin-Barnes integrals in the minkowski space.
The numerical convergence can be radically improved by a contour deformation in the complex plane. This has to take place in such a way, that no pole crossings occur. For a one-dimensional integral, the contour can be rotated by an angle:

$$c_1 + iy_1 \to c_1 + (\theta + i)y_1 \tag{A.3}$$

In theory, the angle can be chosen such, that it cancels the exponential growing factor.

$$(-k^2)^{z_i} = (k^2)^{c_i+iy_i}(-1-i\epsilon)^{c_i+iy_i} = (k^2)^{z_i} e^{i\pi c_i} e^{(\pi+\theta log(k^2))y_i} \tag{A.4}$$

In praxis a wide range of different angles leads to acceptable numerical results.
Multi-loop integrals are slightly more complicated. To ensure, that no poles cross the contour, a transformation to hyperspherical coordinates is reasonable, which consists of one radial and $n-1$ angular components.

$$\begin{aligned} y_1 &= r\cos\phi_1, \\ y_2 &= r\sin\phi_1\cos\phi_2, \\ &\vdots \qquad\qquad \vdots \\ y_{n-1} &= r\sin\phi_1\cdots\sin\phi_{n-2}\cos\phi_{n-1}, \\ y_n &= r\sin\phi_1\cdots\sin\phi_{n-2}\sin\phi_{n-1} \end{aligned} \tag{A.5}$$

Only the radial coordinate r is affected by the transformation A.3. Again, a sophisticated choice of θ eliminates the exponential factors and restore convergence. MB.m automatically converts the Mathematica code for the integrals to FORTRAN code, where they get evaluated with the Monte-Carlo programs Cuhre or Vegas from the Cuba[119] library.
The new method allows to integrate strong oscillating integrals like the 2-fold from equation (10) in [102].

$$\int_{-i\infty}^{i\infty}\int_{-i\infty}^{i\infty} dz_1\, dz_2\, (-s)^{-z_1-z_2} \frac{\Gamma^3(-z_1)\Gamma(1+z_1)\Gamma^3(-z_2)\Gamma(1+z_2)}{\Gamma(-2z_1)\Gamma(-2z_2)}, \tag{A.6}$$

The 2-fold integral is a product of two one dimensional integrals and can be evaluated by resuming the residues exactly. For $s=2$, the result is π^2. But due to strong oscillation of the integrand it was shown in [102], that advanced integration techniques were necessary to get acceptable results with with less than 1% error.
In figure 1 the imaginary part of the integrand is pictured before, in figure 2 after the contour deformation. The real part behaves similar. $\Theta = -0.4$ was used to generate the plots. The convergence of the latter integral is extremely improved and a precision of 10^{-10} can be achieved within seconds.
The method was used to check the most of our master integrals in the qq and in the gg channel with a precision of less than 1% in the deep minkowski space ($\frac{m_{Top}^2}{s} \approx 0.2485$). Even higher precision is available. The most difficult non-planar 7-liners in the qq channel (tensor of first order).can be calculated within 3-5 minutes to a precision of less than 1‰.
The routine is included in version 1.3 of the MB.m package and can be downloaded from http://projects.hepforge.org/mbtools/.

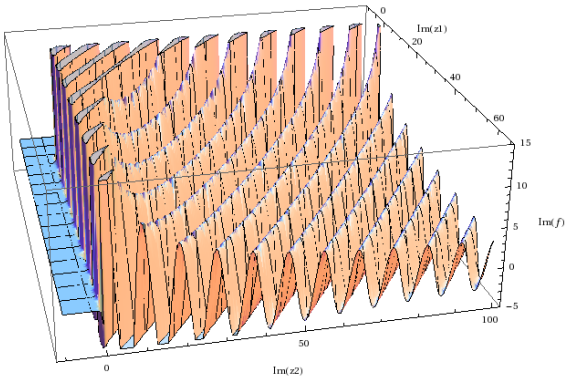

Figure A.1.: Integral A.6 before contour deformation.

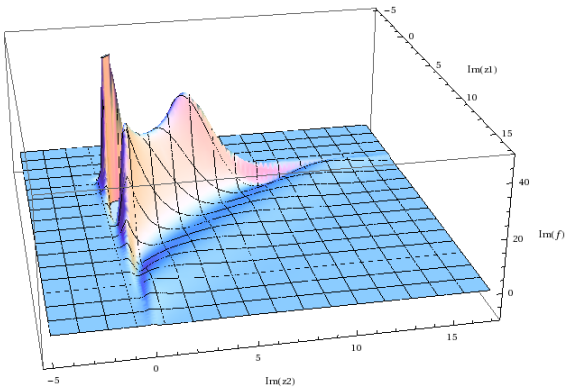

Figure A.2.: Integral A.6 after contour deformation.

Bibliography

[1] Marc-Andre Pleier. Review of Properties of the Top Quark from Measurements at the Tevatron. *Int.J.Mod.Phys.*, A24:2899–3037, 2009.

[2] John M. Campbell, J.W. Huston, and W.J. Stirling. Hard Interactions of Quarks and Gluons: A Primer for LHC Physics. *Rept.Prog.Phys.*, 70:89, 2007.

[3] *Personal discussion of the author with Peter Jenni (Atlas collaboration).*

[4] *www-d0.fnal.gov*. 2011.

[5] M. Beneke, P. Falgari, S. Klein, and C. Schwinn. Hadronic top-quark pair production with NNLL threshold resummation. 2011.

[6] Rikkert Frederix and Fabio Maltoni. Top pair invariant mass distribution: A Window on new physics. *JHEP*, 0901:047, 2009.

[7] Rikkert Frederix. Top quark phenomenology. 2010.

[8] Leandro G. Almeida, George F. Sterman, and Werner Vogelsang. Threshold Resummation for the Top Quark Charge Asymmetry. *Phys.Rev.*, D78:014008, 2008.

[9] Valentin Ahrens, Andrea Ferroglia, Matthias Neubert, Ben D. Pecjak, and Li Lin Yang. Renormalization-Group Improved Predictions for Top-Quark Pair Production at Hadron Colliders. *JHEP*, 1009:097, 2010.

[10] German Rodrigo and Paola Ferrario. Charge asymmetry: A Theory appraisal. *Nuovo Cim.*, C33:04, 2010.

[11] Qing-Hong Cao, David McKeen, Jonathan L. Rosner, Gabe Shaughnessy, and Carlos E.M. Wagner. Forward-Backward Asymmetry of Top Quark Pair Production. *Phys.Rev.*, D81:114004, 2010.

[12] ATL-PHYS-PUB-2009-084. *Atlas Collaboration*. 2009.

[13] M.W. Grunewald. Experimental tests of the electroweak standard model at high-energies. *Phys.Rept.*, 322:125–346, 1999.

[14] S. Dittmaier et al. Handbook of LHC Higgs Cross Sections: 1. Inclusive Observables. 2011. * Temporary entry *.

[15] Richard D. Ball et al. Unbiased global determination of parton distributions and their uncertainties at NNLO and at LO. 2011.

[16] R.S. Thorne and G. Watt. PDF dependence of Higgs cross sections at the Tevatron and LHC: Response to recent criticism. *JHEP*, 1108:100, 2011.

[17] *www.mstwpdf.hepforge.org/pdf4lhc/partonlumi7TeVnnlo.html*. 2011.

[18] R. Keith Ellis, W. James Stirling, and B. R. Webber. QCD and collider physics. *Camb. Monogr. Part. Phys. Nucl. Phys. Cosmol.*, 8:1–435, 1996.

[19] S. Moch, J.A.M. Vermaseren, and A. Vogt. The Three loop splitting functions in QCD: The Nonsinglet case. *Nucl.Phys.*, B688:101–134, 2004.

[20] A. Vogt, S. Moch, and J.A.M. Vermaseren. The Three-loop splitting functions in QCD: The Singlet case. *Nucl.Phys.*, B691:129–181, 2004.

[21] Guido Altarelli and G. Parisi. Asymptotic Freedom in Parton Language. *Nucl. Phys.*, B126:298, 1977.

[22] Juan Rojo. Parton Distributions and LHC data. 2011.

[23] Roberto Bonciani, Stefano Catani, Michelangelo L. Mangano, and Paolo Nason. NLL resummation of the heavy-quark hadroproduction cross- section. *Nucl. Phys.*, B529:424–450, 1998.

[24] P. Nason, S. Dawson, and R. Keith Ellis. The Total Cross-Section for the Production of Heavy Quarks in Hadronic Collisions. *Nucl. Phys.*, B303:607, 1988.

[25] W. Beenakker, H. Kuijf, W. L. van Neerven, and J. Smith. QCD Corrections to Heavy Quark Production in p anti-p Collisions. *Phys. Rev.*, D40:54–82, 1989.

[26] M. Czakon and A. Mitov. Inclusive Heavy Flavor Hadroproduction in NLO QCD: the Exact Analytic Result. *Nucl. Phys.*, B824:111–135, 2010.

[27] Nikolaos Kidonakis. Two-loop soft anomalous dimensions and NNLL resummation for heavy quark production. *Phys.Rev.Lett.*, 102:232003, 2009.

[28] Alexander Mitov, George F. Sterman, and Ilmo Sung. The Massive Soft Anomalous Dimension Matrix at Two Loops. *Phys.Rev.*, D79:094015, 2009.

[29] Thomas Becher and Matthias Neubert. Infrared singularities of QCD amplitudes with massive partons. *Phys.Rev.*, D79:125004, 2009.

[30] M. Beneke, P. Falgari, and C. Schwinn. Soft radiation in heavy-particle pair production: All-order colour structure and two-loop anomalous dimension. *Nucl.Phys.*, B828:69–101, 2010.

[31] Michal Czakon, Alexander Mitov, and George F. Sterman. Threshold Resummation for Top-Pair Hadroproduction to Next-to-Next-to-Leading Log. *Phys.Rev.*, D80:074017, 2009.

[32] Andrea Ferroglia, Matthias Neubert, Ben D. Pecjak, and Li Lin Yang. Two-loop divergences of scattering amplitudes with massive partons. *Phys.Rev.Lett.*, 103:201601, 2009.

[33] S. Catani. Higher order QCD corrections in hadron collisions: Soft gluon resummation and exponentiation. *Nucl.Phys.Proc.Suppl.*, 54A:107–113, 1997.

[34] Stefano Catani, Michelangelo L. Mangano, Paolo Nason, and Luca Trentadue. The Top cross-section in hadronic collisions. *Phys.Lett.*, B378:329–336, 1996.

[35] George F. Sterman. Summation of Large Corrections to Short Distance Hadronic Cross-Sections. *Nucl.Phys.*, B281:310, 1987.

[36] S. Catani and L. Trentadue. Resummation of the QCD Perturbative Series for Hard Processes. *Nucl.Phys.*, B327:323, 1989.

[37] S. Catani and L. Trentadue. Comment on QCD exponentiation at large x. *Nucl.Phys.*, B353:183–186, 1991.

[38] M. Beneke, P. Falgari, S. Klein, and C. Schwinn. Threshold expansion of massive coloured particle cross sections. *Nucl.Phys.Proc.Suppl.*, 205-206:20–24, 2010.

[39] P. Nason, S. Dawson, and R. Keith Ellis. The One Particle Inclusive Differential Cross-Section for Heavy Quark Production in Hadronic Collisions. *Nucl. Phys.*, B327:49–92, 1989.

[40] A. Denner, S. Dittmaier, S. Kallweit, and S. Pozzorini. NLO QCD corrections to WWbb production at hadron colliders. *Phys.Rev.Lett.*, 106:052001, 2011.

[41] Giuseppe Bevilacqua, Michal Czakon, Andreas van Hameren, Costas G. Papadopoulos, and Malgorzata Worek. Complete off-shell effects in top quark pair hadroproduction with leptonic decay at next-to-leading order. *JHEP*, 1102:083, 2011.

[42] Werner Bernreuther. Top quark physics at the LHC. *J. Phys.*, G35:083001, 2008.

[43] Werner Bernreuther, Michael Fucker, and Zong-Guo Si. Weak interaction corrections to hadronic top quark pair production: Contributions from quark-gluon and b anti-b induced reactions. *Phys.Rev.*, D78:017503, 2008.

[44] Werner Bernreuther, Michael Fuecker, and Zong-Guo Si. Weak interaction corrections to hadronic top quark pair production. *Phys.Rev.*, D74:113005, 2006.

[45] W. Bernreuther, Michael Fuecker, and Z.G. Si. Mixed QCD and weak corrections to top quark pair production at hadron colliders. *Phys.Lett.*, B633:54–60, 2006.

[46] Wolfgang Hollik and Monika Kollar. NLO QED contributions to top-pair production at hadron collider. *Phys.Rev.*, D77:014008, 2008.

[47] Personal talk of the author with Peter Jenni (Atlas collaboration). 2011.

[48] M. Czakon, A. Mitov, and S. Moch. Heavy-quark production in massless quark scattering at two loops in QCD. *Phys.Lett.*, B651:147–159, 2007.

[49] M. Czakon, A. Mitov, and S. Moch. Heavy-quark production in gluon fusion at two loops in QCD. *Nucl.Phys.*, B798:210–250, 2008. * Temporary entry *.

[50] Stefano Catani. The Singular behavior of QCD amplitudes at two loop order. *Phys.Lett.*, B427:161–171, 1998.

[51] George F. Sterman and Maria E. Tejeda-Yeomans. Multiloop amplitudes and resummation. *Phys.Lett.*, B552:48–56, 2003.

[52] A. Mitov and S. Moch. The Singular behavior of massive QCD amplitudes. *JHEP*, 0705:001, 2007.

[53] John C. Collins. ALGORITHM TO COMPUTE CORRECTIONS TO THE SUDAKOV FORM-FACTOR. *Phys.Rev.*, D22:1478, 1980.

[54] Ashoke Sen. Asymptotic Behavior of the Sudakov Form-Factor in QCD. *Phys.Rev.*, D24:3281, 1981.

[55] R. Bonciani, A. Ferroglia, T. Gehrmann, D. Maitre, and C. Studerus. Two-Loop Fermionic Corrections to Heavy-Quark Pair Production: The Quark-Antiquark Channel. *JHEP*, 0807:129, 2008.

[56] R. Bonciani, A. Ferroglia, T. Gehrmann, C. Studerus, and D. Maitre. Fermionic Corrections to the Heavy-Quark Pair Production in the Quark-Antiquark Channel. 2008. * Temporary entry *.

[57] Jens Vollinga. GiNaC: Symbolic computation with C++. *Nucl.Instrum.Meth.*, A559:282–284, 2006.

[58] R. Bonciani, A. Ferroglia, T. Gehrmann, A. Manteuffel, and C. Studerus. Two-Loop Leading Color Corrections to Heavy-Quark Pair Production in the Gluon Fusion Channel. *JHEP*, 01:102, 2011.

[59] S. Laporta. High-precision calculation of multi-loop Feynman integrals by difference equations. *Int. J. Mod. Phys.*, A15:5087–5159, 2000.

[60] S. Laporta and E. Remiddi. Analytic treatment of the two loop equal mass sunrise graph. *Nucl.Phys.*, B704:349–386, 2005.

[61] T. Kinoshita. Mass singularities of Feynman amplitudes. *J.Math.Phys.*, 3:650–677, 1962.

[62] T.D. Lee and M. Nauenberg. Degenerate Systems and Mass Singularities. *Phys.Rev.*, 133:B1549–B1562, 1964.

[63] John C. Collins, Davison E. Soper, and George Sterman. Factorization of Hard Processes in QCD. *Adv. Ser. Direct. High Energy Phys.*, 5:1–91, 1988.

[64] Andrea Ferroglia, Matthias Neubert, Ben D. Pecjak, and Li Lin Yang. Two-loop divergences of massive scattering amplitudes in non-abelian gauge theories. *JHEP*, 0911:062, 2009.

[65] Martin Beneke, Pietro Falgari, and Christian Schwinn. Threshold resummation for pair production of coloured heavy (s)particles at hadron colliders. *Nucl.Phys.*, B842:414–474, 2011.

[66] Thomas Becher and Matthias Neubert. Infrared singularities of scattering amplitudes in perturbative QCD. *Phys.Rev.Lett.*, 102:162001, 2009.

[67] Thomas Becher and Matthias Neubert. On the Structure of Infrared Singularities of Gauge-Theory Amplitudes. *JHEP*, 0906:081, 2009.

[68] S.Mert Aybat, Lance J. Dixon, and George F. Sterman. The Two-loop anomalous dimension matrix for soft gluon exchange. *Phys.Rev.Lett.*, 97:072001, 2006.

[69] S.Mert Aybat, Lance J. Dixon, and George F. Sterman. The Two-loop soft anomalous dimension matrix and resummation at next-to-next-to leading pole. *Phys.Rev.*, D74:074004, 2006.

[70] Michael Edward Peskin and Daniel V. Schroeder. An Introduction to quantum field theory. Reading, USA: Addison-Wesley (1995) 842 p.

[71] S. Catani and M.H. Seymour. A General algorithm for calculating jet cross-sections in NLO QCD. *Nucl.Phys.*, B485:291–419, 1997.

[72] Zoltan Nagy and Davison E. Soper. General subtraction method for numerical calculation of one loop QCD matrix elements. *JHEP*, 0309:055, 2003.

[73] S. Frixione, Z. Kunszt, and A. Signer. Three jet cross-sections to next-to-leading order. *Nucl.Phys.*, B467:399–442, 1996.

[74] M. Czakon. A novel subtraction scheme for double-real radiation at NNLO. *Phys.Lett.*, B693:259–268, 2010.

[75] M. Czakon. Double-real radiation in hadronic top quark pair production as a proof of a certain concept. *Nucl.Phys.*, B849:250–295, 2011.

[76] A. Gehrmann-De Ridder, T. Gehrmann, and E.W.Nigel Glover. Antenna subtraction at NNLO. *JHEP*, 0509:056, 2005. Erratum added online, 8/18/06.

[77] T. Binoth and G. Heinrich. An Automatized algorithm to compute infrared divergent multiloop integrals. *Nucl.Phys.*, B585:741–759, 2000.

[78] J.G. Korner, Z. Merebashvili, and M. Rogal. Laurent series expansion of massive scalar one-loop integrals to $O(epsilson^{2)}$. *Phys.Rev.*, D71:054028, 2005.

[79] B. Kniehl, Z. Merebashvili, J.G. Korner, and M. Rogal. Heavy quark pair production in gluon fusion at next-to-next-to-leading $O(\alpha_s^{4)}$ order: One-loop. *Phys.Rev.*, D78:094013, 2008.

[80] J.G. Korner, Z. Merebashvili, and M. Rogal. NNLO $O(\alpha_s^4)$ results for heavy quark pair production in quark-antiquark collisions: The One-loop squared contributions. *Phys.Rev.*, D77:094011, 2008.

[81] Charalampos Anastasiou and S.Mert Aybat. The One-loop gluon amplitude for heavy-quark production at NNLO. *Phys.Rev.*, D78:114006, 2008.

[82] J.G. Korner, Z. Merebashvili, and M. Rogal. Laurent series expansion of a class of massive scalar one-loop integrals up to O(epsilon**2) in terms of multiple polylogarithms. *J.Math.Phys.*, 47:072302, 2006.

[83] Z. Bern, Lance J. Dixon, D.C. Dunbar, and D.A. Kosower. Recent progress in one loop multiparton calculations. *Nucl.Phys.Proc.Suppl.*, 39BC:146–149, 1995.

[84] Zvi Bern, Vittorio Del Duca, and Carl R. Schmidt. The Infrared behavior of one loop gluon amplitudes at next-to-next-to-leading order. *Phys.Lett.*, B445:168–177, 1998.

[85] David A. Kosower and Peter Uwer. One loop splitting amplitudes in gauge theory. *Nucl.Phys.*, B563:477–505, 1999.

[86] Zvi Bern, Vittorio Del Duca, William B. Kilgore, and Carl R. Schmidt. The Infrared behavior of one loop QCD amplitudes at next-to-next-to leading order. *Phys.Rev.*, D60:116001, 1999.

[87] Stefano Catani and Massimiliano Grazzini. The soft gluon current at one loop order. *Nucl.Phys.*, B591:435–454, 2000.

[88] Isabella Bierenbaum, Michal Czakon, and Alexander Mitov. The singular behavior of one-loop massive QCD amplitudes with one external soft gluon. 2011.

[89] P. Bärnreuther, M. Czakon, and A. Mitov. *Percent level precision physics at the Tevatron.* To be published, 2012.

[90] Martin Beneke, Michal Czakon, Pietro Falgari, Alexander Mitov, and Christian Schwinn. Threshold expansion of the gg(qq) $\to$ QQ+X cross section at O(α_s^4). *Phys. Lett.*, B690:483–490, 2010.

[91] Michal Czakon and Alexander Mitov. Top++: a program for the calculation of the top-pair cross-section at hadron colliders. 2011.

[92] Matteo Cacciari, Michal Czakon, Michelangelo L. Mangano, Alexander Mitov, and Paolo Nason. Top-pair production at hadron colliders with next-to-next-to-leading logarithmic soft-gluon resummation. *Phys.Lett.*, B710:612–622, 2012.

[93] M. Czakon. Tops from Light Quarks: Full Mass Dependence at Two-Loops in QCD. *Phys. Lett.*, B664:307–314, 2008.

[94] M. Czakon. *Diagen*. Unpublished.

[95] J.A.M. Vermaseren. FORM development. 2011. * Temporary entry *.

[96] V. A. Smirnov. *Evaluating Feynman Integrals*. Springer, 2004.

[97] D. Kosower. *barnesroutines.m*. http://projects.hepforge.org/mbtools/, 2009.

[98] S. Moch and P. Uwer. XSummer: Transcendental functions and symbolic summation in Form. *Comput. Phys. Commun.*, 174:759–770, 2006.

[99] David H. Bailey and David J. Broadhurst. Parallel integer relation detection: Techniques and applications. *MATH.COMPUT.*, 70:1719, 2001.

[100] J. Gluza, K. Kajda, and T. Riemann. AMBRE - a Mathematica package for the construction of Mellin-Barnes representations for Feynman integrals. *Comput. Phys. Commun.*, 177:879–893, 2007.

[101] M. Czakon G. Chachamis. *MBrepresenatation*. Unpublished, 2007.

[102] M. Czakon. Automatized analytic continuation of Mellin-Barnes integrals. *Comput. Phys. Commun.*, 175:559–571, 2006.

[103] J.B. Tausk. Nonplanar massless two loop Feynman diagrams with four on-shell legs. *Phys.Lett.*, B469:225–234, 1999.

[104] N. Nielsen. *Der Eulersche Dilogarithmus und seine Verallgemeinerungen*. Nova Acta Leopoldina (Halle), 1909.

[105] E. Remiddi and J. A. M. Vermaseren. Harmonic polylogarithms. *Int. J. Mod. Phys.*, A15:725–754, 2000.

[106] M. Czakon. *Quadprec*. Unpublished, 2008.

[107] C.W. Gear. *Numerical Initial Value Problems in Ordinary Differential Equations*. Prentice Hall, 1971.

[108] W.H. Press et al.

[109] A. C. Hindmarsh. ODEPACK, A Systematized Collection of ODE Solvers. *Scientific Computing*, 1, 1983.

[110] Bailey Hida, Li. *Quad-Double Computation Package*. 2009.

[111] T. van Ritbergen, J.A.M. Vermaseren, and S.A. Larin. The Four loop beta function in quantum chromodynamics. *Phys.Lett.*, B400:379–384, 1997.

[112] M. Czakon. The Four-loop QCD beta-function and anomalous dimensions. *Nucl.Phys.*, B710:485–498, 2005.

[113] K.G. Chetyrkin and M. Steinhauser. Short distance mass of a heavy quark at order **3(s). *Phys.Rev.Lett.*, 83:4001–4004, 1999.

[114] Kirill Melnikov and Timo van Ritbergen. The Three loop relation between the MS-bar and the pole quark masses. *Phys.Lett.*, B482:99–108, 2000.

[115] Kirill Melnikov and Timo van Ritbergen. The Three loop on-shell renormalization of QCD and QED. *Nucl.Phys.*, B591:515–546, 2000.

[116] R. Bonciani, A. Ferroglia, T. Gehrmann, and C. Studerus. Two-Loop Planar Corrections to Heavy-Quark Pair Production in the Quark-Antiquark Channel. *JHEP*, 0908:067, 2009.

[117] A.V. Smirnov and V.A. Smirnov. On the Resolution of Singularities of Multiple Mellin-Barnes Integrals. *Eur.Phys.J.*, C62:445–449, 2009.

[118] Ayres Freitas and Yi-Cheng Huang. On the Numerical Evaluation of Loop Integrals With Mellin- Barnes Representations. *JHEP*, 04:074, 2010.

[119] T. Hahn. CUBA: A library for multidimensional numerical integration. *Comput. Phys. Commun.*, 168:78–95, 2005.

Acknowledgements

A variety of ingredients are required to transform a new city into a new home, and a PhD topic into a dissertation. Therefore I would like to thank all, who contributed directly or indirectly to the success of this thesis.

My great thanks go to Prof. Czakon, for entrusting me with this important and interesting subject, as well as for the excellent supervision. Moreover, he supported me to start my economic studies and therewith setting the course for my future career.

I am especially grateful to the Coffee group, for providing all the interesting physical and unphysical conversations, in particular Alex, Jan und Jürgen.

I also want to thank my office colleagues Carsten, Johannes and Cheng-Han for fruitful discussions and Anke Bachtenkirch for helping me to deal with all sorts of bureaucratic matters.

Special thanks go to my parents who always have encouraged and supported me during my studies, and to Ali, Larissa and Isabella and to my sisters Sandra and Birgit for proofreading.

Finally, I would like to thank all the people who transformed Aachen into a new home. This includes in particular: Monica, Matti, Maria, Lotterich, Alexander Lynn, Marie and 'Die Onkel Toms Prinzen'.